applied sciences

Article

# Experimental and Simulation Research on the Process of Nitrogen Migration and Transformation in the Fluctuation Zone of Groundwater Level

**Yuepeng Li [1,2,*], Liuyue Wang [1,2], Xun Zou [1,2], Jihong Qu [1,2] and Gang Bai [1,2]**

[1] College of Geosciences and Engineering, North China University of Water Resources and Electric Power, Zhengzhou 450046, China; z20201020259@stu.ncwu.edu.cn (L.W.); x201810207166@stu.ncwu.edu.cn (X.Z.); qujihong@ncwu.edu.cn (J.Q.); x20201020232@stu.ncwu.edu.cn (G.B.)
[2] Collaborative Innovation Center for Efficient Utilization of Water Resources, Zhengzhou 450046, China
* Correspondence: liyuepeng@ncwu.edu.cn; Tel.: +86-139-3716-5752

**Abstract:** The fluctuation of groundwater causes a change in the groundwater environment and then affects the migration and transformation of pollutants. To study the influence of water level fluctuations on nitrogen migration and transformation, physical experiments on the nitrogen migration and transformation process in the groundwater level fluctuation zone were carried out. A numerical model of nitrogen migration in the Vadose zone and the saturated zone was constructed by using the software HydrUS-1D. The correlation coefficient and the root mean square error of the model show that the model fits well. The numerical model is used to predict nitrogen migration and transformation in different water level fluctuation scenarios. The results show that, compared with the fluctuating physical experiment scenario, when the fluctuation range of the water level increases by 5 cm, the fluctuation range of the nitrogen concentration in the coarse sand, medium sand and fine sand media increases by 37.52%, 31.40% and 21.14%, respectively. Additionally, when the fluctuation range of the water level decreases by 5 cm, the fluctuation range of the nitrogen concentration in the coarse sand, medium sand and fine sand media decreases by 36.74%, 14.70% and 9.39%, respectively. The fluctuation of nitrogen concentration varies most significantly with the amplitude of water level fluctuations in coarse sand; the change in water level has the most significant impact on the flux of nitrate nitrogen and has little effect on the change in nitrite nitrogen and ammonium nitrogen, and the difference in fine sand is the most obvious, followed by medium sand, and the difference in coarse sand is not great.

**Keywords:** groundwater level fluctuation zone; nitrogen; migration and transformation; HYDRUS-1D model

**Citation:** Li, Y.; Wang, L.; Zou, X.; Qu, J.; Bai, G. Experimental and Simulation Research on the Process of Nitrogen Migration and Transformation in the Fluctuation Zone of Groundwater Level. *Appl. Sci.* **2022**, *12*, 3742. https://doi.org/10.3390/app12083742

Academic Editor: Bing Bai

Received: 1 March 2022
Accepted: 5 April 2022
Published: 8 April 2022

**Publisher's Note:** MDPI stays neutral with regard to jurisdictional claims in published maps and institutional affiliations.

**Copyright:** © 2022 by the authors. Licensee MDPI, Basel, Switzerland. This article is an open access article distributed under the terms and conditions of the Creative Commons Attribution (CC BY) license (https://creativecommons.org/licenses/by/4.0/).

## 1. Introduction

Due to industry [1,2], agriculture [3,4], life [5], aquaculture [6], atmospheric deposition [7] and other factors, the groundwater in many countries and regions around the world are affected by nitrogen pollution, including the United States [8], China [9], the United Kingdom [10], South Korea [11] and other countries with severe pollution. In 2005, 34.1% of 1139 groundwater samples in northern China failed to meet World Health Organization (WHO) criteria. [12]. Currently, China has become one of the countries with the highest nitrogen fertilizer used in the world [13]. Nitrate from nitrogen may rapidly leach into groundwater, affecting the ecology and human health [14]. Wild et al. concluded that even if nitrate input is significantly reduced in the future, it will take decades to significantly reduce nitrate concentrations in porous aquifers through denitrification [15]. In 2000, the Water Framework Directive to bring water bodies to good chemical and ecological status by 2027 was issued [16]. Therefore, how to scientifically understand the nitrogen migration and transformation patterns under fluctuating groundwater level conditions has become one of the hot issues in the field of environmental research.

During groundwater level fluctuations, soluble substances in the aquifer medium are gradually dissolved into the groundwater, thus changing the chemical composition of the groundwater [17]. Guo Huaming et al. [18] studied the influencing factors of arsenic enrichment in groundwater, and the results showed that a high pH was unfavorable to the adsorption of arsenic in the form of anions by the aquifer medium. In their study, Sorensen J et al. [19] found that chemical and biological contaminants near the surface were transported to groundwater with minimal attenuation. Water level fluctuations also have a significant effect on nitrogen. Hefting M et al. [20] selected 13 riparian sites to analyze nitrogen cycling processes and confirmed a direct positive correlation between denitrification and elevated water table levels. Heather L. Welch et al. [21] analyzed and found that nitrate-N is weakened by denitrification during downward transport using redox sensitivity metrics at the water table without a location in the vertical direction. Jurado A et al. [22] concluded that the accumulation of $N_2O$ in groundwater is also mainly due to denitrification and, to a lesser extent, nitrification. Yang L.P. et al. [23] conducted indoor soil column experiments to study the effect of pH on nitrogen transport and transformation processes and showed that pH 6.5 was the most efficient for the removal of "tri-nitrogen" in the optimal pH range for adsorption nitrification and denitrification. The authors in [24] analyzed the effect of water level fluctuation on nitrogen transformation by simulating aerobic, anoxic and anaerobic zones, and the results showed that denitrification played the greatest role in the anaerobic zone.

Groundwater level fluctuations significantly affect the migration and transformation of groundwater pollutants [25–29]. Scholars at home and abroad have conducted studies on groundwater level fluctuations. Most of their research focuses on the migration and transformation processes of soil salinity, iron, manganese, arsenic, iodin, benzene and other characteristic components when subjected to water level fluctuations, etc. [18,30,31]. Davis et al. [32] studied the changes of organic matter and oxygen at the fluctuation of water level, and the results showed that BTEX and oxygen concentration showed a relationship between this and that near the water level, and the main reason for oxygen reduction was due to microbial degradation. Kamon et al. [33] conducted an experimental and numerical study of the migration of LNAPL with water level fluctuations and showed that the entry and displacement pressures were greater for the air-water system than for the LNAPL-water system. Xiaoxi Xie et al. [34] analyzed the hysteresis relationship between saturation and the capillary pressure in a medium under the water table fluctuation conditions during alternating drying and wetting processes, and the results demonstrated that when the initial water saturation of the drying process is similar, the greater the initial water saturation of the wetting process, the degree of hysteresis gradually decreases. Xiang Li et al. [35] analyzed and verified that groundwater level fluctuations affected the physicochemical properties of soil-water bodies and further affected the movement of nitrate in soil solids.

Research on the mechanisms of solute migration and transformation in the fluctuation zone of groundwater level, mainly through technical methods, such as field investigation, indoor experiments, theoretical analysis and numerical simulation, was conducted to predict the temporal and spatial distribution characteristics of solute pollution. Chen et al. [36] found through field experiments, that the depth of shallow groundwater has more influence on the nitrogen concentration in shallow groundwater than other factors. Zhang Dan et al. [27] conducted on-site monitoring of plots at different altitudes for a year. They found that the fluctuation of shallow groundwater levels significantly affected the soil profile and the nitrogen concentration of shallow groundwater. Farnsworth et al. [37] established an indoor soil column experiment, using a set of 1.3 m quartz sand columns inoculated with microorganisms, and changing the water level in the sand column every 30~50 h to simulate the periodic production wells of production wells and groundwater caused by the cessation of mining and the influence of the level fluctuation on the oxidation of manganese—the content of manganese increases as the water level drops, and decreases as the water levels rise. Yang Yang [38] studied the influence of the groundwater level rise and fall on the migration of cadmium, and argued that the rise and fall in the water level mainly affect the transport of cadmium ions through convection. Zhang Xuejing et al. [39] used inverse distance weighting (IDW) interpolation and the water chemistry Piper graphic method to analyze the response relationship between the groundwater chemistry characteristics and the depth of the water level in the Ejina Oasis after the ecological water transport (2001–2017). Cao Wengeng et al. [40] used the potential distribution-multi-point complexation model (CD-MUSIC) to predict the evolution of groundwater chemical composition and hydrochemical types in the Baoding Plain of the South-to-North Water Transfer Project under the condition of groundwater level rebound. Arash Tafteh and Ali Reza Sepaskhah [41] successfully simulated the leaching of water and nitrate from two crops in the field with high accuracy using HYDRUS-1D. Mo Xiaoyu et al. [42] used HYDRUS-1D to simulate the changes in nitrogen leaching under different rainfall intensities, analyzed the influencing factors, and found that high intensity would reduce the nitrogen utilization rate.

In summary, the impact of water level fluctuations on the migration and transformation of pollutants has attracted the attention of scholars. Still, the study of nitrogen migration and transformation under different media water level fluctuations is not systematic enough. In this paper, the indoor soil column is used to simulate water level fluctuations to study the temporal and spatial distribution of nitrate nitrogen, nitrite nitrogen and ammonium nitrogen in three typical soil media subjected to water level fluctuations. According to physical experimental conditions, a numerical model of nitrogen migration and transformation in the fluctuation zone of the groundwater level was established to predict the spatial distribution and temporal change of nitrogen pollutants in the fluctuation zone of the groundwater level under different scenarios. This paper provides a scientific basis for the treatment, restoration and protection of groundwater nitrogen pollution.

## 2. Materials and Methods

### *2.1. Experimental Design*

#### 2.1.1. Experimental Materials

The experimental soil samples were collected on the floodplain of the Yellow River in Mengjin District, Luoyang City, Henan Province (Figure 1). The groundwater level in this area fluctuates frequently. Sample collection and processing were carried out by the requirements of the "Technical Specifications for Soil Environmental Monitoring" (HJ/T 166-2004). Sampling was performed using the quarter method, followed by drying, crushing and sieving, delineating three media, namely coarse sand, medium sand and fine sand. The pH value of the sand was between 8.5 and 9.3, and the organic matter content was between 0.241 and 1.070 $g \cdot kg^{-1}$. The basic physical and chemical properties of the soil are shown in Table 1. The water used in the laboratory is ultrapure water made by the German Millipore ultrapure water machine.

#### 2.1.2. Experimental Device

The experiment designed three plexiglass columns with the following exact specifications: the inner diameter was 20 cm, the height was 110 cm, the top was open, and the opening of the glass column was covered with plastic film; the bottom was connected to a pressure-measuring tube and a Markov flask through a three-way valve. Between the Markov flask and the cylinder, a peristaltic pump was equipped to control the water level to simulate the process of groundwater fluctuation (rising–falling); the organic glass column was equipped with four sampling ports from top to bottom, at 15, 25, 35, and 45 cm away from the bottom of the column; adjacent points were separated by 10 cm. The sampling points were equipped with a Rhizon solution sampler (inner diameter: 1 mm); we covered the top and bottom of each column with 5 cm of quartz sand (diameter 2~3 mm), to ensure that the water level rose and fell uniformly. The experimental device is shown in Figure 2.

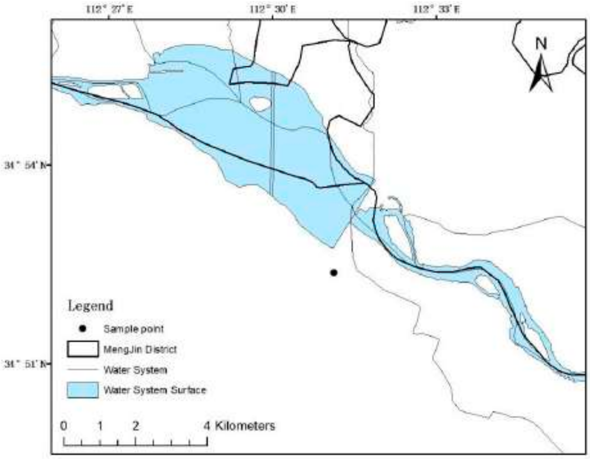

**Figure 1.** Location of sampling points.

**Table 1.** Soil particle composition and its parameters.

| **Serial Number** | **Sample** | **Particle Size (mm)** | **pH** | **Organic Matter Content ($g \cdot kg^{-1}$)** |
|---|---|---|---|---|
| 1 | Coarse sand | 0.5–1.0 | 8.5 | 0.241 |
| 2 | Medium sand | 0.25–0.5 | 8.8 | 0.587 |
| 3 | Fine sand | 0.125–0.25 | 9.3 | 1.070 |

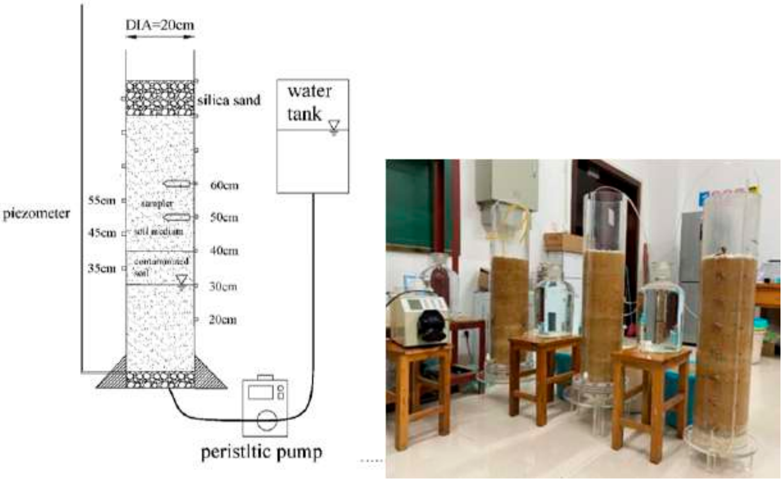

**Figure 2.** Schematic diagram of the experimental device.

### 2.1.3. Experimental Method

First, the experiments were conducted using soil from different media to fill the columns, filled with distilled water and stabilized at a 30 cm scale at the initial water level. Then, potassium nitrate and ammonium chloride solutions were injected from the top of the column. Three days later, we took out the water sample, and adjusted the water level using a peristaltic pump, raising its height by 10 cm each time until the water level reached 50 cm; after that, we decreased the water level by 10 cm each time, until the water level dropped to 10 cm. Finally, we raised the water level again, by 10 cm each time, until it reached 30 cm. The water levels during the experimental period were 30, 40, 50, 40, 30, 20, 10, 20, and 30 cm, respectively. Each water level was maintained for 3 d, and the change in the water level over time is shown in Figure 3, with the experiment using 24 d as a complete change period. The investigation was carried out for two cycles.

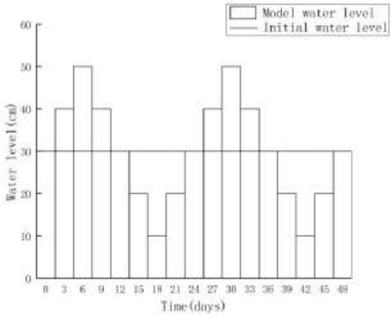

**Figure 3.** Time variation of water level.

Before each water level change, water samples were collected at four sampling ports using a diaphragm vacuum pump and a soil solution sampler to measure the concentrations of three forms of ammonium nitrogen, nitrate nitrogen and nitrite nitrogen.

### *2.2. Numerical Model*

HYDRUS-1D is widely used in saturated-unsaturated zones of water, heat and solute transport to study the process of nitrogen migration and the transformation in the fluctuation zone at the groundwater level. In this paper, based on indoor physical experiments, a numerical model of nitrogen migration and change in the Vadose zone–saturated zone coupled with water transport and solute transport, was constructed using HYDRUS-1D.

#### 2.2.1. Mathematical Model

- Water Movement Model.

The mathematical model of water movement in the water level fluctuation zone can be expressed as the Richards equation, as follows:

$$C(h)\frac{\partial \theta}{\partial t} = \frac{\partial}{\partial z}\left[K(h)[\frac{\partial h}{\partial t} - \cos(\alpha)]\right] - S(z,t) \tag{1}$$

where $C(h)$ is the water capacity (cm$^{-1}$); $K(h)$ is the hydraulic conductivity (cm/d); $h$ is the negative pressure (cm); $z$ represents the position coordinates in the parallel water flow direction (cm); $t$ is the time (d); $\alpha$ is the angle between the water flow direction and the vertical (°); $\theta$ is the volumetric water content (cm$^3$/cm$^3$); and $S(z,t)$ is the water absorption strength of plant roots (cm$^3$/cm$^3$·d$^{-1}$).

- Solute transport model in the Vadose zone.

The solute transport model only considers the behavioral characteristics of convection, diffusion, adsorption, degradation, etc., and uses the traditional convection–diffusion equation to describe the transport process. The equation is expressed as:

$$\frac{\partial}{\partial t}(\theta C) = \frac{\partial}{\partial z}(\theta D_L \frac{\partial C}{\partial z} - vC) - \rho_b \frac{\partial(\rho_s K_L C)}{\partial t} - C_0 \exp(-kt) \tag{2}$$

where $C$ is the solute concentration in the liquid phase (mg/L); $D_L$ is the longitudinal dispersion coefficient (cm/d); $v$ is the Darcy flow velocity (cm/d); $\rho_b$ is the soil bulk density (mg/cm); $\rho_s$ is the soil bulk density (mg/cm$^3$); $K_L$ is the adsorption distribution coefficient ($cm^3/g$); $C_0 \exp(-kt)$ is the source-sink term ($cm^3/cm^3 \cdot d^{-1}$); the others are the same as above.

- Nitrogen migration and transformation model.

The transport model of nitrogen in the soil varies according to the different forms of nitrogen. The transport and transformation process of $NH_4{}^+$ is mainly subjected to adsorption and nitrification. The equation is as follows:

$$\begin{cases} \frac{\partial(\theta c_1)}{\partial t} = \frac{\partial}{\partial z}\left(\theta D_L \frac{\partial c_1}{\partial z}\right) - \frac{\partial}{\partial z}(V c_1) - \rho_b \frac{\partial(\rho_s k_e c_1)}{\partial t} - k_1 \theta c_1 & \\ c_1(Z,0) = c_{10}(Z) & 0 \le Z \le L, t = 0 \\ -\left(\theta D_L \frac{\partial c_1}{\partial z} - q c_1\right) = \varepsilon(t) c_0 & Z = 0, t = 0 \\ c_1(L,t) = c_1 L & Z = L, t > 0 \end{cases} \tag{3}$$

Meanwhile $NO_2{}^-$ and $NO_3{}^-$ are mainly affected by nitrification and denitrification, and the equation is as follows:

$$\begin{cases} \frac{\partial(\theta c_i)}{\partial t} = \frac{\partial}{\partial z}\left(\theta D_L \frac{\partial c_i}{\partial z}\right) - \frac{\partial}{\partial z}(v_i c_i) - k_i \theta c_i & \\ c_i(Z,0) = c_{i0}(Z) & 0 \le Z \le L, t = 0 \\ c_i(0,t) = c_{i0}(t) & Z = 0, t > 0 \\ c_i(L,t) = c_i L & Z = L, t > 0 \end{cases} \tag{4}$$

where $\theta$ is the soil volume water content ($cm^3/cm^3$); $c_1$ is the soil solution $NH_4{}^+$ concentration (mg/L); $D_L$ is the longitudinal diffusion coefficient (cm/d); $k_e$ is the adsorption distribution coefficient ($cm^3/g$) for $NH_4{}^+$ in soil; $k_1$, $k_2$ are the denitrification rate constants ($d^{-1}$) for $NH_4{}^+$ and $NO_2{}^-$, respectively; $c_{10}(t)$ is the soil $NH_4{}^+$ initial concentration (mg/L); $c_0$ is the inlet solution $NH_4{}^+$ concentration (mg/L); $c_{1L}$ is the diving $NH_4{}^+$ concentration (mg/L); $c_2$,$c_2$ are the $NO_2{}^-$ and $NO_3{}^-$ concentration (mg/L), respectively; $k_3$ is the denitrification rate constant ($d^{-1}$); $c_{20}(z)$, $c_{30}(z)$ are the soil $NO_2{}^-$ and $NO_3{}^-$ initial concentration (mg/L), respectively; and $c_{2L}$,$c_{3L}$ are the diving $NO_2{}^-$ and $NO_3{}^-$ concentration (mg/L), respectively. No nitrogen input through the water.

### 2.2.2. Initial Conditions and Boundary Conditions

- Initial conditions.

At the initial moment, the water level was set to 30 cm, and the initial concentration of pollutants is shown in Table 2.

**Table 2.** Initial concentration of pollutants.

| Intake | Coarse Sand | | | Medium Sand | | | Fine Sand | | |
|---|---|---|---|---|---|---|---|---|---|
| | **Nitrite Nitrogen** | **Nitrate** | **Ammonium Nitrogen** | **Nitrite Nitrogen** | **Nitrate** | **Ammonium Nitrogen** | **Nitrite Nitrogen** | **Nitrate** | **Ammonium Nitrogen** |
| 15 cm | 0.19 | 74.85 | 6.17 | 0.37 | 35.81 | 1.97 | 0.70 | 0.55 | 0.08 |
| 25 cm | 0.15 | 77.14 | 6.97 | 0.27 | 36.47 | 3.07 | 0.84 | 2.20 | 0.09 |
| 35 cm | 0.37 | 47.56 | 7.03 | 0.36 | 78.39 | 11.87 | 0.44 | 12.61 | 5.14 |
| 45 cm | 0.33 | 45.25 | 8.23 | 0.25 | 84.41 | 12.61 | 0.49 | 76.77 | 9.76 |

- Boundary conditions.

1. Water transport and boundary conditions.

According to the experimental model, the upper boundary was in direct contact with the atmosphere and was set as the atmospheric boundary. The lower boundary was set as the variable head boundary due to the rise and fall of the water level.

2. Solute transport boundary.

According to the model, the upper boundary condition was the pollutant concentration boundary, and the lower boundary condition was the zero concentration gradient boundary. In the model setting, the primary considerations were adsorption and desorption, as well as nitrification and denitrification.

### 2.2.3. Model Parameters

The parameters of the numerical model mainly included soil hydraulic parameters and solute transport parameters. The initial values of the soil hydraulic parameters were determined according to the soil medium hydraulic parameter database of the Hydrus-1D software. The initial values of solute transport parameters were based on the measured results of this physical experiment, and the practical value was determined. The inverse solution module of the Hydrus-1D software was used for inversion to obtain the final parameters of the numerical model (Tables 3 and 4).

**Table 3.** Soil and water characteristic parameters.

| **Parameter** | **$\theta r$ Residual Volume Water Content** | **$\theta s$ Saturated Volume of Water Content** | **$\alpha$/cm$^{-1}$ Soil Moisture Characteristic Parameters** | **$n$ Soil Moisture Characteristic Index** | **$Ks$/(cm·d$^{-1}$) Saturated Hydraulic Conductivity** |
|---|---|---|---|---|---|
| Coarse sand | 0.045 | 0.43 | 0.1450 | 2.68 | 712.8 |
| Medium sand | 0.051 | 0.42 | 0.1045 | 2.08 | 550.0 |
| Fine sand | 0.057 | 0.41 | 0.1240 | 2.28 | 350.2 |

**Table 4.** Solute transport parameters.

| **Medium** | **Solute** | **$\rho$/mg·cm$^{-3}$ Bulk Density** | **$Disp$/cm Longitudinal Diffusion** | **$D$/cm$^2$·d$^{-1}$ Solute Diffusion Coefficient** | **$Kd$/cm$^3$·mg$^{-1}$ Adsorption Coefficient** |
|---|---|---|---|---|---|
| Coarse sand | Nitrite Nitrogen | 1600 | 1.568 | 1.29085 | 0.000256 |
| | Nitrate | | | 1.69085 | 0.001584 |
| | Ammonium Nitrogen | | | 1.69085 | 0.008779 |
| Medium sand | Nitrite Nitrogen | 1800 | 1.233 | 1.29085 | 0.000103 |
| | Nitrate | | | 1.69085 | 0.000413 |
| | Ammonium Nitrogen | | | 1.69085 | 0.008895 |
| Fine sand | Nitrite Nitrogen | 1800 | 1.116 | 1.29085 | 0.000767 |
| | Nitrate | | | 1.69085 | 0.003094 |
| | Ammonium Nitrogen | | | 1.69085 | 0.008976 |

### 2.2.4. Calibration and Evaluation of the Model

The reliability was verified and analyzed by inputting the solute transport parameters and soil hydraulic parameters through the HYDRUS-1D software, and the simulation's accuracy was evaluated by the coefficient of determination $R^2$, and the root mean square error ($RMSE$). The closer the coefficient of determination $R^2$ was to 1, the closer the root mean square error ($RMSE$) was to 0, which means that the model simulation results and the measured results of nitrogen had higher fitting accuracy. The calculation formula is:

$$R^2 = \frac{\sum_{i=1}^{n}(\hat{y_i} - \overline{y})^2}{\sum_{i=1}^{n}(y_i - \overline{y})^2} \tag{5}$$

$$RMSE = \sqrt{\frac{1}{N}\sum_{i=1}^{N}(S_i - M_i)^2} \tag{6}$$

where $S_i$ and $M_i$ are simulated and measured values, respectively; $N$ is the number of samples.

According to the simulation results of the numerical model of nitrogen migration and transformation in the water level fluctuation zone, the simulated values of ammonia nitrogen, nitrate nitrogen and nitrite nitrogen are shown in Figures 4–6, and the model fitting results are shown in Table 5. The correlation coefficients are mostly above 0.8.

The root mean square error (*RMSE*) is small. Except for the significant simulation error of individual pollutants, the simulation results of the numerical model fit well with the measured results, indicating that the numerical model can better reflect the nitrogen transfer and transformation process under the fluctuation of the groundwater level.

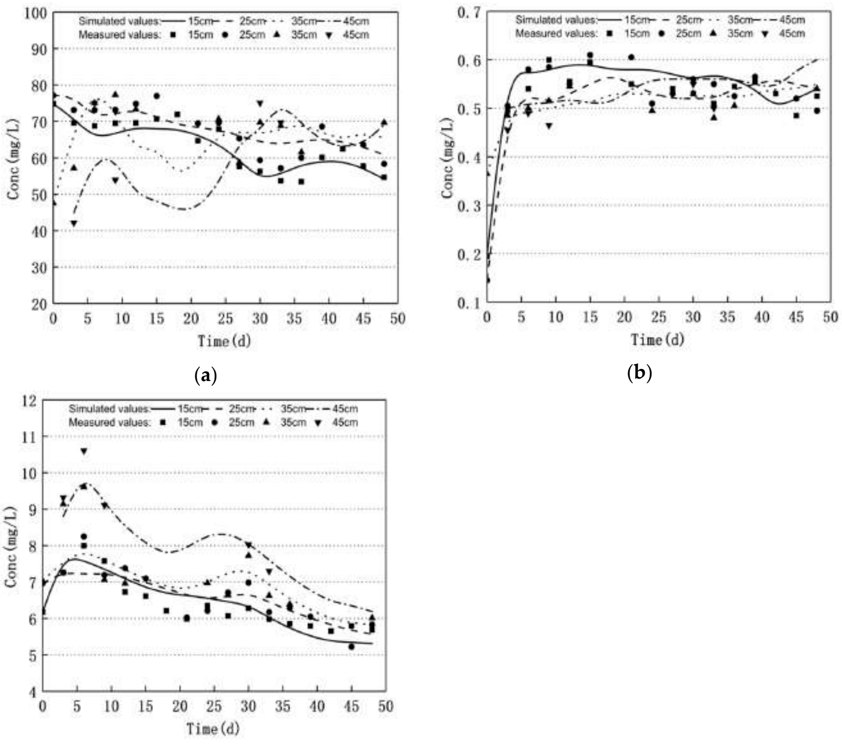

(**a**) (**b**)

(**c**)

**Figure 4.** The process of nitrogen change in coarse sand ((**a**) nitrate nitrogen; (**b**) nitrite nitrogen; (**c**) ammonium nitrogen).

**Table 5.** Model fitting effect.

| Soil Media | Pollutants | Decisive Factor $R^2$ | *RMSE* |
|---|---|---|---|
| Coarse sand | Nitrite nitrogen | 0.71284 | 0.0883 |
| | Nitrate nitrogen | 0.70572 | 5.4257 |
| | Ammonia nitrogen | 0.82099 | 0.4863 |
| Medium sand | Nitrite nitrogen | 0.74610 | 0.0486 |
| | Nitrate nitrogen | 0.80656 | 9.1317 |
| | Ammonia nitrogen | 0.98810 | 0.5115 |
| Fine sand | Nitrite nitrogen | 0.87036 | 0.0309 |
| | Nitrate nitrogen | 0.98398 | 2.7137 |
| | Ammonia nitrogen | 0.97552 | 0.3860 |

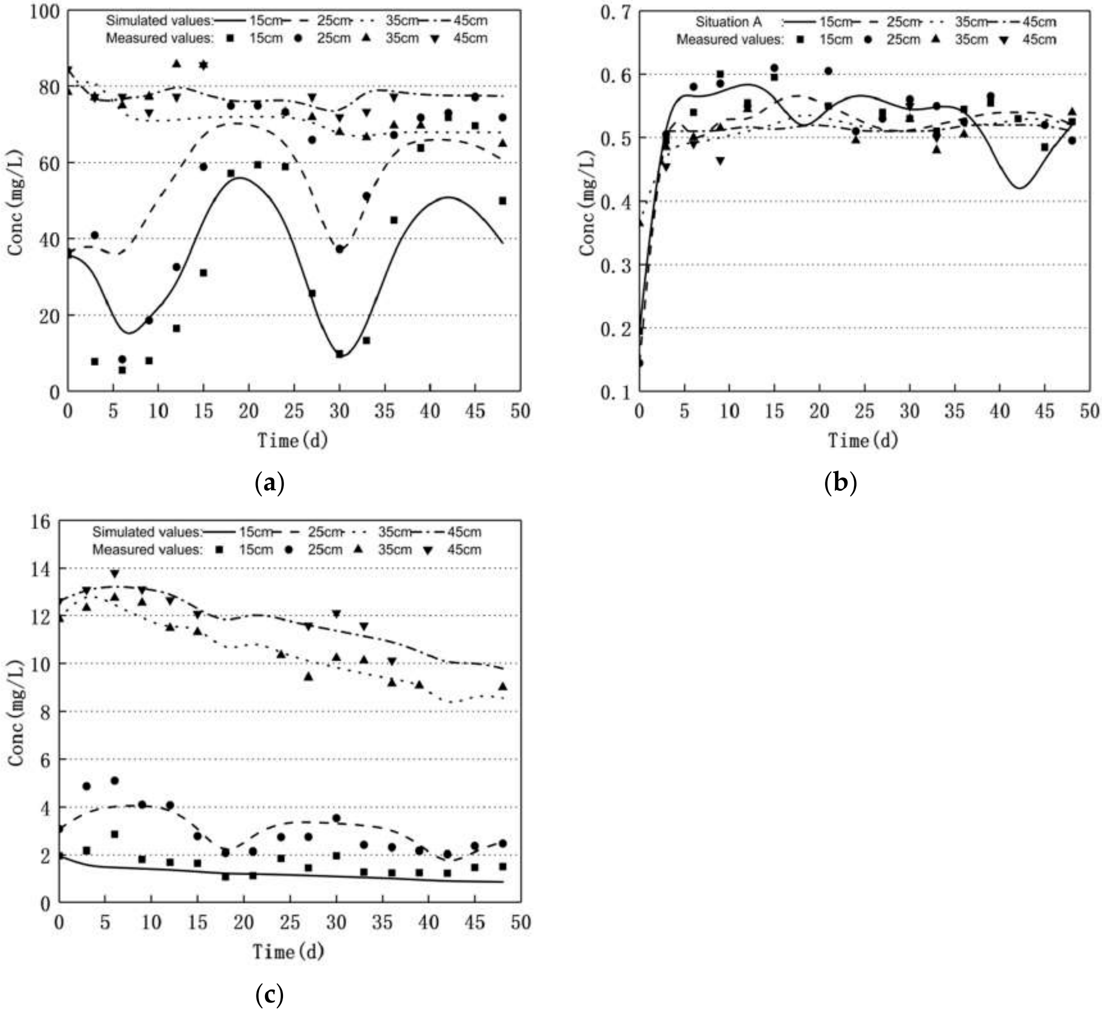

(**a**) (**b**)

(**c**)

**Figure 5.** The process of nitrogen change in medium sand ((**a**) nitrate nitrogen; (**b**) nitrite nitrogen; (**c**) ammonium nitrogen).

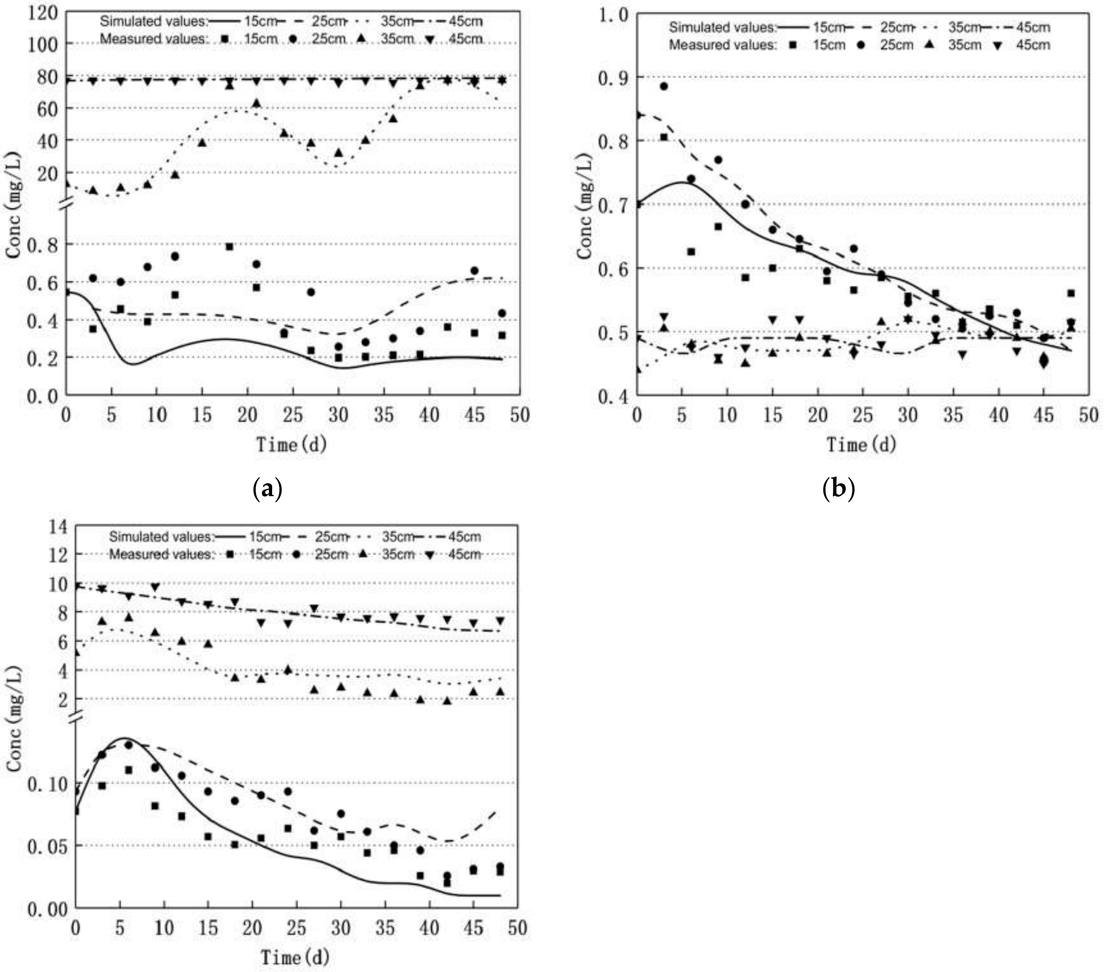

(**a**) (**b**) (**c**)

**Figure 6.** The process of nitrogen change in fine sand ((**a**) nitrate nitrogen; (**b**) nitrite nitrogen; (**c**) ammonium nitrogen).

## 3. Results and Discussion

### *3.1. Nitrogen Changes and Model Validation*

The process curves of the measured and simulated results of ammonia nitrogen, nitrate nitrogen and nitrite nitrogen in the coarse sandy soil column under the condition of water level fluctuation are shown in Figure 4.

In the 15 cm and 25 cm sampling ports in the coarse sand column, $NO_3^-$-N showed a decreasing trend in the rising stage of the water level, with a decrease of 8.55% on average, the maximum decrease of 14.94% in the second cycle of the second rising stage of the water level, and the minimum decrease of 2.27% in the first rising stage of the second cycle of the water level. The concentration of $NO_3^-$-N showed an increasing trend in the declining water level stage, with an average increase of 9.10%, a maximum increase of 15.47% and a minimum increase of 4.62%, and the second fluctuation cycle was more obvious than the first fluctuation cycle of nitrate heel fluctuation. The average increase of $NH_4^+$-N concentration was 9.16% at the stage of the water level rise, and the average decrease of $NH_4^+$-N concentration was 14.355% at the stage of water level fall, and the fluctuation change was more obvious in the first cycle. The concentration of $NO_2^-$-N was much smaller than that of the $NO_3^-$-N and $NH_4^+$-N concentrations, and $NO_2^-$-N showed fluctuating changes and eventually stabilized.

The process curves of the measured and simulated results of ammonia nitrogen, nitrate nitrogen and nitrite nitrogen in the medium sand soil column under the water level fluctuation conditions are shown in Figure 5.

In the medium sand column, the trend of $NO_3^-$-N was similar to that of the coarse sand soil column, with insignificant changes in concentrations at the 35 cm and 45 cm sampling ports, and obvious fluctuation trends at the 15 cm and 25 cm sampling ports. The concentration of $NO_3^-$-N at the 15 cm sampling port decreased by 780.30% on average, especially during the first water level rise in the first cycle. The concentration of $NO_2^-$-N was fluctuating at the beginning and stabilized later.

The process curves of the measured and simulated results of ammonia nitrogen, nitrate nitrogen and nitrite nitrogen in the fine sandy soil column under the condition of water level fluctuation are shown in Figure 6.

In the fine sand soil column, the trend of the $NO_3^-$-N concentration changes at the 15 cm, 25 cm and 35 cm sampling ports were basically the same, and the decreases at 15 cm, 25 cm and 35 cm were 25.93%, 68.05% and 19.19, respectively, during the water level rise stage, and the increases were at 15 cm, 25 cm and 35 cm during the water level fall stage. The trends of $NH_4^+$-N concentrations at the 15 cm, 25 cm and 35 cm sampling ports were basically the same, and the concentrations at the 45 cm sampling port did not change much, and the increases at the water level rising stage were 32.44%, 23.39% and 27.03% for 15 cm, 25 cm and 35 cm, respectively, and the decreasing water level for the $NO_2^-$-N concentration was low and stabilized after fluctuating changes.

Figures 4–6 show the actual measurement process curve of ammonia nitrogen, nitrate nitrogen and nitrite nitrogen under the conditions of water level fluctuation. When the water level rises, the dissolved oxygen content decreases, and the $NH_4^+$-N concentration should fall. Still, denitrifying bacteria become active and dominant under hypoxic conditions, promoting the increase in the $NH_4^+$-N concentration and the significant decrease in the $NO_3^-$-N concentration. When the water level drops, the dissolved oxygen content increases and nitrification plays a central role. The concentration of $NO_3^-$-N increases significantly. However, due to the strong adsorption of the soil, the concentration of $NH_4^+$-N in the free water of the soil solution decreases [43,44]. Nitrite nitrogen, in the three media, fluctuated and eventually stabilized, but its concentration was much smaller than the concentrations of $NO_3^-$-N and $NH_4^+$-N. Before the water level rises, when the dissolved oxygen is sufficient, the reproduction rate of nitrifying bacteria is slower than that of nitrosating bacteria; at this time, the nitrosation reaction dominates, causing the accumulation of $NO_2^-$-N, resulting in an increased concentration of $NO_2^-$-N in the soil solution during the rising water level stage. During the falling phase of the water level, nitrification dominates, a lot of $H^+$ is produced in the solution, and the soil solution becomes weakly acidic, which strengthens the conversion of nitrite to nitrate. $NO_2^-$-N no longer accumulates, and the concentration gradually decreases [29,45,46]. In the initial stage, the increase in $NO_2^-$-N satisfies coarse sand, then medium sand, then fine sand. The more significant the particle size is, the more particle surfaces there are that microbial flocs can come into contact with, and more microbes can participate in the nitrification reaction. With a stronger microbial nitrification ability, it is understood that the nitrification ability of microbial flocs will increase with the increase in particle size [47].

## *3.2. Scenario Simulation*

### 3.2.1. Increasing Water Level Fluctuation

Scenario 1 is set to: keep the initial pollutant concentration unchanged, and increase the water level fluctuation range. That is, the initial water level is set to 30 cm, and the height is raised by 15 cm at a time, and then rises twice until the water level reaches 60 cm; then it is dropped by 15 cm each time and drops four times until the water level drops to 0 cm; finally, the water level is raised again twice, by 15 cm each time, until it reaches 30 cm, which is the initial water level. The comparison chart of water level changes is shown in Figure 7, recorded as situation A.

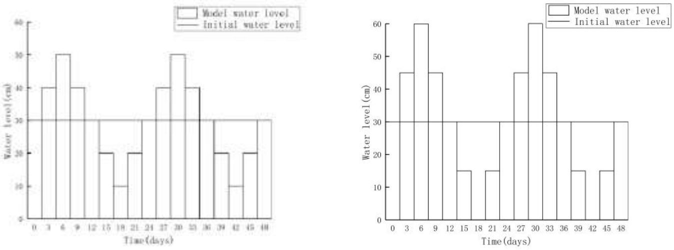

**Figure 7.** Comparison of water level changes.

Synchronously with the previous experiment scenario of groundwater level fluctuation, nitrogen migration and transformation (henceforth referred to as the fluctuation experiment), the simulation period is set to two by increasing the amplitude of the water level fluctuation, and the range of solute concentration in the water body increases. The model is built and run according to the scenario, and the simulation result is shown in Figures 8–10.

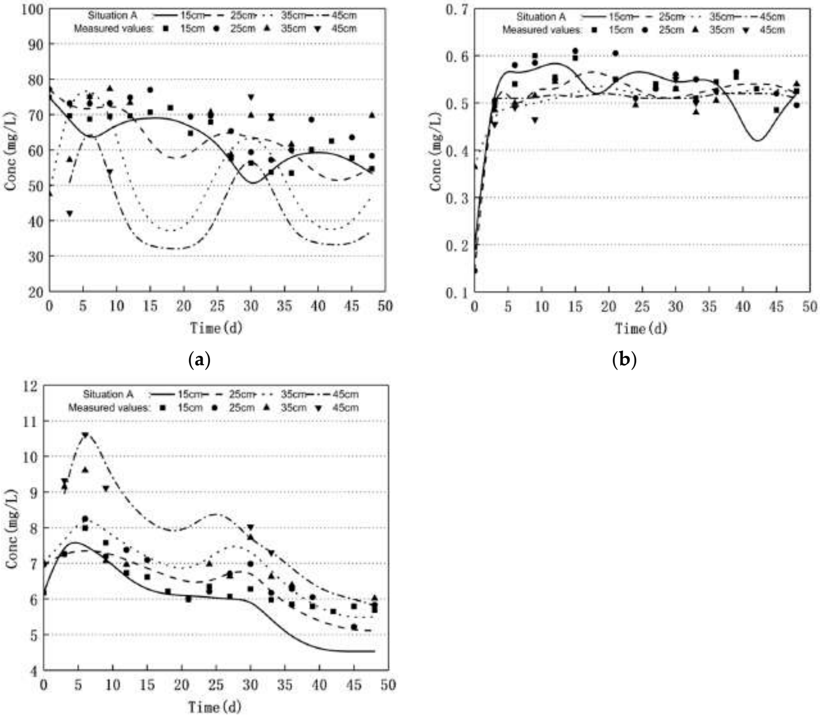

(**a**) (**b**)

(**c**)

**Figure 8.** The measured results of coarse sand and the process of dynamic change of nitrogen in situation A ((**a**) nitrate nitrogen; (**b**) nitrite nitrogen; (**c**) ammonium nitrogen).

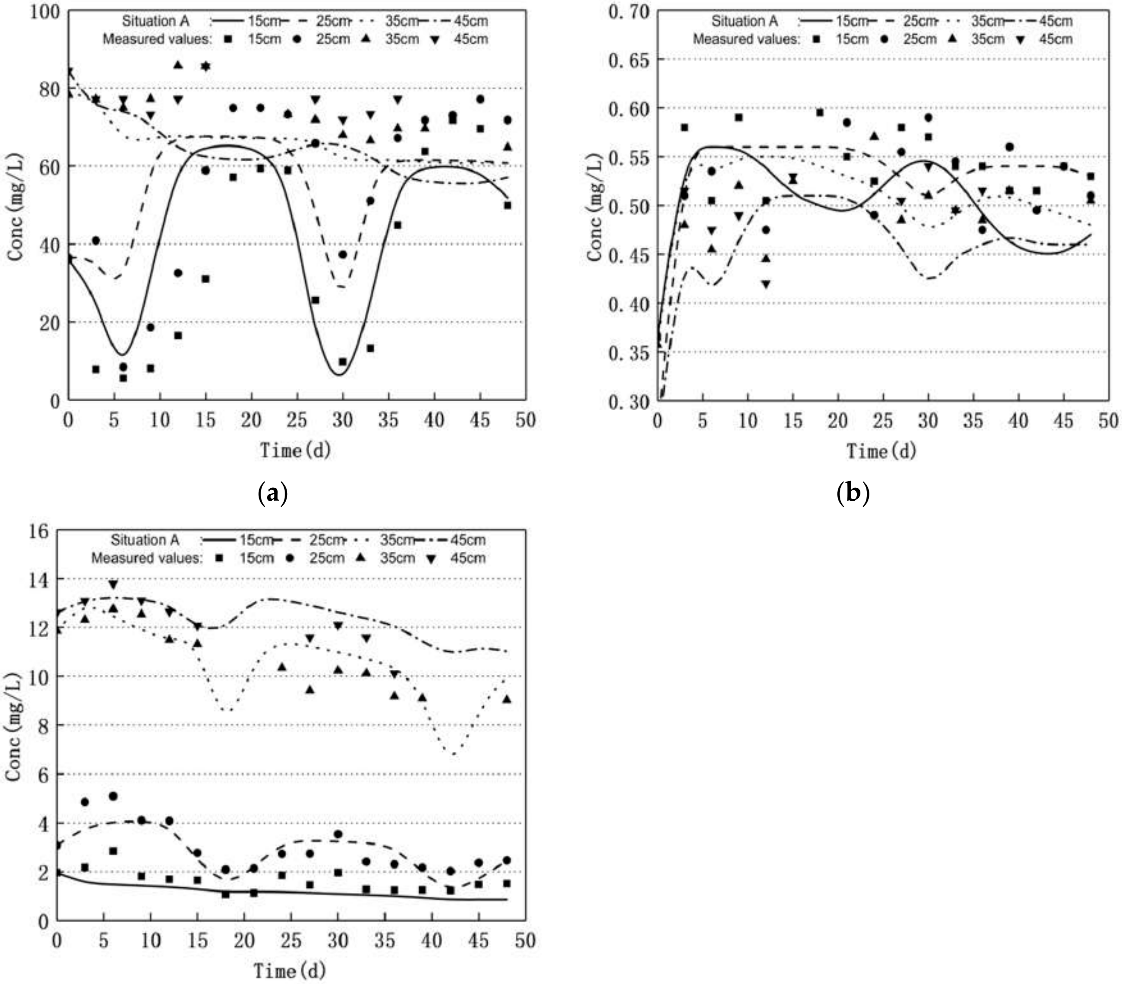

(**a**)

(**b**)

(**c**)

**Figure 9.** The measured results of medium sand and the dynamic process of nitrogen in situation A ((**a**) nitrate nitrogen; (**b**) nitrite nitrogen; (**c**) ammonium nitrogen).

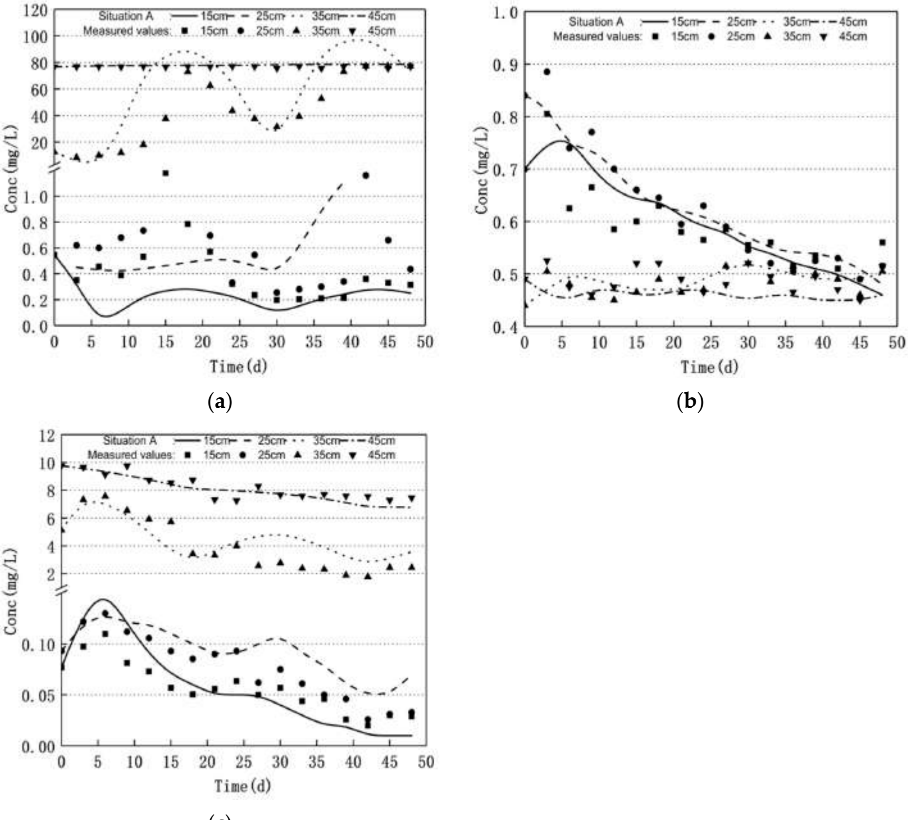

(**a**) (**b**)

(**c**)

**Figure 10.** The measured results of fine sand and the dynamic process of nitrogen in situation A ((**a**) nitrate nitrogen; (**b**) nitrite nitrogen; (**c**) ammonium nitrogen).

The comparison of the standard deviation of nitrogen concentration obtained by the three media simulations is shown in Table 6.

**Table 6.** Scenario A model standard deviation comparison.

| | Observation Hole | Coarse Sand | | Medium Sand | | Fine Sand | |
|---|---|---|---|---|---|---|---|
| | | **Fluctuation Experiment** | **Situation A** | **Fluctuation Experiment** | **Situation A** | **Fluctuation Experiment** | **Situation A** |
| Nitrite nitrogen | 15 cm | 0.0249 | 0.0488 | 0.0348 | 0.0384 | 0.0838 | 0.0896 |
| | 25 cm | 0.0197 | 0.0262 | 0.0141 | 0.0168 | 0.1037 | 0.0924 |
| | 35 cm | 0.0159 | 0.0135 | 0.0261 | 0.0263 | 0.0166 | 0.0159 |
| | 45 cm | 0.0276 | 0.0047 | 0.0255 | 0.0328 | 0.0107 | 0.0072 |
| Nitrate | 15 cm | 5.4152 | 6.2294 | 16.0273 | 22.4563 | 0.0921 | 0.0807 |
| | 25 cm | 4.2269 | 6.9961 | 12.8282 | 15.5376 | 0.0932 | 0.3326 |
| | 35 cm | 5.2402 | 14.0076 | 3.8663 | 4.4202 | 24.2231 | 31.5546 |
| | 45 cm | 9.5118 | 11.4918 | 1.9142 | 6.0021 | 0.417 | 0.4754 |
| Ammonium Nitrogen | 15 cm | 0.7797 | 1.0168 | 0.2074 | 0.2113 | 0.0422 | 0.0441 |
| | 25 cm | 0.5452 | 0.7755 | 0.7561 | 0.9278 | 0.027 | 0.0248 |
| | 35 cm | 0.6154 | 0.875 | 1.4036 | 1.8423 | 1.2271 | 1.3702 |
| | 45 cm | 1.0365 | 1.4005 | 1.1279 | 0.8256 | 0.8747 | 0.8622 |

Table 6 shows that the increase in the fluctuation range of water level can effectively enlarge solute fluctuation.

Water level fluctuations have different effects on the fluctuation range of nitrogen concentration in the three media. When the fluctuation range of water level increases by 5 cm, the fluctuation range of nitrogen in the coarse sand medium increases by 37.52% on average, compared to the fluctuation experiment scenario; the nitrogen concentration in the medium sand medium is increased by 37.52%. The fluctuation range increased by 31.40% on average; the fluctuation range of the nitrogen concentration in the fine sand medium increased by 21.14% on average.

Table 6 shows that in the coarse sand, the fluctuation of the nitrogen concentration changes most significantly with the increase in the fluctuation range of the water level, followed by the medium sand, and the fine sand has the slightest change.

The impact of water level fluctuations on the three solutes is also different. The fluctuation range of the water level is expanded by 5 cm, and the fluctuation range of nitrite nitrogen, nitrate nitrogen and ammonium nitrogen in the coarse sand medium increases by 7.90%, 67.17%, and 37.49%, respectively. In the medium sand medium, the fluctuation range increased by 14.66%, 72.28%, and 7.26%, respectively. The fluctuation range of nitrite nitrogen in the fine sand medium decreased by 10.34%, while the fluctuation range of nitrate nitrogen and ammonium nitrogen increased by 72.17% and 1.62%, respectively.

Table 6 shows that among the three media, the fluctuation of the water level has the most significant effect on the fluctuation of nitrate nitrogen, and the influence on the fluctuation of nitrite nitrogen and ammonium nitrogen is relatively small.

### 3.2.2. Scenario of Reduced Water Level Fluctuation

Scenario 2 is set to: keep the initial pollutant concentration unchanged, and reduce the fluctuation of the water level. That is, the initial water level is set to 30 cm, and the height is raised by 5 cm each time, and then rises two times until the water level reaches 40 cm; it then starts to drop by 5 cm each time, and drops four times until the water level drops to 20 cm; finally, the water level rises again two times, by 5 cm each time, until it reaches 30 cm, which is the initial water level. The comparison chart of the water level changes is shown in Figure 11. It is recorded as situation B.

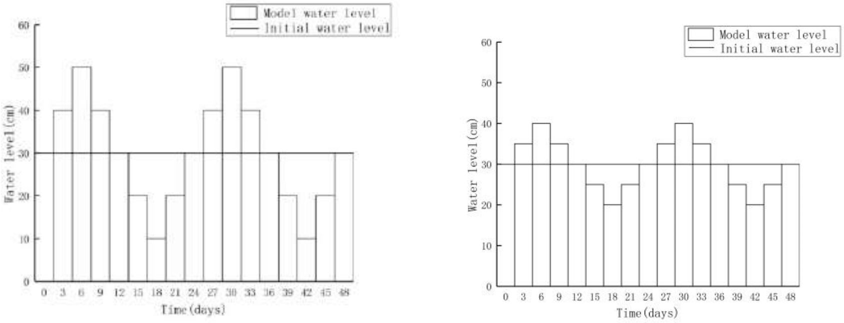

**Figure 11.** Comparison of Water Level Changes.

Similarly, the simulation period is set to 2. By increasing the fluctuation range of the water level, the variation range of the solute concentration in the water body is increased. The model is built and run according to the scenario, and the simulation result is shown in Figures 12–14.

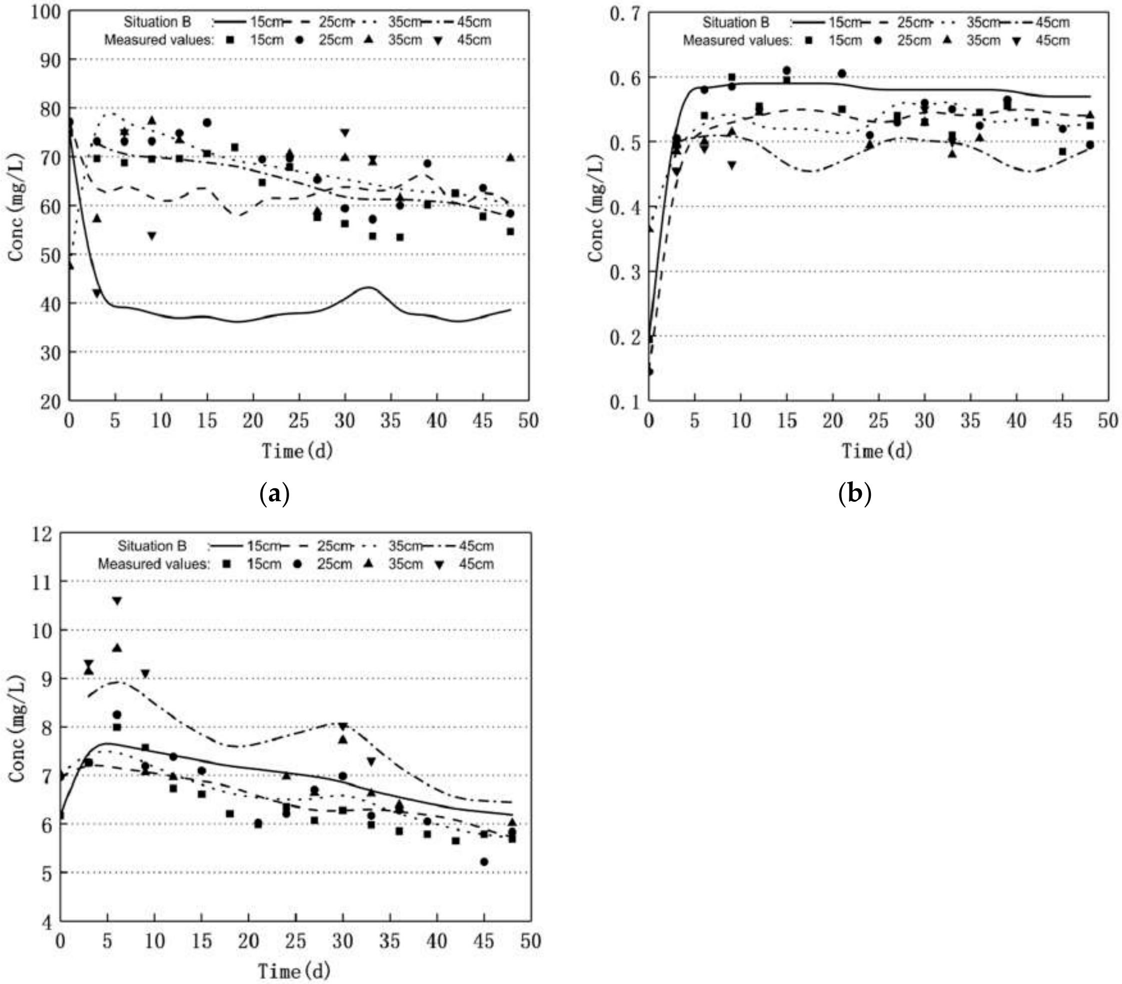

**(a)**

**(b)**

**(c)**

**Figure 12.** The measured results of coarse sand and the process of dynamic change of nitrogen in situation B ((**a**) nitrate nitrogen; (**b**) nitrite nitrogen; (**c**) ammonium nitrogen).

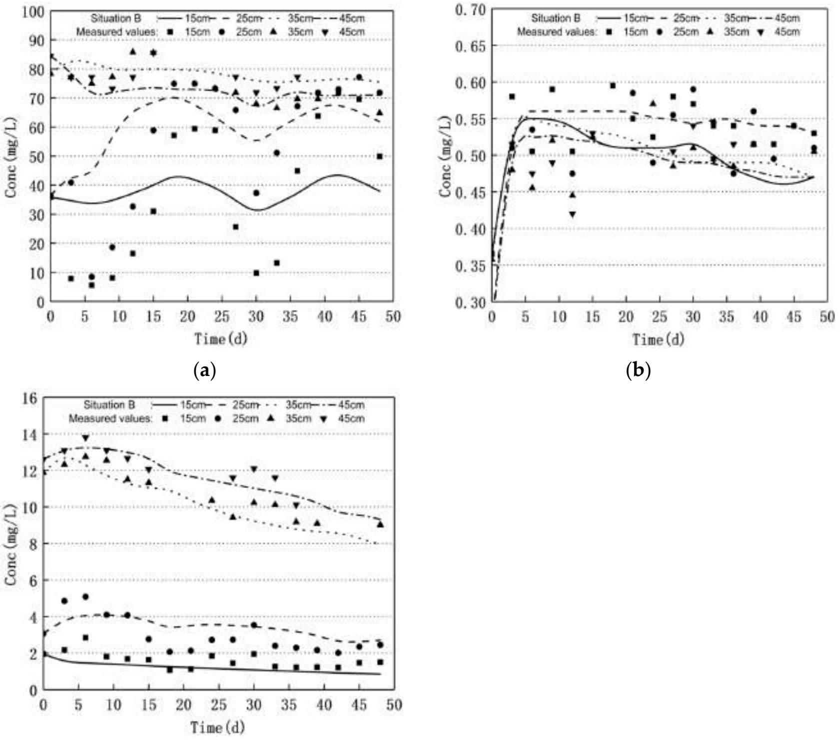

(**a**) (**b**)

(**c**)

**Figure 13.** The measured results of medium sand and the dynamic process of nitrogen in situation B ((**a**) nitrate nitrogen; (**b**) nitrite nitrogen; (**c**) ammonium nitrogen).

The comparison of the standard deviation of the nitrogen concentration obtained by the three media simulations is shown in Table 7.

**Table 7.** Scenario B model standard deviation comparison.

| | Observation Hole | Coarse Sand | | Medium Sand | | Fine Sand | |
|---|---|---|---|---|---|---|---|
| | | Fluctuation Experiment | Situation B | Fluctuation Experiment | Situation B | Fluctuation Experiment | Situation B |
| Nitrite Nitrogen | 15 cm | 0.0249 | 0.0063 | 0.0348 | 0.0316 | 0.0838 | 0.0758 |
| | 25 cm | 0.0197 | 0.0143 | 0.0141 | 0.0099 | 0.1037 | 0.1139 |
| | 35 cm | 0.0159 | 0.0183 | 0.0261 | 0.0266 | 0.0166 | 0.0148 |
| | 45 cm | 0.0276 | 0.0206 | 0.0255 | 0.0219 | 0.0107 | 0.0112 |
| Nitrate | 15 cm | 5.4152 | 2.1756 | 16.0273 | 4.0429 | 0.0921 | 0.1069 |
| | 25 cm | 4.2269 | 3.337 | 12.8282 | 8.1699 | 0.0932 | 0.0601 |
| | 35 cm | 5.2402 | 6.0552 | 3.8663 | 2.4465 | 24.2231 | 15.1679 |
| | 45 cm | 9.5118 | 4.4877 | 1.9142 | 2.658 | 0.417 | 0.3406 |
| Ammonium Nitrogen | 15 cm | 0.7797 | 0.4898 | 0.2074 | 0.2042 | 0.0422 | 0.0391 |
| | 25 cm | 0.5452 | 0.4511 | 0.7561 | 0.4871 | 0.027 | 0.029 |
| | 35 cm | 0.6154 | 0.5448 | 1.4036 | 1.4785 | 1.2271 | 1.0044 |
| | 45 cm | 1.0365 | 0.7817 | 1.1279 | 1.3127 | 0.8747 | 0.7587 |

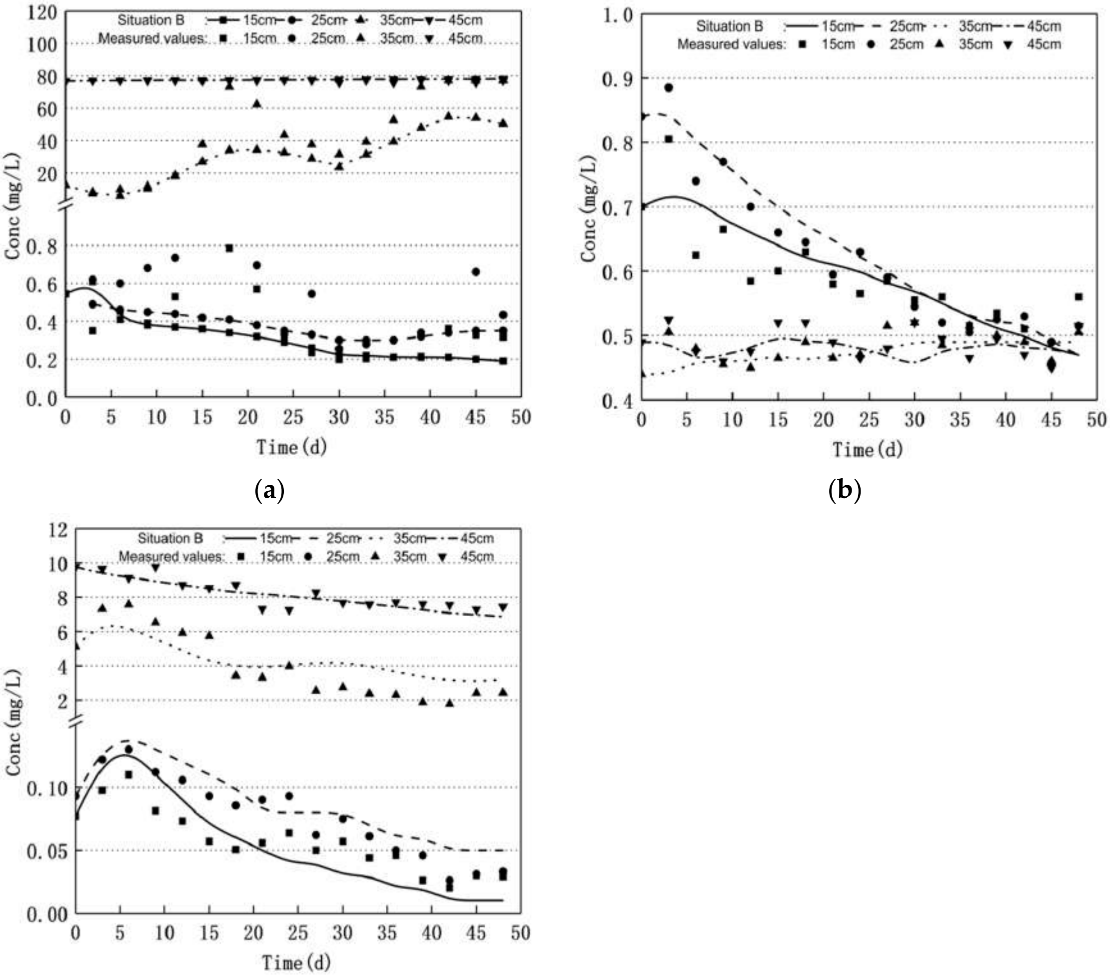

(**a**) (**b**) (**c**)

**Figure 14.** The measured results of fine sand and the dynamic process of nitrogen in situation B ((**a**) nitrate nitrogen; (**b**) nitrite nitrogen; (**c**) ammonium nitrogen).

Table 7 shows that the decrease in water level fluctuation can effectively reduce solute fluctuation.

Water level fluctuations have different effects on the fluctuation range of nitrogen concentration in the three media. When the fluctuation range of the water level decreases by 5 cm, the fluctuation range of nitrogen in the coarse sand medium is reduced by 36.74% on average, compared to the fluctuation experiment scenario. In the medium sand medium, the fluctuation range of the concentration of nitrogen decreased by 14.70% on average, while the fluctuation range of the nitrogen concentration in the fine sand medium decreased by 9.39% on average.

Table 7 shows that in the coarse sand, the fluctuation of the nitrogen concentration changes most significantly with the decrease in the fluctuation range of the water level, followed by the medium sand, and the fine sand demonstrates the most minor change.

The impact of water level fluctuations on the three solutes is also different. When the fluctuation range of the water level is reduced by 5 cm, the fluctuation ranges of nitrite nitrogen, nitrate nitrogen and ammonium nitrogen in the coarse sand medium are reduced by 28.07%, 29.55%, and 22.62%, respectively. In the medium sand medium, the average fluctuation range is reduced by 13.00%, 27.23%, and 3.85%, respectively. In the fine sand model, the fluctuation range is reduced by an average of 1.51%, 18.79%, and 7.86%, respectively.

Table 7 shows that among the three media, water level fluctuations have the most significant impact on the fluctuations of nitrate nitrogen, have less impact on the fluctuations of nitrite nitrogen and ammonium nitrogen, and the difference is the most obvious in the fine sand medium, followed by medium sand. This difference is not great in the coarse sand.

## 4. Conclusions

In this paper, through the experiment examining nitrogen migration and transformation in the groundwater fluctuating zone, we analyzed the nitrogen migration and transformation process. A numerical model of nitrogen migration and transformation in the groundwater level fluctuating zone was established with the help of the HYDRUS-1D model. The paper obtained the following main conclusions:

- Groundwater level fluctuations can significantly affect the nitrogen transport and transformation patterns in soil–groundwater. The nitrate nitrogen concentration increased and the ammonium nitrogen mass concentration decreased when the water level decreased. Moreover, the nitrate nitrogen mass concentration decreased and the ammonium nitrogen mass concentration increased when the water level increased; the nitrite nitrogen did not change significantly.
- In this study, indoor soil column experiments were combined with the Hydrus-1D software simulation prediction to simulate the theoretical values of the tri-nitrogen transformation process in indoor soil columns. Although simple, the software does not take into account the existence of non-homogeneous changes in the soil column, is not accurate enough, there are certain limitations, and the influence of biological processes on the transformation of pollutants has not been taken into account. Furthermore, there is still a certain gap with the actual results.
- As an important factor of the hydrological mechanism, the water level plays a vital role in the groundwater system, and the effect of the level and intensity of fluctuation of the groundwater level on the migration and transformation of nitrogen cannot be ignored. The change in water level will affect the water content in the soil, the state of water movement, the physical and chemical properties of soil and the state of the microorganisms, which in turn, will affect the migration and transformation of nitrogen in the soil.

**Author Contributions:** Conceptualization, Y.L. and J.Q.; methodology, Y.L., L.W. and X.Z.; software, L.W. and X.Z.; validation, Y.L., L.W. and J.Q.; writing—original draft preparation, Y.L. and L.W.; writing—review and editing, Y.L. and J.Q.; visualization, G.B. All authors have read and agreed to the published version of the manuscript.

**Funding:** This research was funded by the Doctoral Research Fund of North China University of Water Resources and Electric Power (40651) and the Key Project of Science and Technology Research of Henan Education Department (14A170006), and by the Key R&D and Promotion Projects in Henan Province (202102310012).

**Institutional Review Board Statement:** Not applicable.

**Informed Consent Statement:** Not applicable.

**Data Availability Statement:** Data are contained within the article.

**Conflicts of Interest:** The authors declare no conflict of interest.

## References

1. Matiatos, I. Nitrate source identification in groundwater of multiple land-use areas by combining isotopes and multivariate statistical analysis: A case study of Asopos basin (Central Greece). *Sci. Total Environ.* **2016**, *541*, 802–814. [CrossRef] [PubMed]
2. Fu, J.; Shan, J.; Yuan, Y.; Gao, Y.; Wu, R.; Yang, J. Comprehensive traceability of nitrogen pollution in the Shenfu section of Hunhe River Basin. *Acta Sci. Circumstantiae* **2018**, *38*, 2560–2567.
3. van der Schans, M.L.; Harter, T.; Leijnse, A.; Mathews, M.C.; Meyer, R.D. Characterizing sources of nitrate leaching from an irrigated dairy farm in Merced County, California. *J. Contam. Hydrol.* **2009**, *110*, 9–21. [CrossRef] [PubMed]
4. Rosenstock, T.S.; Liptzin, D.; Dzurella, K.; Fryjoff-Hung, A.; Hollander, A.; Jensen, V.; King, A.; Kourakos, G.; McNally, A.; Pettygrove, G.S.; et al. Agriculture's Contribution to Nitrate Contamination of Californian Groundwater (1945–2005). *J. Environ. Qual.* **2014**, *43*, 895–907. [CrossRef] [PubMed]
5. Meghdadi, A.; Javar, N. Quantification of spatial and seasonal variations in the proportional contribution of nitrate sources using a multi-isotope approach and Bayesian isotope mixing model. *Environ. Pollut.* **2018**, *235*, 207–222. [CrossRef] [PubMed]
6. Cui, N.; Liu, S. Comprehensive evaluation of soybean meal replacement based on RIAM model. *Feed. Res.* **2020**, *43*, 126–130.
7. Xiaoliang, J.; Xie, R.; Yun, H.; Lu, J. Quantitative identification of nitrate pollution sources and uncertainty analysis based on dual isotope ap-proach in an agricultural watershed. *Environ. Pollut.* **2017**, *229*, 586–594.
8. Burow, K.R.; Nolan, B.T.; Rupert, M.G.; Dubrovsky, N.M. Nitrate in groundwater of the United States, 1991–2003. *Environ. Sci. Technol.* **2010**, *44*, 4988–4997. [CrossRef]
9. Gu, B.; Ge, Y.; Chang, S.X.; Luo, W.; Chang, J. Nitrate in groundwater of China: Sources and driving forces. *Glob. Environ. Chang.* **2013**, *23*, 1112–1121. [CrossRef]
10. Stuart, M.; Gooddy, D.; Bloomfield, J.; Williams, A. A review of the impact of climate change on future nitrate concentrations in groundwater of the UK. *Sci. Total Environ.* **2011**, *409*, 2859–2873. [CrossRef]
11. Cheong, J.-Y.; Hamm, S.-Y.; Lee, J.-H.; Lee, K.-S.; Woo, N. Groundwater nitrate contamination and risk assessment in an agricultural area, South Korea. *Environ. Earth Sci.* **2011**, *66*, 1127–1136. [CrossRef]
12. Zhao, T.; Zhang, C.; Du, L.; Liu, B.; An, Z. Investigation of nitrate content in groundwater of seven provinces (cities) around the Bohai Sea. *Acta Agri-Environ. Sci.* **2007**, *2*, 779–783.
13. Zhao, Y.; Shao, M. Experimental study on nitrate-nitrogen migration in farmland under different fertilization conditions. *J. Agric. Eng.* **2002**, *18*, 37–40.
14. Filippis, G.D.; Ercoli, L.; Rossetto, R. A Spatially Distributed, Physically-Based Modeling Approach for Estimating Agricultural Nitrate Leaching to Groundwater. *Hydrology* **2021**, *8*, 8. [CrossRef]
15. Wild, L.M.; Mayer, B.; Einsiedl, F. Decadal Delays in Groundwater Recovery from Nitrate Contamination Caused by Low O2Reduction Rates. *Water Resour. Res.* **2018**, *54*, 9996. [CrossRef]
16. European Commission. Establishing a Framework for the Community Action in the Field of Water Policy. In *Directive 2000/60/EC of the European Parliament and of the Council of 23 October 2000*; European Commission: Brussels, Belgium, 2000.
17. Liu, M. *Migration and Transformation of Petroleum Hydrocarbons in the Envelope Zone with Numerical Simulation*; Jilin University: Jilin, China, 2014.
18. Guo, H.M.; Wang, Y.X.; Li, Y.M. Analysis of arsenic enrichment factors in groundwater in the arsenic poisoning area of Shan Yin water. *Environ. Sci.* **2003**, *4*, 60–67.
19. Sorensen, J.; Butcher, A.S.; Stuart, M.E.; Townsend, B.R. Nitrate fluctuations at the water table: Implications for recharge processes and solute transport in the Chalk aquifer. *Hydrol. Process.* **2015**, *29*, 3355–3367.
20. Hefting, M.J.C.; Clément, D.D.; Cosandey, A.C.; Bernal, S.; Cimpian, C.; Tatur, A.; Burt, T.P.; Pinay, G. Water table elevation controls on soil nitrogen cycling in riparian wetlands along a European climatic gradient. *Biogeochemistry* **2004**, *67*, 113–134.
21. Welch, H.L.; Green, C.; Coupe, R.H. The fate and transport of nitrate in shallow groundwater in northwestern Mississippi, USA. *Appl. Hydrogeol.* **2011**, *19*, 1239–1252. [CrossRef]
22. Jurado, A.; Borges, A.V.; Brouyère, S. Dynamics and emissions of N2O in groundwater: A review. *Sci. Total Environ.* **2017**, *584–585*, 207–218.
23. Yang, L.-P.; Li, N.; Zhang, J. Effect of pH on the transport and transformation of "tri-nitrogen" in shallow groundwater. *Chin. Agron. Bull.* **2017**, *33*, 56–60.
24. Zhang, Z.; Furman, A. Redox dynamics at a dynamic capillary fringe for nitrogen cycling in a sandy column. *J. Hydrol.* **2021**, *603*, 26899. [CrossRef]
25. Ashworth, D.J.; Shaw, G. Effects of moisture content and redox potential on in situ Kd values for radioiodine in soil. *Sci. Total Environ.* **2006**, *359*, 244–254. [CrossRef]
26. Li, X.; Yang, T.; Bai, S.; Xi, B.; Zhu, X.; Yuan, Z.; Wei, Y.; Li, W. Research on the Influence of Groundwater Level Fluctuation on the Transport of Nitrogen in Vadose Zone. *Agric. Environ. Sci. J.* **2013**, *32*, 2443–2450.
27. Zhang, D.; Fan, M.; Liu, H.; Wang, R.; Zhao, J.; Yang, Y.; Cui, R.; Chen, A. Effects of shallow groundwater table fluctuations on nitrogen in the groundwater and soil profile in the nearshore vegetable fields of Erhai Lake, southwest China. *J. Soils Sediments* **2019**, *20*, 42–51. [CrossRef]
28. Xin, L.; Rui, Z.; Li, M.; Peng, L.; Zhiping, L.; Zhukun, H.; Qiao, L.; Jinsheng, W. Research on Nitrate Nitrogen (Nitrate) Pollution Changes in the Process of Groundwater Level Rising. *China Environ. Sci.* **2021**, *41*, 232–238.

29. Jia, W.; Yin, L.; Zhang, M.; Zhang, J.; Zhang, X.; Gu, X.; Dong, J. Modified method for the estimation of groundwater evapotranspiration under very shallow water table con-ditions based on diurnal water table fluctuations. *J. Hydrol.* **2021**, *597*, 126193. [CrossRef]
30. Kamon, M.; Endo, K.; Katsumi, T. Measuring the k–S–p relations on DNAPLs migration. *Eng. Geol.* **2003**, *70*, 64–65. [CrossRef]
31. Nedrich, S.M.; Burton, G.A. Indirect effects of climate change on zinc cycling in sediments: The role of changing water levels. *Environ. Toxicol. Chem.* **2017**, *36*, 2456–2464. [CrossRef]
32. Davis, G.B.; Rayner, J.L.; Trefry, M.G.; Fisher, S.J.; Patterson, B.M. Measurement and Modeling of Temporal Variations in Hydrocarbon Vapor Behavior in a Layered Soil Profile. *Vadose Zone J.* **2005**, *4*, 265–273. [CrossRef]
33. Kamon, M.; Li, Y.; Endo, K.; Inui, T.; Katsumi, T. Experimental Study on the Measurement of S-p Relations of LNAPL in a Porous Medium. *Soils Found.* **2007**, *47*, 33–45. [CrossRef]
34. Xie, X.; Li, Y.; Xia, B.; Su, Y.; Gu, Q. Study on the hysteresis of saturation-capillary pressure relationship in sand media under fluctuating water level. *Acta Pedol. Sin.* **2011**, *48*, 286–294.
35. Li, X.; Li, J.; Xi, B.; Yuan, Z.; Zhu, X.; Zhang, X. Effects of groundwater level variations on the nitrate content of groundwater: A case study in Luoyang area, China. *Environ. Earth Sci.* **2015**, *74*, 3969–3983. [CrossRef]
36. Chen, A.; Lei, B.; Hu, W.; Wang, H.; Dan, Z. Temporal-spatial variations and influencing factors of nitrogen in the shallow groundwater of the nearshore vegetable field of Erhai Lake, China. *Environ. Ence Pollut. Res.* **2017**, *25*, 4858–4870. [CrossRef] [PubMed]
37. Farnsworth, C.E.; Voegelin, A.; Hering, J.G. Manganese oxidation induced by water table fluctuations in a sand column. *Environ. Sci. Technol.* **2012**, *46*, 277–284. [CrossRef] [PubMed]
38. Yang, Y. Research on Soil Pollutant Transport Model Considering Groundwater Level Fluctuations. Master's Thesis, Hebei Agricultural University, Baoding, China, 3 June 2015.
39. Zhang, X.; Wang, P.; Wang, T.; Yu, J.; Liu, X. Hydrochemical characteristics of shallow groundwater in Ejina Oasis and the relationship between water level and depth under water transport conditions. *South-to-North Water Divers. Water Conserv. Sci. Technol.* **2019**, *17*, 86–94.
40. Cao, W.; Yang, H.; Gao, Y.; Nan, T.; Wang, Z.; Xu, S. Prediction of groundwater quality evolution in Baoding Plain in the wa-ter-receiving area of the Middle Route of the South-to-North Water Transfer Project. *J. Hydraul. Eng.* **2020**, *51*, 924–935.
41. Tafteh, A.; Sepaskhah, A.R. Application of HYDRUS-1D model for simulating water and nitrate leaching from continuous and alternate furrow irrigated rapeseed and maize fields. *Agric. Water Manag.* **2012**, *113*, 19–29. [CrossRef]
42. Mo, X.; Peng, H.; Xin, J.; Wang, S. Analysis of urea nitrogen leaching under high-intensity rainfall using HYDRUS-1D. *J. Environ. Manag.* **2022**, *312*, 114900. [CrossRef]
43. Chang, C.; Entz, T. Nitrate Leaching Losses under Repeated Cattle Feedlot Manure Applications in Southern Alberta. *J. Environ. Qual.* **1996**, *25*, 145–153. [CrossRef]
44. Steffy, D.A.; Johnston, C.D.; Barry, D.A. Numerical Simulations and Long-Column Tests of LNAPL Displacement and Trapping by a Fluctuating Water Table. *J. Soil Contam.* **1998**, *7*, 325–356. [CrossRef]
45. Marshall, H.W.H. Ecology of Water-Level Manipulations on a Northern Marsh. *Ecology* **1963**, *44*, 331–343.
46. Wang, Y. Ammonia Nitrogen Adsorption-Desorption Characteristics of Sediments of Different Sizes in the Xiliao River. Master's Thesis, Liaoning Technical University, Liaoning, China, 15 September 2012.
47. Sasikala, S.; Tanaka, N.; Wah, H.W.; Jinadasa, K. Effects of water level fluctuation on radial oxygen loss, root porosity, and nitrogen removal in subsurface vertical flow wetland mesocosms. *Ecol. Eng.* **2009**, *35*, 410–417. [CrossRef]

applied sciences

MDPI

Article

# The Effects of the Long-Term Freeze–Thaw Cycles on the Forms of Heavy Metals in Solidified/Stabilized Lead–Zinc–Cadmium Composite Heavy Metals Contaminated Soil

**Zhongping Yang [1,2,3,*], Jiazhuo Chang [1,2,3], Xuyong Li [1,2,3], Keshan Zhang [1,2,3] and Yao Wang [1,4]**

[1] School of Civil Engineering, Chongqing University, Chongqing 400045, China; changjiazhuo@cqu.equ.cn (J.C.); lixuyong@cqu.edu.cn (X.L.); zhangkeshan1999@163.com (K.Z.); a_yao0218@163.com (Y.W.)
[2] Key Laboratory of New Technology for Construction of Cities in Mountain Area, Chongqing University, Ministry of Education, Chongqing 400045, China
[3] National Joint Engineering Research Center for Prevention and Control of Environmental Geological Hazards in the TGR Area, Chongqing University, Chongqing 400045, China
[4] China Machinery China Union Engineering Co., Ltd., Chongqing 400045, China
[*] Correspondence: yang-zhp@163.com; Tel./Fax: +86-(023)-65120728

**Abstract:** Heavy metals (HMs) exist in nature in different forms, and the more unstable the form of an HM, the higher its toxicity and bioavailability. The content of HMs in stable fractions can increase significantly through the stabilization/solidification (S/S) technology. Still, external environments such as freeze–thaw (F–T) cycles will affect the stability of HMs directly. Therefore, a long-term F–T study of S/S Pb–Zn–Cd composite HM-contaminated soil was conducted under six conditions (0, 3, 7, 14, 30, and 90 cycles) with each F–T cycle process up to 24 h. The improved Tessier method was employed, and the results show that the S/S technology makes HMs transform to a more stable fraction. Still, the transformation efficiency is different for each HM. More than 98% of lead and zinc were converted to stable forms, while for cadmium, there are only 75.1%. Meanwhile, the S/S HMs were rapidly transformed into unstable forms at 0–14 cycles, but after 14 cycles, the transformation speed was significantly reduced. Among stable forms, it is mainly that the carbonate-bound fraction of HMs changes to unstable forms, and the characteristic peaks of carbonate stretching vibration were found at 874 $cm^{-1}$, and 1420 $cm^{-1}$ by Fourier infrared spectroscopy proves the presence of carbonate-bound substances. As a result of this study, the change trend of contaminated soil with S/S HMs under the effect of long-term F–T cycle was revealed, and the crisis point of pollution prevention and control was found, which provides some theoretical basis for the safety of soil remediation project.

**Keywords:** long-term freeze–thaw cycles; composite heavy metal contamination; morphological analysis; solidification/stabilization

**Citation:** Yang, Z.; Chang, J.; Li, X.; Zhang, K.; Wang, Y. The Effects of the Long-Term Freeze–Thaw Cycles on the Forms of Heavy Metals in Solidified/Stabilized Lead–Zinc–Cadmium Composite Heavy Metals Contaminated Soil. *Appl. Sci.* **2022**, *12*, 2934. https://doi.org/10.3390/app12062934

Academic Editors: Bing Bai and Dibyendu Sarkar

Received: 6 February 2022
Accepted: 10 March 2022
Published: 13 March 2022

**Publisher's Note:** MDPI stays neutral with regard to jurisdictional claims in published maps and institutional affiliations.

**Copyright:** © 2022 by the authors. Licensee MDPI, Basel, Switzerland. This article is an open access article distributed under the terms and conditions of the Creative Commons Attribution (CC BY) license (https://creativecommons.org/licenses/by/4.0/).

## 1. Introduction

Because of considerable migration depth, complex migration mechanism, sizeable spatial variability, strong concealment, and resistance to degradation of heavy metals (HMs), its high-concentration and high-risk pollutants in the soil are extremely difficult to repair and manage and are called "chemical time bombs" [1–3]. In recent years, the remediation of soil HM pollution has been an environmental topic worthy of attention. Studies have shown that HM pollutants may cause changes in soil structure, such as colloidal corrosion between soil particles, decrease in cementation strength, increase in clay content, resulting in increased soil compression, reduced liquid, and plastic limits, reduced shear strength (the reduction can reach about 35%), increased permeability, and the decreased bearing capacity [4–6]. In addition, the non-degradability of HMs leads to their accumulation in plants, animals, and humans along the biological chain [7–11]. Both pose a threat to human safety and health; therefore, it is imperative to control soil

HM pollution [12]. There are two kinds of solutions to manage HM pollution in the soil. The first one is to directly reduce the concentration of HMs in the soil, and the second one is to reduce the possibility of HM migration. That means fixing them in place and reducing their biotoxicity by special treatments [13,14]. In this context, a series of treatment methods for HM-contaminated soils have emerged, such as S/S technology, displacement technology, soil leaching, incineration, solvent extraction, glass curing, and physical separation, emerged. Among them, solidification/stabilization (S/S) technology is the most widely used because of its cost-effective and simple operation [14,15].

The S/S technology of soil usually provides the ability to handle HMs through two aspects. On the one hand, the S/S technology has a direct effect on HMs. Chemical precipitation, physical encapsulation, adsorption, and other means occur between HMs and hydrations products of binders; on the other hand, the S/S technology directly affects soil, and indirectly affects HMs by changing the soil structure. The reduced permeability leads to reduced migration of HMs, then the stability of HMs in the soil can be achieved [15,16]. However, while enjoying the restorative power of S/S technology, one must also consider its environmental impact.

Considering this problem, three inorganic binders, cement, lime, and fly ash, were used in the current study to improve S/S efficiency while reducing carbon emissions and easing the burden of industrial waste disposal [17–19]. However, it should be noted that the use of binders should involve reasonable control of the amount: too little S/S has poor effect, but if the amount is too much it will not only increase the cost, but also change the physical and chemical properties of the soil, and even cause secondary pollution.

Starting from the mechanism of the S/S technology, it can be realized that this technology cannot reduce the concentration of HMs in the soil, but restricts the migration of pollution, or limits the effectiveness of pollutants. Based on this, it is necessary to track the follow-up progress of HMs after the use of S/S technology. In the internal system of S/S HM-contaminated soil, the type of soil [20], the type and content of HMs [21], the type and content of binders [22,23], the curing conditions [23], and the moisture content [24] all have an impact on the long-term stability of HMs. In various complex environments, such as carbonation [25], acid rain leaching [25–27], high salt groundwater infiltration [28,29], wetting and drying cycles [30–32], and F–T cycles [33–36], the stable forms of the contaminants in the S/S-contaminated soil is very likely to change or even fail, which causes the activation of HM pollutants in the soil, causing secondary pollution and affecting its engineering mechanical properties. Therefore, the environmental durability of S/S-contaminated soil is extremely sensitive to environmental changes. The impact of F–T cycles on S/S HM-contaminated soil will continue to be focused on in-depth in this study.

Freeze–thaw cycles mainly occur in seasonal frozen regions. The moisture in the soil constantly transforms between liquid and solid with the periodic change of temperature: through changes in the volume of water in different fractions, as well as the free migration of water, the pore structure and density of the soil are changed, which is one of the direct factors affecting the migration effect of HMs. In China, the area of seasonal permafrost is about 5.14 million square kilometers, accounting for 53 percent of the total land area [37]. According to the second national soil erosion remote sensing survey, China's F–T erosion area has reached 13.4% of the country's total area [38]. Because of the vast F–T area, it is of great practical significance to explore the influence of the F–T cycle on the S/S of HM-contaminated soil. After 12 F–T cycles, the leaching concentrations of Pb/Zn-contaminated soil and composite Zn–Pb-contaminated soil increased greatly [34]. The elastic modulus of silty clay and modified clay can be significantly reduced after four F–T cycles [39]. After conducting seven F–T cycles on silty clay, Wang et al. concluded that the number of F–T cycles had a great influence on the mechanical properties of soil [40]. Studies have confirmed that under the long-term effect of simple F–T cycles (180 cycles, 180 days), the unconfined compressive strength loss rate of cemented contaminated soil can reach more than 30%, and the concentration of HM ions in HM leaching solution can increase by more than 20% [18,41,42].

This research has been improved on this basis, and "long-term" is the keyword of this. Studying the condition of HMs in the soil during the long F–T cycle period, observing the S/S effect of the HMs is a good way to ensure the long-term use of the S/S soil. Effective control of HMs in soil under adverse conditions is of great significance to prevent secondary pollution of HMs. A maximum of 90 F–T cycles (90 days) was set up under the same F–T mode to explore the stability of HMs under long-term F–T cycles in this research.

After making up for the problem of short-term F–T, the situation of HMs in the soil has also been improved, and the transformation from single HM pollution to compound HM pollution research has been realized. According to a large number of studies, one source of pollution often produces multiple types of HM pollution [41–43]. As, Cd, Cr, Cu, Mn, Ni, Pb, Zn, and other HMs exist in the farmland soil of the Qixia mining area in Nanjing, China [44]. There are many HMs in the weathered coal gangue, and the surrounding land is also harmed by HMs such as Zn, Cd, and Cr. Research on a single HM-contaminated soil can no longer meet the actual needs. Therefore, in this study, three pollutants, Pb, Zn, and Cd, were added to the soil at the same time.

The adsorption–desorption, precipitation reaction, complexation reaction, and oxidation–reduction reaction between HMs and soil allow HMs to exist in different forms in soil, and different forms of HMs exhibit different toxicity and environmental behavior [45]. When HMs are in a less bioavailable form or a more stable form, their risk in the environment is low. Therefore, the content of each form of HMs can be used as an observation indicator to assess the risk of HMs in soil. The improved Tessier method was used to extract seven fractions of HMs in the soil in this study.

Based on the above analysis, the improved Tessier method was adopted to detect the content of various forms of HMs (Pb, Zn, and Cd) in the soil that had undergone six F–T cycle conditions (0, 3, 7, 14, 30, and 90 cycles) up to 90 days, and the functional groups were analyzed by Fourier transform infrared spectroscopy analysis tests. Meanwhile, the study assumes that the HMs are uniformly distributed in the soil, by controlling the particles of the original soil less than 1 mm, the mixing time of the preparation of contaminated soil longer than 5 min, and the error of X-ray fluorescence analyses (XRF) of the same batch of three concentrations less than 3%.

In this study, the safety of the S/S technology is investigated by using a near-actual high concentration of complex hinged HM-contaminated soil, the morphological changes of HMs as a variable of interest, and the F–T cycle effects that may occur in most of the global land as the influencing factor. The conclusions and laws drawn from this study provide more rigorous theoretical support for predicting the safety of seasonally S/S HM-contaminated soil use and provide favorable conditions for post-remediation reuse of contaminated soil [18].

## 2. Materials and Methods

### *2.1. Material*

### 2.1.1. Soil

The soil was collected from a site in Gaomiao Village, Chongqing, with dense soil, small porosity, brownish-red soil color, and large water content, but the soil was still in a plastic state. After bringing the soils back to the laboratory, they were placed into an electric constant temperature air blast drying box to dry and left at 100 °C for 24 h before all steps. Then, they were crushed and passed through a 1 mm nylon sieve after removing stones, tree roots, and other impurities.

Table 1 shows the basic physical properties of soil taken from the limit moisture content test, and the compaction test, which were carried out according to the Standards for Geotechnical Test Methods (GB/T 50123-2019). The soil was sieved to obtain a coarse-grained group containing more than 25% and not more than 50% and satisfying $w_L < 50\%$, $I_P \geq 7$, and $I_P \geq 0.73(w_L - 20)$. According to the engineering classification standard of soil (GB/T 50145-2007), the soil is low-liquid-limit clay. The sealed soil was assessed using the XRF to identify the chemical composition and relative content of each composition. The results are shown in Figure 1.

**Table 1.** Basic physical properties of undisturbed soil samples.

| Physical Property Index | Soil Sample |
|---|---|
| Liquid Limit/% | 27 |
| Plastic Limit/% | 12 |
| Plasticity Index ($I_P$) | 15 |
| Optimum Moisture Content/% | 11.8 |
| Maximum dry density/g/cm$^3$ | 1.91 |

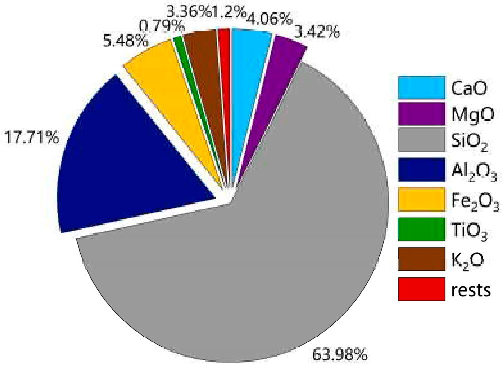

**Figure 1.** Main chemical components of undisturbed soil.

### 2.1.2. Binders

Cement, lime, and fly ash were used simultaneously in this study for the following three reasons. (1) Cement costs a lot of energy and releases a lot of carbon according to previous studies [45,46]. Therefore, the use of cement should be reduced; (2) the active substances in fly ash and lime react with the hydration products of cement to further improve properties of the soil and enhance the S/S effects of the HMs; (3) fly ash, as a kind of industrial byproduct, used in this way can reduce the pressure of waste treatment.

Figure 2 shows the results of the X-ray fluorescence analysis of cement, lime, and fly ash, containing the chemical composition and content of each component of three binders. Analytical-grade calcium oxide is the main component of quicklime, which was tested as high as 88.73 percent; the model of the ordinary Portland cement was 325; the fly ash was taken from the Chongqing power plant, and the grade of it was determined as two, according to GB/T 1594-2017. To ensure the uniform mixing of binders and soil, the binders needed to pass a 200-mesh sieve before use.

### 2.1.3. Heavy Metals

To minimize the influence of anions of the added HM compounds on the test results, analytical-grade $Zn(NO_3)_2 \cdot 6H_2O$, analytical-grade $Pb(NO_3)_2$, and high-purity $Cd(NO_3)_2 \cdot 4H_2O$ were used simultaneously as HM contaminants to provide the required HM ions. Reactions are difficult to take place between binders, hydration products, and nitrate, while the concentration of nitrate was not high in this research. The side effects of $Zn(NO_3)_2 \cdot 6H_2O$, $Pb(NO_3)_2$, and $Cd(NO_3)_2 \cdot 4H_2O$ were, thus, negligible [47,48].

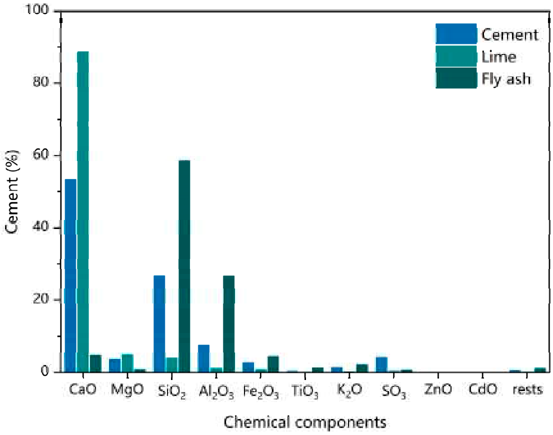

**Figure 2.** The chemical components of three binders.

## *2.2. Specimen Preparation*

### 2.2.1. Preparation of Artificial Composite Contaminated Soil

In order to improve the observability of ion changes with F–T cycles in this study, as well as to make the test soils more closely resemble the form of contamination in the project, the tertiary standard limits of Pb, Zn, and Cd in the Soil Environmental Quality Standard (GB36000-2018) were enlarged by 16, 10, and 400 times, respectively, to obtain test yields of 8000 mg/kg, 5000 mg/kg, and 400 mg/kg for Pb, Zn and Cd, respectively.

At the same time, the soil moisture content was set at 120% of the optimal moisture content to ensure adequate F–T effects, and then, according to the soil water content and the HM mixture, a certain amount of deionized water, analytical-grade $Pb(NO_3)_2$, analytical-grade $Zn(NO_3)_2{\cdot}6H_2O$, and high-purity $Cd(NO_3)_2{\cdot}4H_2O$ was weighed and placed in a magnetic mixer for ten minutes to mix the solution well.

After that, the mixed solution was added to the sieved soil, stirred with a magnetic mixer for 10 min, then wrapped in a plastic bag and placed in a humidor with a temperature of 22 °C and a relative humidity of 95% for 30 days to make an artificial composite HMs-contaminated soil.

### 2.2.2. Stabilization/Solidification of Contaminated Soil

According to the previous results of our research group [41], the better designed mixing ratio of cement, lime, and fly ash on S/S of HMs-contaminated soil is 5%, 2.5%, and 2.5%, respectively, so this ratio was adopted in our current study. After weighing a certain amount of binder according to the binders' set ratio, the soil-added binders were stirred by a mechanical mixer for 10 min, then sealed by a plastic membrane and kept for 56 days in a standard curing chamber (22 °C, 95% relative humidity) for use.

## *2.3. Testing Methods*

### 2.3.1. Freeze–Thaw Test

The alternately high- and low-temperature test chamber (Chongqing Tester Experimental Instrument Co., Ltd. Chongqing, China) is the instrument for F–T tests. Five kinds of F–T cycles were designed for the specimens, including 3, 7, 14, 30, and 90 F–T cycles (0 F–T cycle was set as the control group). The setting mode of one cycle is shown in Table 2 (24 h for each cycle), in which the freezing temperature of the soil was set at −10 °C, and the dissolution temperature was 20 °C. To ensure the complete freezing and dissolution of the soil, it was maintained for 11 h after reaching the specified temperature. The F–T cycled specimens were ground and pounded through a 200-mesh sieve to meet the experimental.

**Table 2.** The form of the F–T cycles.

| **Temperature Form** | From 20° to − 10° | Remaining −10° | From − 10° to 20° | Remaining 20° |
|---|---|---|---|---|
| **Time/h** | 0–1 | 2–12 | 12–13 | 14–24 |

Note: The first time the soil freezes, it starts to drop from room temperature.

### 2.3.2. The Improved Tessier Method

According to the Geological Survey Standards of China Geological Bureau (DD2005-03), the improved Tessier method was adopted to determine the distribution of seven fractions of three HMs of S/S Pb–Zn–Cd HM-contaminated soil under six conditions. This method is to further divide the organically bound fractions in the Tessier sequential extraction method proposed by Tessier into strongly organically bound fractions and humic-acid-bound fractions, and additionally add the water-soluble fraction [49,50]. The seven forms in the method are water-soluble fraction, ion exchange fraction, carbonate-bound fraction, iron and manganese oxidation fraction, weak organic fraction, strong organic fraction, and residue fraction.

The main reagents used are as follows, according to Technical Standards for Geological Survey of China Geological Survey (DD2005-03).

(a) Hydrochloric acid ($\rho(HCl) = 1.18$ g/mL);
(b) Hydrochloric acid in which concentrated hydrochloric acid and water are mixed in a volume ratio of 1:1;
(c) Nitric acid ($\rho(HNO_3) = 1.41$ g/mL);
(d) Nitric acid ($c(HNO_3) = 0.02$ mol/L);
(e) Perchlorate ($\rho(HClO_4) = 1.66$ g/mL);
(f) Hydrofluoric acid ($\rho(HF) = 1.15$ g/mL);
(g) Magnesium chloride ($c(MgCl_2{\cdot}6H_2O) = 1.0$ mol/L, pH = 7.0 ± 0.2)

Five hundred and eight grams $MgCl_2 \cdot 6H_2O$ was weighed and dissolved in distilled water in a 2500 mL plastic bucket. The pH was adjusted by NaOH ($\omega(NaOH) = 10\%$).

(h) Sodium acetate ($c(CH_3COONa{\cdot}3H_2O) = 1.0$ mol/L, pH = 5 ± 0.2)

Three hundred and forty grams $CH_3COONa \cdot 3H_2O$ was weighed and dissolved in distilled water in a 2500 mL plastic bucket. The pH was adjusted by $CH_3COOH$.

(i) Sodium pyrophosphate ($c(Na_4PO_7{\cdot}10H_2O) = 0.1$ mol/L, pH = 10.0 ± 0.2)

One hundred and eleven and a half grams Na4PO$_7\cdot$ 10H$_2$O was weighed and dissolved in distilled water in a 2500 mL plastic bucket, and the pH was adjusted to 10.0 ± 0.2 with $HNO_3$ where concentrated nitric acid and water are mixed in a volume ratio of 1:1.

(j) Ammonium hydroxide hydrochloride–hydrochloric acid mixture ($c(HONH_3Cl) = 0.25$ mol/L, $c(HCl) = 0.25$ mol/L)

Forty-three point four grams $HONH_3Cl$ was weighed and 104 mL hydrochloric acid was added, where concentrated hydrochloric acid and water are mixed in a volume ratio of 1:1 and dissolved in distilled water in a 2500 mL plastic bucket.

(k) Hydrogen peroxide ($\varphi(H_2O_2) = 30\%$, pH = 2.0 ± 0.2)

The pH was adjusted by nitric acid where concentrated nitric acid and water are mixed in a volume ratio of 1:1.

(l) Ammonium acetate–nitric acid mixture ($c(CH_3COONH_4) = 3.2$ mol/L, $c(HNO_3) = 4.48$ mol/L)

Six hundred and sixteen point six grams $CH_3COONH_4$ was weighed and added 500 mL $HNO_3$ (c). Both were dissolved in a 2500 mL plastic bucket with distilled water.

Using the above reagent, the concentration of HMs in soil under seven forms could be accurately determined according to the following nine steps.

(1) A sample of 2.5000 g was accurately weighed and placed in a centrifuge tube.
(2) Extraction of water-soluble fraction.

Distilled water was used as the extraction agent for water-soluble HMs. First, 25 mL of distilled water was added to the beaker and shaken well, then the beaker was placed into the ultrasonic cleaner. Ultrasound was performed at the working mode of 5 min with 5 min intervals at a frequency of 40 kHz, and the total working time was 30 min, during which the water temperature in the ultrasonic cleaner was 25 ± 5 °C. Then, the material in the beaker was transferred into a centrifuge tube for centrifugation (20 min at a speed of 4000 r/min), the precipitated supernatant was filtered with a pore diameter of 0.45 μm, and then the liquid was poured into a 25 mL colorimetric tube. An Optima 8000 inductively coupled plasma emission spectrometer was used to detect the contents of lead, zinc, and cadmium in the extracted liquid.

(3) Residue cleaning

The remaining residue was added to about 100 mL distilled water to wash the precipitation, and centrifuged at 4000 r/min for 10 min. The aqueous phase was discarded, and the residue was left.

(4) Extraction of ion-exchange fraction

Twenty-five milliliters of magnesium chloride (g) solution were accurately added to the residue left in step (3), shaken well, and placed in an ultrasonic cleaner that had been placed into water. Ultrasound was performed at a frequency of 40 kHz for 30 min (ultrasonic was performed for 5 min every 5 min during this period, and the water temperature in the ultrasonic cleaner was controlled at 25 ± 5 °C). After the ultrasound, they were taken out, and centrifuged at 4000 r/min for 20 min. A total of 5 mL of liquid was taken into a 10 mL colorimetric tube and added to 0.5 mL of hydrochloric acid (a). After that, the distilled water was used for constant volume to scale. After shaking the colorimetric tube well, the ICP-OES theory was used to determine the content of HMs in liquid. The step of residue cleaning was repeated at last.

(5) Extraction of carbonate-bound fraction

Sodium acetate (h) was selected as the extraction agent of carbonate-bound fraction. A total of 25 mL of it was added to the residue which came from step (4), shaken well, and placed in an ultrasonic cleaner with a frequency of 40 kHz for 1 h (ultrasonic was performed for 5 min every 5 min during the period, and the water temperature in the ultrasonic cleaner was controlled at 25 ± 5 °C). Then they were taken out and centrifuged at 4000 r/min for 20 min. Separated 5 mL liquid was poured into a 10 mL colorimetric tube. After adding 0.5 mL HCl (a) to the colorimetric tube, the distilled water was brought to scale, and shaken well. An Optima 8000 inductively coupled plasma emission spectrometer was used to analyze the contents of lead, zinc, and cadmium, and step (3) was repeated finally.

(6) Extraction of humic-acid-bound fraction

Fifty milliliters sodium pyrophosphate solution (i) was accurately added to the residue obtained in step (5). After shaking well, it was taken to the ultrasonic cleaner with a frequency of 40 kHz for 40 min (ultrasonic 5 min every 5 min during this period, and the water temperature in an ultrasonic cleaner is controlled at 25 ± 5 °C) and placed for 2 h. Then, the solution was centrifuged at 4000 r/min for 20 min. A 50 mL beaker was filled with 10 mL clear liquid and 5 mL $HNO_3$ (c) and 1.5 mL $HClO_4$ were added (e). The surface dish was used to cover the beaker, and the beaker was heated and steamed on the electric heating plate until the occurrence of $HClO_4$ white smoke exhaust. Then, 1 mL HCl (b) was added, the surface dish was washed, and the dissolved salt was heated, removed, and cooled. Finally, a 10 mL colorimetric tube was scaled by distilled water. After shaking well, an Optima 8000 inductively coupled plasma emission spectrometer was used to analyze the contents of lead, zinc, and cadmium. The remaining residue was treated as described in step (3).

(7) Extraction of iron and manganese oxidized bond fraction

Fifty milliliters hydroxylamine hydrochloride solution (j) was added to residue obtained from step (6) accurately. After they were shaken well, the ultrasound was carried out in ultrasonic cleaner with a frequency of 40 kHz for 1 h (ultrasonic for 5 min every 5 min during this period, water temperature in an ultrasonic cleaner is controlled at 25 ± 5 °C). Then, the solution was removed and centrifuged at 4000 r/min for 20 min. Finally, 10 mL clear liquid was separated into a colorimetric tube. The contents of lead, zinc, and cadmium were analyzed by the ICP-OES method. The remaining precipitation was transferred to a 50 mL centrifuge tube with 50 mL distilled water and centrifuged for 10 min at a speed of 4000 r/min. The aqueous phase was discarded, and the residue was left after cleaning twice.

(8) Extraction of strong organic bonding fraction

Three milliliters $HNO_3$ (d) and 5 mL $H_2O_2$ (k) were accurately added to the residue obtained from step (7). The solution was shaken well and kept for 1.5 h in a constant temperature water bath at 83 ± 3 °C (stirred once every 10 min during the period). Then, the solution was continued to have 3 mL $H_2O_2$ added (k) and kept warm in the water bath for 1 h and 10 min (stirring once every 10 min during this period). After cooling to room temperature, 2.5 mL ammonium acetate–nitric acid solution (a) was added, and the samples were diluted to about 25 mL and stirred for 1 min, then placed at 25 ± 5 °C overnight, and centrifuged at 4000 r/min for 20 min. The clear liquid was poured into a 50 mL colorimetric tube, diluted with distilled water to scale, and shaken well. Then, a 50 mL beaker was used. First, 25 mL separated clear liquid, 10 mL $HNO_3$ (c), and 1 mL $HClO_4$ (e) was poured in, then, with a surface dish, it was heated on the electric heating plate at low temperature until it was nearly dry, and at high temperature until the concentrated white smoke was cleared. After this, 5 mL HCl (b) was added while hot, and the dish was washed. The beaker was heated at a low temperature until the salts dissolved. After the solution cooled, 25 mL of water was placed into a colorimetric tube and shaken well. A 5 mL solution was separated into 10 mL colorimetric tubes for ICP-OES analysis for Pb, Zn, and Cd. About 20 mL of distilled water was added to wash the sediment, and centrifuged for 10 min at a speed of 4000 r/min. The aqueous phase was discarded. The cleaning process was carried out twice, leaving the residue at the end.

(9) Extraction of residue fraction

The cleaned residue obtained from step (8) was air-dried, ground, weighed, and the correction factor was calculated, and then the sample of 0.2000 g was accurately taken out and placed in the PTFE crucible. The sample was wetted in the crucible by water and 5 mL of hydrochloric acid (f), nitric acid, and perchloric acid mixture in the ratio of 1:1:1 was added. The crucible was heated on an electric heating plate until the white smoke of perchloric acid was fully distributed. Then, 3 mL of hydrochloric acid (b) was added to the crucible. After the crucible wall was washed, the crucible continued to heat until the salt was dissolved, and then cooled to room temperature. Finally, the remaining product was transferred to a colorimetric tube, and the volume was kept at 25 mL and shaken well. The contents of lead, zinc, and cadmium were analyzed by the ICP-OES method.

### 2.3.3. Fourier Transform Infrared Spectrum (FTIR) Analysis Test

The attenuated total reflection Fourier transform infrared spectroscopy method was adopted in this study. Six kinds of soil were dried at 100 °C for 24 h and tested by a Fourier infrared spectrometer after passing through a 200-mesh sieve. The mid-infrared region was used for detection in this study. The following procedures were used to analyze the spectrum [51].

The measured mid-infrared was tentatively divided into a characteristic functional group area (4000–1333 $cm^{-1}$) and a fingerprint area (1333–400 $cm^{-1}$), then the characteristic functional group was further divided into three wavebands (4000–2400 $cm^{-1}$, 2400–2000 $cm^{-1}$, and 900–400 $cm^{-1}$), and the fingerprint area was finely divided into two wavebands (1333–900 $cm^{-1}$ and 900–400 $cm^{-1}$). Infrared spectroscopies were taken as a preliminary analysis (compound type, functional group, the structural unit, etc.) based on the corresponding characteristic absorption bands to determine the possible functional groups and possible structural units.

Based on possible functional groups, possible structural units, the characteristic frequency table of the characteristic absorption bands of various compounds, and various factors affecting the movement of characteristic frequencies, the structural details were revealed. The standard spectra of related compounds determined according to the details were compared with the obtained spectra of soils under six environments to obtain specific functional group composition.

## 3. Results

### 3.1. Effect of Solidification/Stabilization on the Speciation of Different Heavy Metals

Among the seven different HM fractions extracted by the improved Tessier method, the order of bioavailability for different fractions of HMs in the soil is shown as follows: water-soluble state > ion-exchange state > carbonate-bound fraction > humic-acid-bound fraction > iron and manganese oxidized bond fraction > strong organic bonding fraction > residue fraction. $Pb^{2+}$, $Zn^{2+}$, and $Cd^{2+}$ provided by $Pb(NO_3)_2$, $Zn(NO_3)_2 \cdot 6H_2O$, and $Cd(NO_3)_2 \cdot 4H_2O$ are in the ion exchange fraction. HMs whose bioavailability is greater than this form can be considered to have undergone a transition to the stable forms, and are referred to as the stable form, while the ion-exchange fraction and the water-soluble fraction are set as the unstable form.

Figure 3 shows the relative content of HMs in the S/S soil under a non-freeze–thaw condition in the unstable fraction, and the stable fraction. It is obvious that the content of Pb ion, Zn ion, and Cd ion supplied in the soil decreased sharped after the S/S by adding cement, lime, and fly ash. After S/S, the unstable forms of Pb, Zn, and Cd remain as only 1.19%, 1.09%, and 24.89%, respectively.

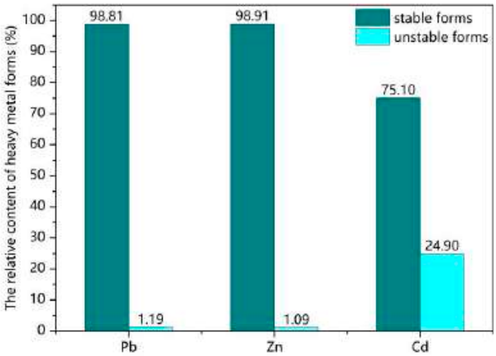

**Figure 3.** The relative content of heavy metals (HMs) in the solidified/stabilized (S/S) Pb–Zn–Cd composite HM-contaminated soil without F–T cycles.

However, Figure 3 also shows that the S/S efficiency varies for different HMs. The relative contents of the stable forms of Pb and Zn are much larger than that of the stable fractions of Cd. After the S/S process, 98.81% of lead and 98.91% of zinc were converted to a stable fraction, but only 75.10% of cadmium was converted to a stable fraction, with a relative content difference of more than 20%.

### 3.2. Effect of F–T Cycles on the Speciation of HMs

Figure 4 reveals the trend of the relative content of the two types of fractions of HMs in the S/S Pb–Zn–Cd composite HM-contaminated soil with the action of F–T cycles. The changing trend of the curve in it indicates that the F–T cycle causes HMs to transform from stable to unstable forms, but the reduction of stable HM becomes slow after reaching 14 cycles. After 90 F–T cycles, the relative contents of stable forms of Pb, Zn, and Cd in the soil decreased by 1.27%, 3.11%, and 8.16%, respectively, while the decrease reached more than 50% of the total decrease after 14 F–T cycles.

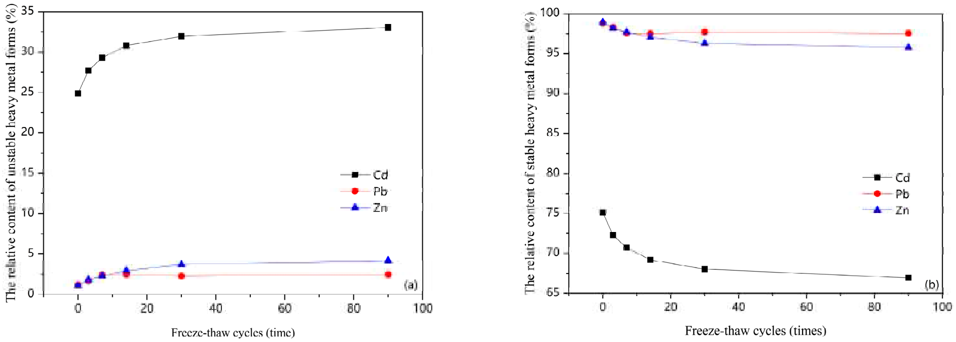

**Figure 4.** The variation of the relative content of HM forms with F–T cycles in the S/S Pb-Zn-Cd composite HM-contaminated soil. (**a**) unstable HM forms; (**b**) stable HM forms.

The variation of the relative content of stable fractions of three HMs in S/S soil with the number of F–T cycles is shown in Figure 5. It can be seen that the relative content of the carbonate-bound fraction of HMs decreases significantly with F–T cycles. The effect is significant within the 14 F–T cycles, the slope of the curve is large, and the rate of decline is fast. However, with the increase of the F–T cycles times, the rate of decline of carbonate-bound forms becomes relatively slow. After 14 F–T cycles, the relative contents of carbonate-bound fraction of Pb, Zn, and Cd decreased by 13.46%, 7.35%, and 8.68%, respectively, while the relative contents of corresponding types only decreased by 2.06% in the process from 14 F–T cycles to 90 F–T cycles, 4.58%, and 1.56%.

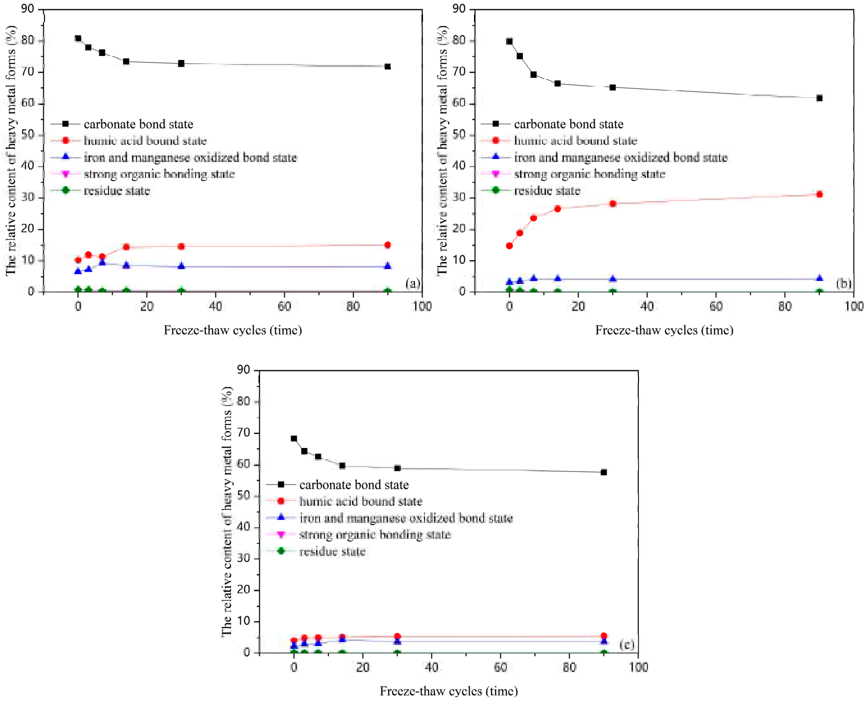

**Figure 5.** The variation of relative content of each speciation of HMs with F–T cycles in the S/S Pb–Zn–Cd composite HM-contaminated soil. (**a**) Zn; (**b**) Pb; (**c**) Cd.

### 3.3. Effect of F–T Cycles on the Functional Groups in S/S Soil

Figure 6 shows the FTIR spectra of S/S Pb–Zn–Cd composite HM-contaminated soil under six F–T cycle conditions (0, 3, 7, 14, 30, and 90 cycles). According to their own spectra, a large amount of literature data, and standard Fourier infrared spectrogram, the types of functional groups in each condition were distinguished.

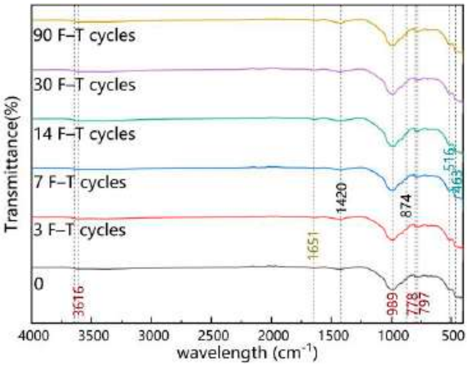

**Figure 6.** FTIR spectra of S/S Pb–Zn–Cd composite HMs-contaminated soil under 6 F–T cycle conditions (0, 3, 7, 14, 30, and 90 cycles).

The locations of the characteristic peaks of the FTIR spectra under the six F–T conditions are roughly the same, indicating that within 90 F–T cycles, the types of target substances (soil components, binder components, hydration products, etc.) detected in the S/S Pb–Zn–Cd composite HMs-contaminated soil did not change.

Seven hundred and ninety-seven per centimeter, and Seven hundred and eighty-seven per centimeter are caused by Si–O–Si stretching vibrations, which are typical double peaks of quartz minerals, which is an important part of the soil itself, and the added binders. The peaks at 516 cm$^{-1}$ and 463 cm$^{-1}$ are the Si–O vibration absorption peaks of the gel [52,53]. There are two main reasons for the existence of the characteristic peak of colloid. One is that the effective component of cement, tricalcium silicate, and dicalcium silicate, generates a large amount of hydrated calcium silicate colloid after hydration; the other is that the hydration product of cement, calcium hydroxide, continues to react with lime and fly ash to form colloids [54]; among them, there was residual calcium hydroxide, and the characteristic peak appears in 1651 cm$^{-1}$. The existence of colloids has made a great contribution to the S/S of HMs, such as the large amounts of adsorption of HM ions, and the filling of soil pores, which hinders the flow of HMs. The formation of calcium hydroxide also underwent a substitution reaction with HM ions, causing HM ions to precipitate.

Eight hundred and seventy-four per centimeter and one thousand four hundred and twenty per centimeter are caused by carbonate stretching vibration. These two obvious characteristic peaks appeared in the FTIR spectra under every F–T condition (0, 3, 7,14, 30, and 90 F–T cycles). This is mainly produced by the entry of carbon dioxide into the atmosphere and is affected by the pH of the soil. There is a huge relationship with the formation of HM carbonate-bound fraction.

## 4. Discussion

### 4.1. Effect of Solidification/Stabilization on the Speciation of Different Heavy Metals

The results in Section 3.1 show the transfer of HMs to stable forms after the addition of binders. After the hydration reaction of the binders, their hydration products will interact with HMs, increasing the inertness of HMs and reducing the migration ability of HMs.

The first mechanism for immobilization of HMs is a chemical reaction, in which lead, zinc, and cadmium react with $Ca(OH)_2$, calcium silicate hydrates, and so on, and are fixed to the binder components. Furthermore, the S/S technology also has a certain physical effect on the treatment process of HMs through the improvement of soil properties and the progress of the chemical reaction of the binders [55]. The decrease in soil permeability will hinder the migration of HMs, and the colloids produced by the curing agent will physically encapsulate the HMs [56]. Soil S/S technology, as a risk management technology, has a strong effect on reducing the risk of HMs. However, it can be clearly found that for different HMs in the soil, the conversion efficiency is different, with cadmium having the lowest conversion efficiency, with a difference of 20% compared to the other two HMs. The factors causing this phenomenon may have the following three aspects.

First, the properties of each HM are different [55]. Compared with cadmium ions, lead ions are more electronegative and have poor reaction activity [57]. Second, the S/S of HMs is closely related to the pH value of the soil, and different kinds of HM have different optimal pH values for S/S [58–60]. Most lead ions precipitate at a pH of about 9.8 and remain stable within a pH of 12 [61]. Zinc hydroxide begins to precipitate when pH is above 5 [62], and crystalline $Cd(OH)_2$ is precipitated in soil when pH is increased to above 6.2 [63]. Finally, the initial content of the three elements added to the undisturbed soil is different, the added cadmium is the least, and the progress of S/S will be less targeted.

### 4.2. Effect of F–T Cycles on the Speciation of HMs

The main reasons for this phenomenon are as follows. Through the continuous action of the F–T cycle, the porosity ratio in the soil keeps increasing, making it easier for carbon dioxide to enter the soil. Some studies have shown that the carbonization process of soil has adverse effects on the S/S of HMs. The pH value of the soil keeps decreasing with the carbonization, causing hydrolysis of the hydration products of many adhesives, and further activation of more HMs.

This is due to the fact that the carbonate-bound fraction of HMs is very sensitive to the change of pH. Under alkaline conditions, the carbonate-bound fraction is relatively stable. With the continuous decrease of soil pH under the action of the F–T cycle, the HM compounds in the carbonate-bound fraction decompose, while the rate of decomposition is associated with the change speed of pH because the degree of influence of carbon dioxide on soil Ph gradually decreases over time. During this time, the process of S/S of HM is still underway but does not play a dominant role.

As the F–T cycle progresses, the relative content of the humic-acid-bound fraction, iron and manganese oxidized bond fraction, strong organic bonding fraction, and residue fraction in the stable form increases continuously. However, due to their small content, they have little influence on the overall fraction of HMs, so the relative content of the stable form of HMs is still in a downward trend as the F–T cycle progresses. It may also be noted that these four HM forms are not sensitive to pH.

### 4.3. Effect of F–T Cycles on the Functional Groups in S/S Soil

According to Figure 6, a large number of Si–O–Si stretching vibrations, Si–O vibration absorption peaks, and carbonate stretching vibration can be found in the sample; this proves that substances that can enhance the stability of HMs, such as colloids and carbonate binders, are indeed present in the soil at this time [52,53]. This is why a large number of HMs have previously undergone a transition to the steady fractions.

Meanwhile, the types of functional groups contained in the soil are approximately the same in the six cases. The direct effect of the F–T cycle on the soil is mainly a physical reaction without the addition of new substances; therefore, the number of characteristic peaks did not increase. Meanwhile, the result of chemical speciation analysis shows that when the number of F–T cycles exceeded 14 times, the changing trend of the content of each HM forms was very slow, and gradually stabilized instead of a single decline. Therefore, there was no disappearance of the characteristic peak. Due to the above reasons, the F–T cycle did not change the types of functional groups in the system.

In addition, carbonate stretching vibration was detected in the soil. This is consistent with the fact that there are carbonate binders in the soil, and that when the pH environment in which the HMs are located changes, the HMs react with the carbonates to varying degrees. The F–T cycles, on the other hand, increase the amount of carbon dioxide entering the soil precisely by changing the porosity of the soil, causing changes in the carbonate-bound fraction of the soil.

Throughout the whole process of this study, it is clearly recognized that the change in the content of its stable fractions tends to slow down when the F–T cycles are performed several times. According to the experimental results, this node occurs at 30 cycles. When conducting an HM soil remediation project, the collected soil samples can be S/S in the laboratory and then subjected to a small trial test of 30 F–T cycles to test the morphological components, derive the instability limits, determine whether there is a safety hazard, and determine whether to keep the curing ratios or change the curing ratios.

## 5. Conclusions

The improved Tessier method and Fourier transform infrared spectrum (FTIR) analysis test were used to study the effects of long-term F–T on the S/S of Pb–Zn–Cd composite HM-contaminated soil in this study. The soil morphology and FTIR spectra were tested in six environments (without F–T cycles, with 3 cycles, 7 cycles, 14 cycles, 30 cycles, and 90 cycles) in HM-contaminated soil, and the following remarkable conclusions were obtained.

In the S/S Pb–Zn–Cd composite HM-contaminated soil, the addition of three binders, cement, lime, and fly ash, reduces the HM risk by making HMs exist in a more stable form. The characteristic peaks at 463 $\mathrm{cm}^{-1}$ and 516 $\mathrm{cm}^{-1}$ of the FTIR spectra indicate the presence of colloids that can adsorb and store HMs, and the characteristic peak of calcium hydroxide that can precipitate HMs appeared at 1651 $\mathrm{cm}^{-1}$. However, for different types of HMs, the S/S efficiency is different. The relative content of HMs transferred to stable forms in lead and zinc is 20% greater than that in cadmium.

The content of HMs in a steady state decreased continuously with the increase of frequency of F–T cycles. There were drastic changes before 14 cycles, but with the continuous increase in the frequency of F–T cycles, the increasing trend gradually decreases, and the rate of decrease in the stable form of HMs became minimal after 30 F–T cycles. This is the main reason why F–T cycles would not change the types of functional groups.

Under the action of long-term F–T cycles, the decrease in the stable form content of HMs in the S/S composite HM-contaminated soil is mainly caused by the decrease in the carbonate-bound state content. Its peaks appeared at 874 $\mathrm{cm}^{-1}$ and 1420 $\mathrm{cm}^{-1}$. Ninety F–T cycles caused the carbonate-bound content of Pb, Zn, and Cd to decrease by 18.04%, 8.92%, and 10.74%, respectively.

Through this experiment, it can be seen that after the number of F–T cycles reaches 30, the decrease rate of stable form HM content reaches the minimum; therefore, 30 F–T cycles can be used as the critical test point for indoor tests in actual projects to determine the danger zone. However, for different soils, exactly how the critical number changes is not yet known; in future research, it is recommended that the majority of scholars conduct further research on this part. At the same time, the huge change in the content of the carbonate-bound fraction of HMs during the F–T cycles must also recognize the tremendous influence of environmental pH on the S/S effect, and numerous studies have been conducted by domestic and foreign scholars on this content in the hope that a risk control method for the common assessment of various influencing factors can be established in the future.

**Author Contributions:** Conceptualization, Z.Y.; methodology, Z.Y. and Y.W.; investigation, Y.W., X.L., J.C. and K.Z.; writing—original draft preparation, J.C.; writing—review and editing, Z.Y.; supervision, Z.Y., X.L. and K.Z. All authors have read and agreed to the published version of the manuscript.

**Funding:** This research was funded by the National Natural Science Foundation of China, grant number 42177125 and the National Natural Science Foundation of China, grant number 41772306.

**Institutional Review Board Statement:** Not applicable.

**Informed Consent Statement:** Not applicable.

**Data Availability Statement:** Not applicable.

**Acknowledgments:** The authors acknowledge the financial support received from the National Natural Science Foundation of China (Grant No. 42177125, and No. 41772306). We also thank Ren Shupei and Wang Yao, graduate students, for their efforts in terms of conducting the laboratory tests.

**Conflicts of Interest:** The authors declare no conflict of interest. The funders had no role in the design of the study; in the collection, analyses, or interpretation of data; in the writing of the manuscript, or in the decision to publish the results.

## References

1. Xue, Q.; Zhan, L.T.; Hu, L.M.; Du, Y.J. Environmental geotechnics: State-of-the-art of theory, testing and application to practice. *China Civil. Eng. J.* **2020**, *53*, 80–94.
2. Liu, S.Y. Geotechnical investigation and remediation for industrial contaminated sites. *Chin. J. Geotech. Eng.* **2018**, *40*, 1–37.
3. Kogbara, R.B. A review of the mechanical and leaching performance of stabilized/solidified contaminated soils. *Environ. Rev.* **2014**, *22*, 66–86. [CrossRef]
4. Cao, X.; Ma, R.; Zhang, Q.S.; Wang, W.B.; Liao, Q.X.; Sun, S.C.; Zhang, P.X.; Liu, X.L. The factors influencing sludge incineration residue (SIR)-based magnesium potassium phosphate cement and the solidification/stabilization characteristics and mechanisms of heavy metals. *Chemosphere* **2020**, *261*, 127789. [CrossRef] [PubMed]
5. Hao, H.Z.; Chen, T.B.; Jin, M.G.; Lei, M.; Liu, C.W.; Zu, W.P.; Huang, L.M. Recent advance in solidification /stabilization technology for the remediation of heavy metalscontaminated soil. *Chin. J. Appl. Ecol.* **2011**, *22*, 816–824.
6. Zhang, T.T.; Li, J.S.; Wang, P.; Huang, Q.; Xue, Q. Experimental study of mechanical and microstructure properties of magnesium phosphate cement treated lead contaminated soils. *Rock Soil Mech.* **2016**, *37*, 279–286.
7. Ngo, H.T.T.; Watchalayann, P.; Nguyen, D.B.; Doan, H.N.; Liang, L. Environmental health risk assessment of heavy metal exposure among children living in an informal e-waste processing village in Viet Nam. *Sci. Total Environ.* **2021**, *763*, 142982. [CrossRef]
8. Ustaoğlu, F.; Islam, M.S. Potential toxic elements in sediment of some rivers at Giresun, Northeast Turkey: A preliminary assessment for ecotoxicological status and health risk. *Ecol. Indic.* **2020**, *113*, 106237. [CrossRef]
9. Islam, M.S.; Ahmed, M.K.; Al-Mamun, M.H.; Eaton, D.W. Human and ecological risks of metals in soils under different land-use types in an urban environment of Bangladesh. *Pedosphere* **2020**, *30*, 201–213. [CrossRef]
10. He, L.Z.; Zhong, H.; Liu, G.X.; Dai, Z.M.; Brookes, P.C.; Xu, J.M. Remediation of heavy metal contaminated soils by biochar: Mechanisms, potential risks and applications in China. *Environ. Pollut.* **2019**, *252*, 846–855. [CrossRef]
11. Markus, J.; McBratney, A.B. A review of the contamination of soil with lead. *Environ. Int.* **2001**, *27*, 399–411. [CrossRef]
12. Buddhi, W.; Liu, A.; He, B.B.; Yang, B.; Zhao, X.; Godwin, A. Ashantha G Behaviour of metals in an urban river and the pollution of estuarine environment. *Water Res.* **2019**, *196*, 414911.
13. Shao, Y.Y.; Yan, T.; Wang, K.; Huang, S.M.; Yuan, W.Z.; Qin, F.G.F. Soil heavy metal lead pollution and its stabilization remediation technology. *Energy Rep.* **2020**, *6*, 122–127. [CrossRef]
14. Liu, S.J.; Miao, C.; Yao, S.S.; Ding, H.; Zhang, K. Soil stabilization/solidification (S/S) agent-water-soluble thiourea formaldehyde (WTF) resin: Mechanism and performance with cadmium. *Environ. Pollut.* **2021**, *272*, 116025. [CrossRef]
15. Gong, Y.Y.; Zhao, D.Y.; Wang, Q.L. An overview of field-scale studies on remediation of soil contaminated with heavy metals and metalloids: Technical progress over the last decade. *Water Res.* **2018**, *147*, 440–460. [CrossRef]
16. Qin, C.C.; Yuan, X.Z.; Xiong, T.; Tan, Y.Z.; Wang, H. Physicochemical properties, metal availability and bacterial community structure in heavy metal-polluted soil remediated by montmorillonite-based amendments. *Chemosphere* **2020**, *261*, 128010. [CrossRef]
17. Gao, P.; Yue, S.J.; Chen, H.T. Carbon emission efficiency of China’s industry sectors: From the perspective of embodied carbon emissions. *J. Clean. Prod.* **2021**, *283*, 124655. [CrossRef]
18. Yang, Z.P.; Wang, Y.; Li, D.H.; Li, X.Y.; Liu, X.R. Influence of Freeze–Thaw Cycles and Binder Dosage on the Engineering Properties of Compound Solidified/Stabilized Lead-Contaminated Soils. *Int. J. Environ. Res. Public Health* **2020**, *17*, 1077. [CrossRef]
19. Wang, F.; Pan, H.; Xu, J. Evaluation of red mud based binder for the immobilization of copper, lead and zinc. *Environ. Pollut.* **2020**, *263*, 114416. [CrossRef]
20. Bai, B.; Rao, D.Y.; Chang, T.; Guo, Z.G. A nonlinear attachment-detachment model with adsorption hysteresis for suspension-colloidal transport in porous media. *J. Hydrol.* **2019**, *587*, 124080. [CrossRef]
21. Zha, F.S.; Zhu, F.H.; Xu, L.; Kang, B.; Yang, C.B.; Zhang, W.; Zhang, J.W.; Liu, Z.H. Laboratory study of strength, leaching, and electrical resistivity characteristics of heavy-metal contaminated soil. *Environ. Earth Sci.* **2021**, *80*, 184. [CrossRef]
22. Zha, F.S.; Qiao, B.R.; Kang, B.; Xu, L.; Chu, C.F.; Yang, C.B. Engineering properties of expansive soil stabilized by physically amended titanium gypsum. *Constr. Build. Mater.* **2021**, *303*, 124456. [CrossRef]
23. Wang, F.; Xu, J.; Yin, H.L.; Zhang, Y.H.; Pan, H.; Wang, L. Sustainable stabilization/solidification of the Pb, Zn, and Cd contaminated soil by red mud-derived binders. *Environ. Pollut.* **2021**, *284*, 117178. [CrossRef] [PubMed]

24. Bai, B.; Zhou, R.; Cai, G.Q.; Hu, W.; Yang, G.C. Coupled thermo-hydro-mechanical mechanism in view of the soil particle rearrangement of granular thermodynamics. *Comput. Geotech.* **2021**, *137*, 104272. [CrossRef]
25. Zha, F.S.; Liu, C.M.; Kang, B.; Xu, L.; Yang, C.B.; Chu, C.F.; Yu, C.; Zhang, W.; Zhang, J.W.; Liu, Z.H. Effect of Carbonation on the Leachability of Solidified/Stabilized Lead-Contaminated Expansive Soil. *Adv. Civil. Eng.* **2021**, *2021*, 8880818. [CrossRef]
26. Du, Y.J.; Jiang, N.J.; Shen, S.L.; Jin, F. Experimental investigation of influence of acid rain on leaching and hydraulic characteristics of cement-based solidified/stabilized lead contaminated clay. *J. Hazard. Mater.* **2012**, *225*, 195–201. [CrossRef]
27. Du, Y.J.; Wei, M.L.; Reddy, K.R.; Liu, Z.P.; Jin, F. Effect of acid rain pH on leaching behavior of cement stabilized lead-contaminated soil. *J. Hazard. Mater.* **2014**, *271*, 131–140. [CrossRef]
28. Stanforth, R.; Yap, C.F.; Nayar, R. Effects of weathering on treatment of lead contaminated soils. *J. Environ. Eng.* **2005**, *131*, 38–48. [CrossRef]
29. Wu, Z.L.; Deng, Y.F.; Chen, Y.G.; Gao, Y.F.; Zha, F.S. Long-term desalination leaching effect on compression/swelling behaviour of Lianyungang marine soft clays. *Bull. Eng. Geol. Environ.* **2021**, *80*, 8099–8107. [CrossRef]
30. Zha, F.S.; Liu, J.J.; Xu, L.; Cui, K.R. Effect of cyclic drying and wetting on engineering properties of heavy metal contaminated soils solidified/stabilized with fly ash. *J. Cent. South. Univ.* **2013**, *20*, 1947–1952. [CrossRef]
31. Kalkan, E. Impact of wetting–drying cycles on swelling behavior of clayey soils modified by silica fume. *Appl. Clay Sci.* **2011**, *52*, 345–352. [CrossRef]
32. Zha, F.S.; Liu, S.Y.; Du, Y.J.; Cui, K.R. Behavior of expansive soils stabilized with fly ash. *Nat. Hazards* **2008**, *47*, 509–523. [CrossRef]
33. Hafsteinsdottir EG, White DA, Gore DB, Stark SC Products and stability of phosphate reactions with lead under freeze-thaw cycling in simple systems. *Environ. Pollut.* **2011**, *159*, 3496–3503. [CrossRef] [PubMed]
34. Wei, M.L.; Du, Y.J.; Reddy, K.R.; Wu, H.L. Effects of freeze-thaw on characteristics of new KMP binder stabilized Zn- and Pb-contaminated soils. *Environ. Sci. Pollut. Res. Int.* **2015**, *22*, 19473–19484. [CrossRef]
35. Zhou, Z.W.; Ma, W.; Zhang, S.J.; Mu, Y.H.; Li, G.Y. Effect of freeze-thaw cycles in mechanical behaviors of frozen loess. *Cold Reg. Sci. Technol.* **2018**, *146*, 9–18. [CrossRef]
36. Liu, J.J.; Zha, F.S.; Xu, L.; Kang, B.; Yang, C.B.; Feng, Q.; Zhang, W.; Zhang, J.W. Strength and microstructure characteristics of cement-soda residue solidified/stabilized zinc contaminated soil subjected to freezing–thawing cycles. *Cold Reg. Sci. Technol.* **2020**, *172*, 102992.
37. Zhao, R.F.; Zhang, S.N.; Gao, W.; He, J.; Wang, J.; Jin, D.; Nan, B. Factors effecting the freeze thaw process in soils and reduction in damage due to frosting with reinforcement: A review. *Bull. Eng. Geol. Environ.* **2019**, *78*, 5001–5010. [CrossRef]
38. Su, Y.Y.; Li, P.; Ren, Z.P.; Xiao, L.; Zhang, H. Freeze-thaw effects on erosion process in loess slope under simulated rainfall. *J. Arid. Land* **2021**, *12*, 937–949. [CrossRef]
39. Wei, H.B.; Jiao, Y.B.; Liu, H.B. Effect of freeze–thaw cycles on mechanical property of silty clay modified by fly ash and crumb rubber. *Cold Reg. Sci. Technol.* **2015**, *116*, 70–77. [CrossRef]
40. Wang, T.L.; Liu, Y.J.; Yan, H.; Xu, L. An experimental study on the mechanical properties of silty soils under repeated freeze–thaw cycles. *Cold Reg. Sci. Technol.* **2015**, *112*, 51–65. [CrossRef]
41. Yang, Z.; Li, X.; Li, D.; Wang, Y.; Liu, X. Effects of Long-Term Repeated Freeze-Thaw Cycles on the Engineering Properties of Compound Solidified/Stabilized Pb-Contaminated Soil: Deterioration Characteristics and Mechanisms. *Int. J. Environ. Res. Public Health* **2020**, *17*, 1798. [CrossRef] [PubMed]
42. Yang, Z.P.; Chang, J.Z.; Wang, Y.; Li, X.Y.; Li, S. Effects of Long-Term Freeze-Thaw Cycles on the Properties of Stabilized/Solidified Lead-Zinc-Cadmium Composite-Contaminated Soil. *Int. J. Environ. Res. Public Health* **2021**, *18*, 6114. [CrossRef] [PubMed]
43. Chen, X.D.; Lu, X.W.; Yang, G. Sources identification of heavy metals in urban topsoil from inside the Xi'an Second Ringroad, NW China using multivariate statistical methods. *Catena* **2012**, *98*, 73–78. [CrossRef]
44. Yao, Y.R.; Li, J.; He, C.; Hu, X.; Yin, L.; Zhang, Y.; Zhang, J.; Huang, H.Y.; Yang, S.G.; He, H.; et al. Distribution Characteristics and Relevance of Heavy Metals in Soils and Colloids Around a Mining Area in Nanjing, China. *Bull. Environ. Contam. Toxicol.* **2021**, *107*, 996–1003. [CrossRef] [PubMed]
45. Liu, H.B.; Liu, S.J.; He, X.S.; Dang, F.; Tang, Y.Y.; Xi, B.D. Effects of landfill refuse on the reductive dechlorination of pentachlorophenol and speciation transformation of heavy metals. *Sci. Total Environ.* **2021**, *760*, 144122. [CrossRef]
46. McLellan, B.C.; Williams, R.P.; Lay, J.; van Riessen, A.; Corder, G.D. Costs and carbon emissions for geopolymer pastes in comparison to ordinary portland cement. *J. Clean. Prod.* **2011**, *19*, 1080–1090. [CrossRef]
47. Cuisinier, O.; Le Borgne, T.; Deneele, D.; Masrouri, F. Quantification of the effects of nitrates, phosphates and chlorides on soil stabilization with lime and cement. *Eng. Geol.* **2011**, *117*, 229–235. [CrossRef]
48. Yang, Z.P.; Li, X.Y.; Wang, Y.; Chang, J.Z.; Liu, X.R. Trace element contamination in urban topsoil in China during 2000-2009 and 2010-2019: Pollution assessment and spatiotemporal analysis. *Sci. Total Environ.* **2020**, *758*, 143647. [CrossRef]
49. PeÂrez-Cid, B.; Lavilla, I.; Bendicho, C. Application of microwave extraction for partitioning of heavy metals in sewage sludge. *Anal. Chim. Acta* **1999**, *378*, 201–210. [CrossRef]
50. Liu, D.D.; Miao, D.R.; Liu, F. Evaluation of the As, Cu and Pb Immobilizing Efficiency by Tessier, TCLP and SBET Method. *Adv. Mater. Res.* **2014**, *878*, 520–521. [CrossRef]
51. Linker, R.; Shmulevich, I.; Kenny, A.; Shaviv, A. Soil identification and chemometrics for direct determination of nitrate in soils using FTIR-ATR mid-infrared spectroscopy. *Chemosphere* **2005**, *61*, 652–658. [CrossRef] [PubMed]

52. Shi, T.; Yang, Z.P.; Zheng, L.W. FTIR spectra for early age hydration of cement-based composites incorporatted with CNTs. *Acta Mater. Compos. Sin.* **2017**, *34*, 653–660.
53. Yan, K.Z.; Guo, Y.X.; Li, N.J.; Cheng, F.Q. Effect and Mechanism Analysis of Calcium Oxide Additive on the Sodium Carbonate Activation of Fly Ash. *Bull. Chin. Ceram. Soc.* **2018**, *37*, 1003–1009.
54. Correia, A.A.S.; Matos, M.P.S.R.; Gomes, A.R.; Rasteiro, M.G. Immobilization of Heavy Metals in Contaminated Soils—Performance Assessment in Conditions Similar to a Real Scenario. *Appl. Sci.* **2020**, *10*, 7950. [CrossRef]
55. Guo, B.; Liu, B.; Yang, J.; Zhang, S.G. The mechanisms of heavy metal immobilization by cementitious material treatments and thermal treatments: A review. *J. Environ. Manag.* **2017**, *193*, 410–422. [CrossRef] [PubMed]
56. Zha, F.S.; Liu, C.M.; Kang, B.; Yang, X.H.; Zhou, Y.; Yang, C.B. Acid rain leaching behavior of Zn-contaminated soils solidified/stabilized using cement-soda residue. *Chemosphere* **2021**, *281*, 130916. [CrossRef]
57. Fei, Y.; Yan, X.L.; Zhong, L.R.; Li, F.S.; Du, Y.J.; Li, C.P.; Lv, H.Y.; Li, Y.H. On-Site Solidification/Stabilization of Cd, Zn, and Pb Co-Contaminated Soil Using Cement: Field Trial at Dongdagou Ditch, Northwest China. *Environ. Eng. Sci.* **2018**, *35*, 1329–1339. [CrossRef]
58. Zhang, W.L.; Zhao, L.Y.; Yuan, Z.J.; Li, D.Q.; Morrison, L. Assessment of the long-term leaching characteristics of cement-slag stabilized/solidified contaminated sediment. *Chemosphere* **2021**, *267*, 128926. [CrossRef]
59. Yoon, D.H.; Choi, W.S.; Hong, Y.K.; Lee, Y.B.; Kim, S.C. Effect of chemical amendments on reduction of bioavailable heavy metals and ecotoxicity in soil. *Appl. Biol. Chem.* **2019**, *62*, 1–7. [CrossRef]
60. Bai, B.; Nie, Q.K.; Zhang, Y.K.; Wang, X.L.; Hu, W. Cotransport of heavy metals and SiO2 particles at different temperatures by seepage. *J. Hydrol.* **2021**, *597*, 125771. [CrossRef]
61. Ouhadi, V.R.; Yong, R.N.; Deiranlou, M. Enhancement of cement-based solidification/stabilization of a lead-contaminated smectite clay. *J. Hazard. Mater.* **2021**, *403*, 123969. [CrossRef] [PubMed]
62. Velichenko, A.B.; Portillo, J.; Sarret, M.; Muller, C. Zinc dissolution in ammonium chloride electrolytes. *J. Appl. Electrochem.* **1999**, *29*, 1119–1123. [CrossRef]
63. Mitani, T.; Ogawa, M. Cadmium leaching by acid rain from cadmium-enriched activated sludge applied in soil. *J. Environ. Health* **1998**, *33*, 1569–1581. [CrossRef]

applied sciences

MDPI

*Article*

# Molecular Dynamics Simulation of Nanoscale Elastic Properties of Hydrated Na-, Cs-, and Ca-Montmorillonite

**Lianfei Kuang [1], Qiyin Zhu [1,*], Xiangyu Shang [2] and Xiaodong Zhao [1]**

[1] State Key Laboratory for Geomechanics and Deep Underground Engineering, China University of Mining and Technology, Xuzhou 221116, China; kuanglf@cumt.edu.cn (L.K.); zxd@cumt.edu.cn (X.Z.)
[2] School of Mechanics and Civil Engineering, China University of Mining and Technology, Xuzhou 221116, China; xyshang@cumt.edu.cn
* Correspondence: qiyin.zhu@cumt.edu.cn

**Abstract:** The knowledge of nanoscale mechanical properties of montmorillonite (MMT) with various compensation cations upon hydration is essential for many environmental engineering-related applications. This paper uses a Molecular Dynamics (MD) method to simulate nanoscale elastic properties of hydrated Na-, Cs-, and Ca-MMT with unconstrained system atoms. The variation of basal spacing of MMT shows step characteristics in the initial crystalline swelling stage followed by an approximately linear change in the subsequent osmotic swelling stage as the increasing of interlayer water content. The water content of MMT in the thermodynamic stable-state conditions during hydration is determined by comparing the immersion energy and hydration energy. Under this stable hydration state, the nanoscale elastic properties are further simulated by the constant strain method. Since the non-bonding strength between MMT lamellae is much lower than the boning strength within the mineral structure, the in-plane and out-of-plane strength of MMT has strong anisotropy. Simulated results including the stiffness tensor and linear elastic constants based on the assumption of orthotropic symmetry are all in good agreement with results from the literature. Furthermore, the out-of-plane stiffness tensor components of $C_{33}$, $C_{44}$, and $C_{55}$ all fluctuate with the increase of interlayer water content, which is related to the formation of interlayer H-bonds and atom-free volume ratio. The in-plane stiffness tensor components $C_{11}$, $C_{22}$, and $C_{12}$ decrease nonlinearly with the increase of water content, and these components are mainly controlled by the bonding strength of mineral atoms and the geometry of the hydrated MMT system. Young's modulus in all three directions exhibits a nonlinear decrease with increasing water content.

**Keywords:** molecular dynamics; mechanical properties; montmorillonite; basal spacing

**Citation:** Kuang, L.; Zhu, Q.; Shang, X.; Zhao, X. Molecular Dynamics Simulation of Nanoscale Elastic Properties of Hydrated Na-, Cs-, and Ca-Montmorillonite. *Appl. Sci.* **2022**, *12*, 678. https://doi.org/10.3390/app12020678

Academic Editor: Bing Bai

Received: 17 December 2021
Accepted: 10 January 2022
Published: 11 January 2022

**Publisher's Note:** MDPI stays neutral with regard to jurisdictional claims in published maps and institutional affiliations.

**Copyright:** © 2022 by the authors. Licensee MDPI, Basel, Switzerland. This article is an open access article distributed under the terms and conditions of the Creative Commons Attribution (CC BY) license (https://creativecommons.org/licenses/by/4.0/).

## 1. Introduction

Montmorillonite (MMT) consists of well-defined layers separated by interlayer spaces and has great water absorption potential [1–4]. Thus, it is often used as clay barriers or adsorption material in environmental geotechnical engineering, for example, the backfill in the nuclear waste disposal and the cushion in the landfill [5–10]. It is very challenging to directly measure the fundamental mechanical properties of MMT [11,12]. Atomic force acoustic microscopy is used to determine the elastic properties of clay mineral aggregates by measuring adhesion forces [13–15]. Nanoindentation and ultrasonic pulse velocity technology (UPV) are also used to measure the elastic stiffness constants of clays and shale samples [16–18]. However, these techniques are powerless to measure the anisotropic mechanical properties of MMT, due to the complications in sample preparation and even the testing process.

In contrast to difficulty in experimental methods, molecular dynamics (MD) simulation is a supplemental way to model and understand the properties of hydrated clay minerals on an atomic scale [1,19–21]. With the development of polymer–clay nanocomposites in recent years, several studies on the nanomechanical properties of MMT minerals or hydrated MMT systems have emerged. The authors in [18] reported for the first time the stress–strain response of rock-forming minerals by MD simulation. The authors in [22] performed MD simulations to study the flexibility and the mechanical behavior of a single clay layer in a completely exfoliated state and found that the critical stress of a clay layer bending fracture is 0.8 MPa in both in-plane directions. In [23], the authors presented results for the elastic properties of a single lamella of MMT by MD simulation and further pointed out that the elastic constants characteristic of a thin plate is closely related to the thickness of the nanoplate. Based on the analogous minerals and modulus-density relations, ref. [24] deduced a convergence of opinion in the range 178–265 GPa for the elastic moduli of smectite clay platelets. The authors in [25] systematically simulated the structure and the thermomechanical properties of an isolated clay nanoplate and MMT crystals intercalated by water or polyethylene oxide. In [26], the authors clarified the linear elastic properties including tensile moduli, shear moduli, and potential failure mechanisms as a function of cation density and stress for the minerals pyrophyllite, MMT, and mica. In [27], the authors examined the mechanism of bending, the stored energy, and the failure of several clay minerals. They revealed that molecular contributions to the bending energy include bond stretching and bending of bond angles in the mineral as well as rearrangements of alkali ions on the surface of the layers. The authors in [28] further simulated the elastic and structural properties of muscovite as a function of temperature, pressure, and strain. The results demonstrate that the elastic properties of muscovite depend on both temperature and pressure. MD with the CLAYFF force field was used in [29] to simulate isothermal isobaric water adsorption of interlayer MMT, and nanoscale elastic properties of the clay-interlayer water system are calculated from the potential energy of the model system. Similar simulations have also been carried out on MMT by implementing the elastic bath method [30]. The mechanical properties of Na-MMT were investigated in [31] from the view of water content by MD, and the hysteresis phenomena of elastic constant during the swelling and shrinking was found. In addition, researchers found that the mechanical behavior of MMT crystal exhibits a clear dissymmetry between compression and tension and an important dependency on mean stress [32].

The above simulation studies are generally based on the strain method, that is, the stress is calculated by changing the size of the simulation box. The stress method and the large-scale fluctuation method are also usually adopted. For example, using steered molecular dynamics (SMD) technology, the mechanical response of the interlayer of hydrated MMT was evaluated by [33]. Using grid-computing technology, ref. [34] simulated MMT clay large-scale systems containing up to approximately ten million atoms; large-scale systems exhibit emergent behavior with increasing size, and the material mechanical properties were calculated based on thermal bending fluctuations. From the surveyed status of nanoscale mechanical properties of clay minerals, it can be found that the stress–strain response of minerals can be revealed by different methods (constant strain, SMD, or the large-scale fluctuation method) based on different force fields and different platforms. However, the moisture content under most simulated hydration conditions is usually arbitrarily selected and generally restricts some movement directions of clay plates or even the interlayer water molecules which affect the mechanical response characteristics of the hydrated mineral system.

The goal of this study is to simulate the nanoscale mechanical properties of hydrated MMT minerals with three cations (Na, Ca, and Cs) at variable water contents. In the simulation, all degrees of freedom of atoms are released, and the water content in different hydration states is determined according to stable-state thermodynamic conditions. To the best of our knowledge, no such treatments have been reported to study the mechanical properties of the MMT mineral up to now. The quantitative values of the basal spacing for different compensation cationic MMTs are firstly studied. The relative stabilities of different states are determined by comparing the immersion energy and hydration energy between MMT systems, and, then, the corresponding moisture content of thermodynamics stable states is obtained. Finally, the nanoscale elastic properties of MMT are further simulated by the constant strain method under the stable state water content.

## 2. Model and Methods

### 2.1. Molecular Models

Wyoming-type MMT, which has been widely simulated, was selected as the model clay in this study, as shown in Figure 1. The initial unit cell parameters are $a$ = 5.23 Å and $b$ = 9.06 Å, and the c-axis increases with increasing water content, the unit cell angles are $\alpha = \gamma = 90°$, $\beta = 99°$. The x and y axes were chosen parallel to the clay layer, while the $z$-axis was orthogonal to the clay layer. The unit cell of MMT was replicated (4a × 2b × 1c) in the x, y, and z directions so that the supercell contained 8-unit cells with approximate dimensions in the XY plane of 21 Å × 18 Å and 9.6 Å in the $z$-axis. One of every 8 octahedral $Al^{3+}$ atoms was substituted with an $Mg^{2+}$ atom and one of every 4 tetrahedral $Si^{4+}$ atoms was substituted with an $Al^{3+}$ atom. The isomorphic substitutions were distributed randomly obeying Lowenstein's rule. This extent of substitution led to a layer charge of −0.75 e per unit cell and the unbalanced charge will be compensated by $Na^+$, $Ca^{2+}$, and $Cs^+$ which are commonly adopted in engineering applications [12,35]. In addition, the interlayer space was randomly filled with a given number $n$ of water molecules, the number $n$ ranged from 0 to 160, and a total of 23 clay–water-ion systems will be evaluated. The structural formula of the simulated layer of Na- and Cs-MMT is $M_{0.75}\{Si_{7.75}Al_{0.25}\}[Al_{3.5}Mg_{0.5}]O_{20}(OH)_4 \cdot nH_2O$ (M = Na or Cs), whereas for the Ca-MMT, it can be expressed as $Ca_{0.375}\{Si_{7.75}Al_{0.25}\}[Al_{3.5}Mg_{0.5}]O_{20}(OH)_4 \cdot nH_2O$.

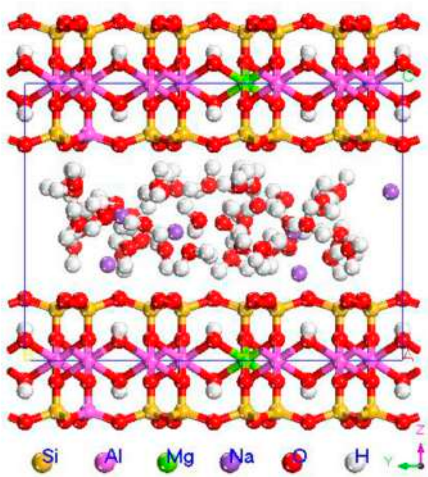

**Figure 1.** Super-cell model of Na-montmorillonite (Mg octahedral are green, Al octahedral and tetrahedral purple, Si tetrahedral brown, O atoms red, H atoms white, and Na ions cyan).

### 2.2. Simulation Protocol

MD simulations were conducted in Forcite module in the Material studio 8.0 simulation package and the CLAYFF force field, developed by [36]. The latter is a flexible model which describes hydrated mineral systems through nonbonded electrostatic and Lennard–Jones terms. It can accurately reproduce structural and spectroscopic properties of clays, as well as dynamical and energetic properties of clay interlayer and aqueous interfaces. The interlayer water molecules were described with the flexible version of the simple point charge (SPC) potential. The potential energy of the system was evaluated with an 8.5 Å cutoff, a 0.5 Å spline, and buffer width for short-range van der Waals interaction. The Ewald summation for the electrostatic interaction was calculated with a precision of

$10^{-3}$ kcal/mol. Periodic boundary conditions were imposed on three dimensions to avoid interface effects.

The initial conformation of hydrated MMT needs optimization of the geometry first by searching for the minimum potential energy of the system. A smart algorithm was chosen for the optimization with a maximum number of 5000 cycles, and the convergence thresholds for the specified maximum energy and displacement changes were set as $1.0 \times 10^{-4}$ kcal/mol and $5.0 \times 10^{-5}$ Å, respectively. Following this, the final configuration from optimization was used as the initial configuration for the equilibration stage simulation in the NPT (isothermal–isobaric) ensemble at $P$ = 1 atm and $T$ = 298 K. Each system was equilibrated for 100 ps (105 steps) with a time step of 1 fs. The temperature and the pressure were controlled by a Nosé–Hoover–Langevin thermostat of 1 ps and a Berendsen barostat of 0.1 ps, respectively. Finally, following the thermal equilibration configurations, a microcanonical NVE ensemble was then performed for a 1 ns production simulation, and the time step was still set as 1 fs (NVE: Each system in the ensemble has the same energy, and the number of particles and volume of each system are usually the same). The data from all 1 ns trajectories of the NVE simulation runs were recorded every 500 fs and were used to analyze the microstructure and thermodynamic properties of hydrated MMT. By comparing the relative thermodynamic energy of different systems, the steady-state water content of hydrated MMT can be determined. Furthermore, the mechanical properties of the steady-state system will be further simulated by the constant strain method. The constant strain method obtains the elastic constants via minimizing the energy of the system and deforming the supercell parameters in 12 directions in order. To improve the statistical accuracy, the simulations of mechanical properties are carried out based on the production stage trajectory files obtained above, that is, 20 frames of instant conformation are extracted from the corresponding trajectory files. The strain step is set as 10, and the maximum strain in each strain step is set to 1% according to the linear elastic assumption. The final mechanical parameters are obtained by the geometric average of the 20 frames.

### *2.3. Methods for Calculating the Elastic Constants*

Acting on external forces, the hydrated MMT system will be in a state of stress. If the system is in equilibrium, the external forces must be exactly balanced by internal stress. In general, stress is a second rank tensor with nine components as in Equation (1):

$$\vec{\sigma} = \left[\sigma_{ij}\right] = \begin{bmatrix} \sigma_{xx} & \sigma_{xy} & \sigma_{xz} \\ \sigma_{xy} & \sigma_{yy} & \sigma_{yz} \\ \sigma_{xz} & \sigma_{yz} & \sigma_{zz} \end{bmatrix} \tag{1}$$

In an atomistic calculation, the internal stress tensor can be obtained using the so-called virial expression as in Equation (2):

$$\vec{\sigma} = -\frac{1}{V_0}\left(\sum_{i=1}^{N} m_i(\vec{v}_i \vec{v}_i^{\,T}) + \sum_{i<j} \vec{r}_{ij} \vec{F}_{ij}^{\,T}\right) \tag{2}$$

where index $i$ runs over all particles 1 through $N$; $m_i$, $\vec{v}_i$, and $\vec{F}_i$ denote the mass, velocity, and force acting on particle $i$, respectively; $V_0$ denotes the initial system volume.

The application of stress to the hydrated MMT system results in a change in the relative positions of particles within the system expressed quantitatively via the strain tensor as in Equation (3):

$$\vec{\varepsilon} = \left[\varepsilon_{ij}\right] = \begin{bmatrix} \varepsilon_{xx} & \varepsilon_{xy} & \varepsilon_{xz} \\ \varepsilon_{xy} & \varepsilon_{yy} & \varepsilon_{yz} \\ \varepsilon_{xz} & \varepsilon_{yz} & \varepsilon_{zz} \end{bmatrix} \tag{3}$$

For a parallelepiped (for example, a periodic simulation cell) characterized by the three column vectors $[\overrightarrow{a}_0\ \overrightarrow{b}_0\ \overrightarrow{c}_0]$ in some reference state, and by the vectors $[\overrightarrow{a}\ \overrightarrow{b}\ \overrightarrow{c}]$ in the deformed state, the strain tensor is given by Equation (4):

$$\overrightarrow{\varepsilon} = \frac{1}{2}\left[\left(\overrightarrow{h}_0^{T}\right)^{-1}\overrightarrow{G}\,\overrightarrow{h}_0^{-1} - 1\right] \tag{4}$$

where $\overrightarrow{h}_0$ denotes the matrix formed from the three column vectors $[\overrightarrow{a}_0\ \overrightarrow{b}_0\ \overrightarrow{c}_0]$, $\overrightarrow{h}$ denotes the corresponding matrix forms from $[\overrightarrow{a}\ \overrightarrow{b}\ \overrightarrow{c}]$, $T$ denotes the matrix transpose, and $\overrightarrow{G}$ denotes the metric tensor $\overrightarrow{h}^{T}\overrightarrow{h}$.

Therefore, the elastic stiffness coefficients, relating the various components of stress and strain, are defined by Equation (5):

$$\overrightarrow{C} = \left[C_{ijkl}\right] = \left.\frac{\partial\sigma_{ij}}{\partial\varepsilon_{kl}}\right|_{T,\varepsilon_{kl}} = \frac{1}{V_0}\left.\frac{\partial^2 A}{\partial\varepsilon_{ij}\partial\varepsilon_{kl}}\right|_{T,\varepsilon_{ij},\varepsilon_{kl}} \tag{5}$$

where $A$ denotes the Helmholtz free energy, and $T$ denotes temperature.

For small deformations, the relationship between the stresses and strains may be expressed in terms of a generalized Hooke's law:

$$\sigma_{ij} = C_{ijkl}\varepsilon_{kl} \tag{6}$$

and, alternatively:

$$\varepsilon_{ij} = S_{ijkl}\sigma_{kl} \tag{7}$$

where $C_{ijkl}$ and $S_{ijkl}$ denote stiffness tensor and compliance tensor, respectively.

Since both the stress and strain tensors are symmetric, it is often convenient to simplify these expressions by making use of Voigt vector notation. The stress is represented as in Equation (8):

$$\begin{bmatrix} \sigma_{xx} & \sigma_{xy} & \sigma_{xz} \\ \sigma_{xy} & \sigma_{yy} & \sigma_{yz} \\ \sigma_{xz} & \sigma_{yz} & \sigma_{zz} \end{bmatrix} \Rightarrow \begin{bmatrix} \sigma_1 & \tau_6 & \tau_5 \\ & \sigma_2 & \tau_4 \\ & & \sigma_3 \end{bmatrix} \tag{8}$$

The strain is represented as in Equation (9):

$$\begin{bmatrix} \varepsilon_{xx} & \varepsilon_{xy} & \varepsilon_{xz} \\ \varepsilon_{xy} & \varepsilon_{yy} & \varepsilon_{yz} \\ \varepsilon_{xz} & \varepsilon_{yz} & \varepsilon_{zz} \end{bmatrix} \Rightarrow \begin{bmatrix} \varepsilon_1 & \gamma_6 & \gamma_5 \\ & \varepsilon_2 & \gamma_4 \\ & & \varepsilon_3 \end{bmatrix} \tag{9}$$

The generalized Hooke's law is thus often written as in Equation (10):

$$\begin{bmatrix} \sigma_1 \\ \sigma_2 \\ \sigma_3 \\ \tau_4 \\ \tau_5 \\ \tau_6 \end{bmatrix} = \begin{bmatrix} C_{11} & C_{12} & C_{13} & C_{14} & C_{15} & C_{16} \\ & C_{22} & C_{23} & C_{24} & C_{25} & C_{26} \\ & & C_{33} & C_{34} & C_{35} & C_{36} \\ & & & C_{44} & C_{45} & C_{46} \\ & & & & C_{55} & C_{56} \\ & & & & & C_{66} \end{bmatrix} \begin{bmatrix} \varepsilon_1 \\ \varepsilon_2 \\ \varepsilon_3 \\ \gamma_4 \\ \gamma_5 \\ \gamma_6 \end{bmatrix} \tag{10}$$

alternatively:

$$\sigma_i = C_{ij}\varepsilon_j \tag{11}$$

where $C_{ij}$ denotes the stiffness tensor and is a symmetric matrix of 6 × 6. The number of independent elastic constants for any system is 21. The mineral of MMT crystals belongs to the monoclinic system ($a \neq b \neq c$, $\alpha = \beta = 90^\circ \neq \gamma$) and has C2/M symmetry. It, then, only needs 13 independent parameters to describe its stiffness tensor. However, according to the study in [23], the MMT crystal can be considered approximately as orthotropic symmetry, thus further reducing the stiffness tensor parameters to 9 to characterize the sheet. These 9 independent elastic constants include 3 Young's moduli ($E_1$, $E_2$, $E_3$), 3 shear moduli ($G_{23}$, $G_{31}$ and $G_{12}$), and 3 Poisson's ratios ($\mu_{12}$, $\mu_{13}$ and $\mu_{23}$). In terms of these parameters, the stiffness tensor $C_{ij}$ can be further expressed as in Equation (12):

$$\begin{bmatrix} C_{11} & C_{12} & C_{13} & 0 & 0 & 0 \\ C_{21} & C_{22} & C_{23} & 0 & 0 & 0 \\ C_{31} & C_{32} & C_{33} & 0 & 0 & 0 \\ 0 & 0 & 0 & C_{44} & 0 & 0 \\ 0 & 0 & 0 & 0 & C_{55} & 0 \\ 0 & 0 & 0 & 0 & 0 & C_{66} \end{bmatrix} = \begin{bmatrix} \frac{1-\mu_{23}\mu_{32}}{E_2E_3\Delta} & \frac{\mu_{21}+\mu_{31}\mu_{23}}{E_2E_3\Delta} & \frac{\mu_{31}+\mu_{21}\mu_{32}}{E_2E_3\Delta} & 0 & 0 & 0 \\ \frac{\mu_{12}+\mu_{13}\mu_{32}}{E_3E_1\Delta} & \frac{1-\mu_{31}\mu_{13}}{E_3E_1\Delta} & \frac{\mu_{32}+\mu_{31}\mu_{12}}{E_3E_1\Delta} & 0 & 0 & 0 \\ \frac{\mu_{13}+\mu_{12}\mu_{23}}{E_1E_2\Delta} & \frac{\mu_{23}+\mu_{13}\mu_{21}}{E_1E_2\Delta} & \frac{1-\mu_{12}\mu_{21}}{E_1E_2\Delta} & 0 & 0 & 0 \\ 0 & 0 & 0 & 2G_{23} & 0 & 0 \\ 0 & 0 & 0 & 0 & 2G_{31} & 0 \\ 0 & 0 & 0 & 0 & 0 & 2G_{12} \end{bmatrix} \tag{12}$$

where $\Delta = \frac{1-\mu_{12}\mu_{21}-\mu_{23}\mu_{32}-\mu_{31}\mu_{13}-2\mu_{12}\mu_{23}\mu_{31}}{E_1E_2E_3}$.

Therefore, the key to characterizing the elastic mechanical properties of the MMT–water-ion system at the nanoscale level is to obtain the parameters of the stiffness tensor or the compliance tensor.

## 3. Results and Discussion

### 3.1. Swelling and Thermodynamics Analysis

To obtain the water content corresponding to the thermodynamic steady-state in the hydration process of MMT, the strategy of simulating 23 different water content systems was adopted. The interlayer space of the MMT lamellae increases with the increase of water content, and this swelling process can be described by using the parameter of basal spacing. The basal spacing can be obtained from the view of water content by averaging the system volume during the production stage of simulation and defined as in Equation (13):

$$d_{001} = \frac{\langle V \rangle}{\langle a \rangle \langle b \rangle \sin\langle \alpha \rangle} \tag{13}$$

where $<V>$ denotes the statistically averaged volume, and $<a>$ $<b>$ $<\alpha>$ are the statistically averaged parameters of the simulation supercell.

Figure 2 illustrates the variation of basal spacing of different hydrated montmorillonite systems as a function of water content from this study and available results from the literature. In the early stage of crystalline swelling, the basal spacing increases from step to step, while the step characteristic (plateau) disappears, and shows approximately linear variation in the following stage of osmotic swelling. The swelling curves of MMT with different compensation cations are different. The basal spacing of Cs-MMT is greater than Na- and Ca-MMT under the same water content. However, there is almost no difference between the latter two. This is mainly due to the fact that $Cs^+$ ions are a heavy metal ion and their ion radius is about 1.7 times that of $Na^+$ and $Ca^{2+}$ ions, while the latter two's ion radii are almost the same. The simulated results can well penetrate the distribution range of other available measurements.

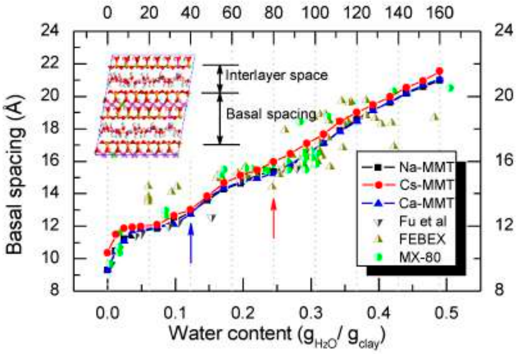

**Figure 2.** The simulated and experimental basal spacing of montmorillonite as a function of water content (*g* denotes molecular mass).

It has been shown that the energy contribution to free energy dominates clay swelling and the entropy term only played a minor role. The local minima of the swelling energy curve correspond to the stable hydration state. Hence, the relative stabilities of different states can be determined by immersion energy and hydration energy. The immersion energy is defined as in Equation (14):

$$Q = \langle E(N) \rangle - \left\langle E(N^0) \right\rangle - \left(N - N^0\right) E_{bulk} \tag{14}$$

Here <$E(N)$> is the average potential energy of the hydrate with water content $N$, and <$E(N^0)$> is the average energy of the referential hydration state (the state with the highest water content, 49%, was selected). $E_{bulk}$ is the mean interaction potential of the bulk flexible SPC water; $E_{bulk} = -41.5392$ kJ/mol. The immersion energy $Q$ is the energy released when MMT with water content $N$ transforms into the referenced state with water content $N^0$ by adsorbing water from bulk water.

The hydration energy is defined as in Equation (15)

$$\Delta E = \frac{\langle E(N) \rangle - \langle E(0) \rangle}{N} \tag{15}$$

Here <$E(0)$> is the average potential energy of the dry MMT. The hydration energy $\Delta E$ evaluates the energy change associated with water uptake by the dry clay.

The simulated hydration energy and immersion energy curves of MMT with different compensation cations are presented in Figure 3. For Na- and Cs-MMT the local minima occur when the interlayer water molecular number is 40 and 80 in the hydration energy curves, while Ca-MMT has only a global minimum at low water content. Correspondingly, in the immersion energy curves of Na- and Cs-MMT, local minima occur when the interlayer water molecular numbers are also 40 and 80. The global minima of Cs-MMT is found at $n = 80$, while Na-MMT global minima is located at $n = 160$, as shown by the enlarged illustration in Figure 3. Meanwhile, the variation of the Ca-MMT immersion energy curve decreases monotonically with the increase of water content, and the global minima occurs also at $n = 160$. Then, since the local minima of the swelling energy corresponds to the thermodynamic stable states, it can be deduced that the Na- and Cs-MMT will form the single- and double-layer stable hydrated states when the number of interlayer water molecules reach 40 and 80 respectively. The double-layer hydrate for Cs-MMT is in the most stable state. Thus, the $Cs^+$ ions can inhibit swelling. The global minima of Na-MMT is located at $n = 160$. After forming the first and second hydration layer, Na-MMT will continue expansion to the osmotic swelling stage, namely that the $Na^+$ ions promote swelling in contrast with $Cs^+$. For Ca-MMT, its role in promoting expansion is even more pronounced. The intermediate state of the first or second hydration layer will not form during the swelling process, and the osmotic swelling stage will rapidly and directly develop. The nanoscale elastic properties of these stable state water content systems will be further simulated in the following sections.

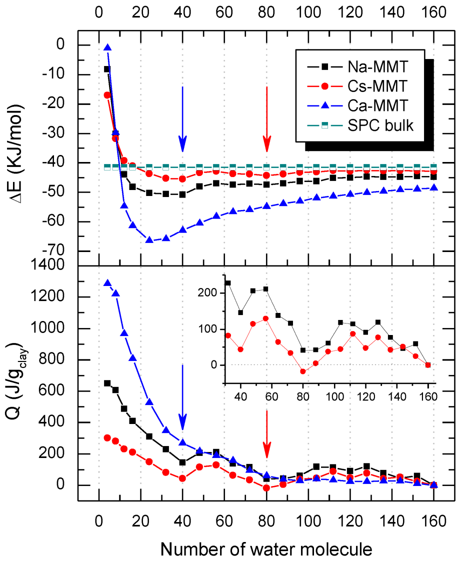

**Figure 3.** Hydration energy and immersion energy of montmorillonite as a function of increasing interlayer water molecule number.

### 3.2. Nanoscale Elastic Properties

To fully demonstrate the yield behavior of the MMT mineral, the maximum strain of each direction is expanded to 10% and the corresponding calculation step is increased to 100 steps. The stress–strain curves of the typical MMT system obtained from simulation are shown in Figure 4, where the interlayer compensation cation is $Ca^{2+}$ ion, and the interlayer water number $n$ is 80, corresponding to bilayer hydration.

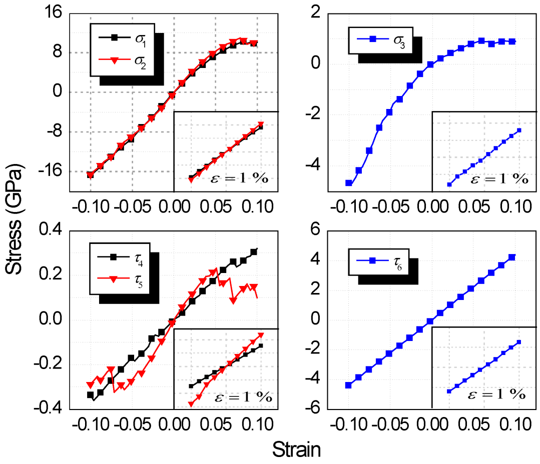

**Figure 4.** Typical stress–strain behavior for hydrated Ca-montmorillonite.

The micromechanical properties of hydrated MMT show obvious anisotropy. The in-plane uniaxial tensile and compressive strength of MMT is approximately equal (for $\sigma_1$ and $\sigma_2$), while the tensile strength is slightly less than the compressive strength. When the tensile strain reaches about 7%, the material yields. Meanwhile, the compressive stress–strain relationship shows a good linear relationship within the maximum compressive strain (10%). The tensile and compressive strength ($\sigma_3$) of MMT orthogonal to the mineral plane is much lower than that in-plane strength ($\sigma_1$ and $\sigma_2$). This is mainly due to the appearance of the interlayer water in MMT lamellae, and the bonding strength between the MMT crystal and water molecule through non-bonding is much lower than that of covalent or ionic bonding in the mineral plane. In addition, the compression of MMT in the Z direction shows obvious non-linear characteristics and hardening under high pressure, which is different from the linear characteristics in the crystal plane.

The hydration molecular layer that mixed within MMT lamellae has a certain shear strength (τ4 and τ5) and also shows anisotropy along with different directions of the MMT crystal plane. The shear stiffness of the interlayer water along the Y direction (τ5) is slightly larger than that in the X direction (τ4), while its shear strength is slightly lower. The shear capability of MMT lamellae is very high (τ6) and shows good linear characteristics in the simulated strain ranges.

By comparing the quantitative values of in-plane strength, it was found that the in-plane compressive strength of hydrated MMT is the largest, followed by tensile strength and shear strength. Similarly, this variation also applies to the strengths that are perpendicular to the mineral plane.

All of the stress responses show good linearity in the range of 1% small strain, and this is illustrated in the lower right of each block in Figure 4. This also shows that the linear elastic constants calculated by the small strain of 1% are reliable. The stiffness tensor and linear elastic constants of typical MMT in the 1% strain range corresponding to Figure 4 are listed in Table 1.

**Table 1.** Typical stiffness coefficients and elastic constants of hydrated Ca-MM (GPa).

| $C_{ij}$ | 1 | 2 | 3 | 4 | 5 | 6 |
|---|---|---|---|---|---|---|
| 1 | 189.6710 ± 1.0140 | 81.7433 ± 0.8172 | 10.1290 ± 0.4701 | 1.2430 ± 0.3777 | −10.4597 ± 0.2771 | 0.4964 ± 0.4787 |
| 2 | | 212.5464 ± 1.7814 | 8.4054 ± 0.4993 | 3.5123 ± 0.4520 | −3.4307 ± 0.3618 | 1.1526 ± 1.0715 |
| 3 | | | 28.4335 ± 0.5057 | 0.3278 ± 0.2660 | 1.3468 ± 0.1654 | 0.1060 ± 0.2955 |
| 4 | | | | 4.2630 ± 0.1881 | −0.6221 ± 0.1371 | −2.7480 ± 0.2758 |
| 5 | | Symmetric | | | 5.4343 ± 0.1049 | 0.3864 ± 0.2236 |
| 6 | | | | | | 45.4441 ± 0.6942 |
| Young's modulus | $E_1$ | 139.1605 | $E_2$ | 174.2115 | $E_3$ | 27.0289 |
| Shear modulus | $G_{23}$ | 2.1315 | $G_{31}$ | 2.7172 | $G_{12}$ | 22.7221 |
| Poisson's ratios | $\mu_{12}$<br>0.3463 | $\mu_{21}$<br>0.4335 | $\mu_{13}$<br>0.3436 | $\mu_{31}$<br>0.0667 | $\mu_{23}$<br>0.1199 | $\mu_{32}$<br>0.0186 |
| Bulk modulus | | | 70.1340 | | | |
| Compressibility (1/TPa) | | | 38.6319 | | | |

The simulated stiffness tensor components in Table 1 are in good agreement with simulations and measurements in the literature. The in-plane components $C_{11}$ and $C_{22}$ of the MMT with water bilayer at 300 K are 189 GPa and 191 GPa, respectively, from [25], which are almost equal to the results of this study that $C_{11}$ = 189 GPa and $C_{22}$ = 212 GPa. Furthermore, there are differences in the in-plane Young's moduli $E_1$ and $E_2$ which are derived from the stiffness tensor, and these differences are induced by the different topologies of trivalent cations in dioctahedral structure of MMT, as shown in Figure 5. However, the in-plane Young's moduli ($E_1$ and $E_2$) are all much higher than the Young's modulus perpendicular to the plane ($E_3$). On the contrary, the in-plane shear moduli ($G_{23}$ and $G_{31}$) are lower than the shear modulus perpendicular to the plane ($G_{12}$). The larger difference of Poisson's ratio in different directions once again shows the anisotropy of the MMT structure. The boning strength in the mineral plane is much higher than that of non-bonding strength between mineral lamellae.

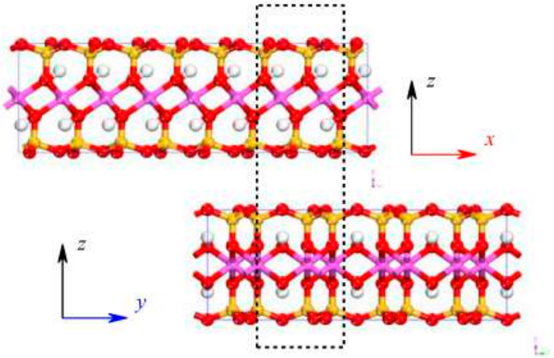

**Figure 5.** Different topologies of Al atom in the dioctahedral structure of montmorillonite.

The evolution of elastic properties of hydrated MMT under different stable state water content will be further illustrated by analyzing the changes of some components in the stiffness tensor. To validate the study, the simulation results from [29] and UPV test results from [17] are adopted for comparison due to the high correlation with the work in this study. The authors in [29] gave the variation of stiffness components during the hydration process of Na-Wyoming MMT with a water content of 0–40%. The authors in [17] obtained the range of elastic stiffness constants of smectite minerals on the microscale based on UPV test results of clay composition in shale.

For compression of clay under high pressure, the most concerning component of the stiffness tensor is $C_{33}$, that is, the ability to resist deformation in the direction of perpendicular to the mineral plane. Figure 6 shows the variation of $C_{33}$ obtained upon hydration by [29], Na-, Cs-, Ca- MMT in this study under different stable state conditions, and the test range results of [17]. Since the stiffness tensor elements in this study are obtained by a statistical average of 20 frame trajectory files, the statistical standard deviation of data is also given in Figure 6.

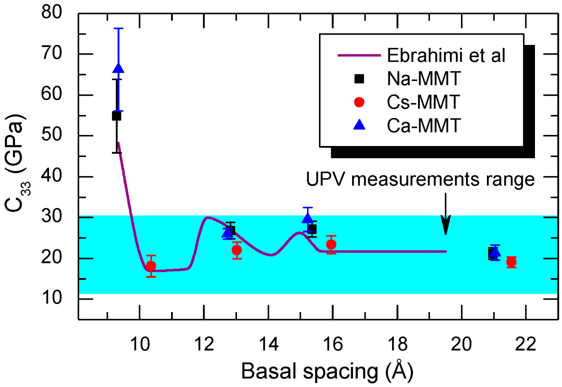

**Figure 6.** The $C_{33}$ elastic constant as a function of basal layer spacing.

Ebrahimi et al. (2012) revealed that $C_{33}$ decreased sharply from dry MMT to the formation of the first hydrated layer between lamellae, then increased to a local maximum with the formation of the stable hydrated layer, and finally maintained a constant until the basic spacing d > 15.6 Å [29]. The values of $C_{33}$ obtained in this study are in good agreement with the results of [29], apart from the first hydrated layer. The $C_{33}$ of Ca-MMT is slightly higher than that of Na-MMT, while the $C_{33}$ of Cs-MMT is the lowest among all the same hydrated states. Apart from the dry MMT, all of the simulated $C_{33}$ fall well into the given range of UPV measured by [17] ($C_{33}$ = 11.5~30.4 GPa).

The in-plane stiffness tensor components $C_{11}$, $C_{22}$, and $C_{12}$, which reflect the Poisson effect in the plane, are shown in Figure 7 with basal spacing. $C_{11}$, $C_{22}$, and $C_{12}$ all decrease nonlinearly with the increase of water content. These components are mainly controlled by the ionic or covalent bonding strength of mineral atoms and the geometric conformation of the hydrated MMT system. In addition, the simulation results of $C_{11}$ and $C_{12}$ are in good agreement with those of [29], but $C_{12}$ is slightly lower. The reason may lie in the difference between our simulation structure and the octahedral isomorphic substitutions of [29]. However, the measured range of UPV given by [17] ($C_{11}$ = 13.8~46.1 GPa and $C_{12}$ = 6.9~17.8 GPa) is much lower than the simulated results. This is because the MMT mineral lamellae are very thin, and the relative slip between lamellae easily occurs in the UPV test. However, the simulated results in [25] ($C_{11}$ = 189~231 GPa) and test results by Brillouin scattering on mica minerals in [26] ($C_{11}$ = 181 GPa and $C_{22}$ = 178 GPa) both show that the results of this study are credible.

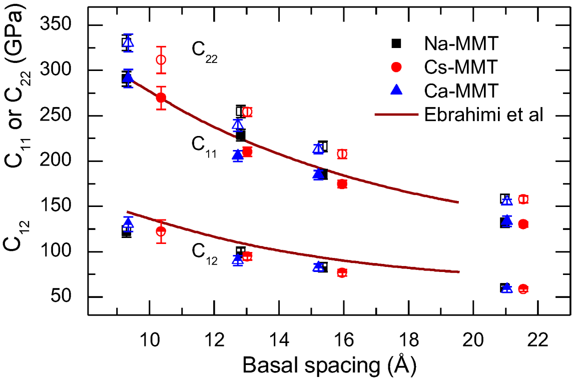

**Figure 7.** The $C_{11}$, $C_{22}$, and $C_{12}$ elastic constants as a function of basal layer spacing.

For the shear of clay under high pressure, the most concerned is the shear resistance of limited interlayer water molecules in the hydrated MMT system, i.e., the in-plane shear stiffness tensor components $C_{44}$ and $C_{55}$. Their variations with basal spacing are shown in Figure 8; $C_{44}$ and $C_{55}$ fluctuate with the increase of water content which is like the variation of $C_{33}$. Therefore, the mechanism of shear strength of interlayer water is closely related to the formation of H-bonds and atom-free volume. The shear strength between dry MMT lamellae is much larger than that of hydrated MMT lamellae, that is to say, the addition of water plays a lubricating role in interlayer friction, which makes $C_{44}$ and $C_{55}$ decrease sharply. However, these limited interlayer water molecules do not completely show the zero shear strength characteristics of free water. As water content increases, the in-plane shear strength increases to a local maximum when the system approaches the thermodynamic stable state and minimum atom free volume occurs. In the range of simulated water content, $C_{44}$ and $C_{55}$ eventually tend to be constant. Furthermore, the results in Figure 8 shows that the components $C_{44}$ and $C_{55}$ are in good agreement with those obtained by [29], and the in-plane shear strength between different MMT systems is close except for the dry MMT system. Meanwhile, the simulated results also fall well into the UPV measurement range of [17] ($C_{44}$ = 2.9~8.9 GPa).

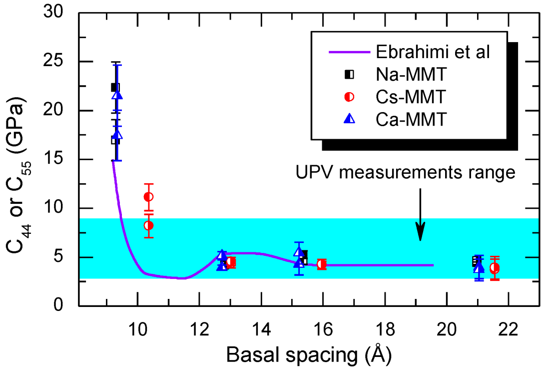

**Figure 8.** The $C_{44}$ and $C_{55}$ elastic constants as a function of basal layer spacing.

The shear of hydrated MMT along the direction perpendicular to the mineral plane is mainly controlled by the relative torsion of bonded atoms. The variations of $C_{66}$ with basal spacing are shown in Figure 9. With the increase of interlayer water content, $C_{66}$ decreases continuously, which is mainly due to the increase of interlayer water contribution in the weak shear zone. Considering that the ratio of width to height of a true MMT lamella is very large (about 100:1 to 1000:1), shear along the direction of orthogonal to the mineral plane is almost impossible, so the variations of $C_{66}$ will not be discussed here.

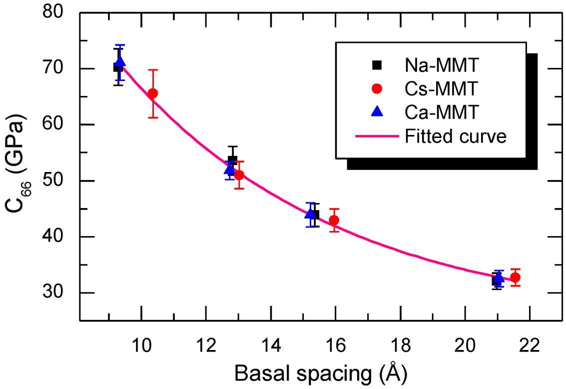

**Figure 9.** The $C_{66}$ elastic constant as a function of basal layer spacing.

Young's moduli of the different MMT systems under various hydration can be obtained by further conversion of the stiffness tensor, and the variation of Young's moduli with basal spacing is shown in Figure 10. The in-plane Young's moduli $E_1$ and $E_2$ are consistent with $C_{11}$ and $C_{12}$ that decrease nonlinearly with the increase of water content. For the Young's modulus of $E_3$ which is perpendicular to the mineral plane, its value for the dry MMT system is 2–3 times that of the hydrated system for Na-MMT and Ca-MMT. $E_3$ of the hydrated MMT system also decreases nonlinearly with the increase of water content. Interestingly, for Cs-MMT, the Young's modulus, $E_3$, of different hydrated MMT systems, even dry MMT systems, is almost the same. Preliminary analysis shows that this may be related to the larger radius of $Cs^+$ ions. For the dry MMT system, the interlayer spacing is large, which induces a low compression strength. After hydration, the $Cs^+$ ions always form an inner-sphere complex, which has little effect on the strength, thus making all Cs-MMT systems of $E_3$ almost the same within the range of simulated water content. However, this interesting phenomenon has not yet been reported in the literature, so the above corollary needs further study in the future.

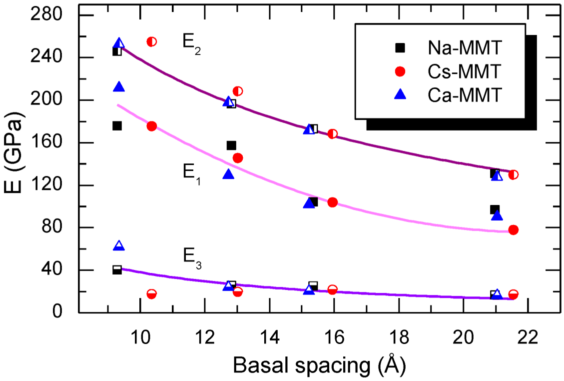

**Figure 10.** Young modulus as a function of basal layer spacing.

From the above comparisons, molecular microscopic testing techniques, such as UPV, can only qualitatively analyze the strength of clay minerals and the test results are not accurate enough. Molecular dynamics simulation provides a good way to understand the properties of hydrated clay minerals on an atomic scale. In particular, unconstrained system techniques and thermodynamic stable-state water content analysis techniques are used to make the calculation results of molecular dynamics more reliable.

## 4. Conclusions

Molecular dynamic simulations were conducted to investigate the mechanical properties of montmorillonite with different compensation cations upon hydration with unconstrained system atoms, expanding further studies of nanoscale elastic properties. The conclusions are as follows:

(1) The basal spacing of all MMT systems increases from step to step in the initial crystalline swelling stage. While this step characteristic (plateau) disappears, the basal spacing shows approximately linear variation in the subsequent osmotic swelling stage. However, the quantitative values of the basal spacing for different compensation cationic MMTs are different, which is related to the ion radius of cations.

(2) The nanoscale elastic properties of hydrated MMT show obvious anisotropy. The tensile and compressive strength ($\sigma_3$) of MMT orthogonal to the mineral plane is much lower than the in-plane strengths ($\sigma_1$ and $\sigma_2$), and the hydration molecular layer mixed within MMT lamellae has certain shear strengths ($\tau_4$ and $\tau_5$). The order of strength values from large to small is the compressive strength, the tensile strength, and the shear strength, respectively.

(3) The components of $C_{33}$, $C_{44}$, and $C_{55}$ all fluctuate with the increase of interlayer water content, while the variation of the in-plane stiffness tensor components $C_{11}$, $C_{22}$, and $C_{12}$, all decrease nonlinearly with the increase of water content. These components are mainly controlled by the bonding strength of mineral atoms and the geometric conformation of the hydrated MMT system. The $C_{66}$ component reflects the shear of hydrated MMT along the direction perpendicular to the mineral plane, which is mainly controlled by the relative torsion of bonded atoms. Due to the increase of interlayer water contribution in the weak shear zone, $C_{66}$ decreases continuously with the increase of interlayer water content. Young's moduli all decrease nonlinearly with the increase of water content.

The simulation results reveal that the water molecules linked to the mineral surface will be arranged in an ordered structure (H-bond formation and thermodynamic dense stable state) and their shear strength are not zero. Preliminary discussion shows that this is related to the strength mechanism of clay at the microscale. Building a bottom-up procedure toward a constitutive law for soil mechanical still needs further research.

**Author Contributions:** Conceptualization, L.K. and Q.Z.; Methodology, X.S.; Validation, X.Z.; Formal analysis, L.K.; investigation, Q.Z.; writing—original draft preparation, L.K Writing-Original Draft Preparation, L.K.; Writing—review and editing, Q.Z. and X.Z.; Visualization, X.S.; Supervision, Q.Z. All authors have read and agreed to the published version of the manuscript.

**Funding:** This research was funded by the Fundamental Research Funds for the Central Universities, grant number 2020ZDPYMS18.

**Institutional Review Board Statement:** Not applicable.

**Informed Consent Statement:** Not applicable.

**Data Availability Statement:** The data presented in this study are available on request from the corresponding author.

**Acknowledgments:** The study presented in this article was supported by the Fundamental Research Funds for the Central Universities (2020ZDPYMS18). This support is gratefully acknowledged.

**Conflicts of Interest:** The authors declare no conflict of interest.

## References

1. Sposito, G. *The Chemistry of Soils*, 2nd ed.; Oxford University Press, Inc.: Cary, NC, USA, 2008.
2. Bai, B.; Yang, G.C.; Li, T.; Yang, G.S. A thermodynamic constitutive model with temperature effect based on particle rearrangement for geomaterials. *Mech. Mater.* **2019**, *139*, 10318. [CrossRef]
3. Frenkel, D.; Smit, B. *Understanding Molecular Simulation*, 2nd ed.; Academin Press: San Diego, CA, USA, 2002.
4. Bai, B.; Rao, D.Y.; Chang, T.; Guo, Z.G. A nonlinear attachment-detachment model with adsorption hysteresis for suspension-colloidal transport in porous media. *J. Hydrol.* **2019**, *578*, 124080. [CrossRef]
5. Gilmour, K.A.; Davie, C.T.; Gray, N. An indigenous iron-reducing microbial community from MX80 bentonite—A study in the framework of nuclear waste disposal. *Appl. Clay Sci.* **2021**, *205*, 106039. [CrossRef]
6. Xu, H.; Zheng, L.G.; Rutqvist, J.; Birkholzer, J. Numerical study of the chemo-mechanical behavior of FEBEX bentonite in nuclear waste disposal based on the Barcelona expansive model. *Comput. Geotech.* **2021**, *132*, 103968. [CrossRef]
7. Wu, P.X.; Tang, Y.N.; Wang, W.M.; Zhu, E.W.; Li, P.; Wu, J.H.; Dang, Z.; Wang, X.D. Effect of dissolved organic matter from Guangzhou landfill leachate on sorption of phenanthrene by Montmorillonite. *J. Colloid Interf. Sci.* **2011**, *361*, 618–627. [CrossRef]
8. Ray, S.; Mishra, A.K.; Kalamdhad, A.S. Hydraulic performance, consolidation characteristics and shear strength analysis of bentonites in the presence of fly-ash, sewage sludge and paper-mill leachates for landfill application. *J. Environ. Manag.* **2022**, *302*, 113977. [CrossRef]
9. Bai, B.; Zhou, R.; Cai, G.Q.; Hu, W.; Yang, G.C. Coupled thermo-hydro-mechanical mechanism in view of the soil particle rearrangement of granular thermodynamics. *Comput. Geotech.* **2021**, *137*, 104272. [CrossRef]
10. Bai, B.; Nie, Q.K.; Zhang, Y.K.; Wang, X.L.; Hu, W. Cotransport of heavy metals and $SiO_2$ particles at different temperatures by seepage. *J. Hydrol.* **2021**, *597*, 125771. [CrossRef]
11. Zhu, B.; Wang, Y.M.; Liu, H.; Ying, J.; Liu, C.T.; Shen, C.Y. Effects of interface interaction and microphase dispersion on the mechanical properties of PCL/PLA/MMT nanocomposites visualized by nanomechanical mapping. *Compos. Sci. Technol.* **2020**, *190*, 108048. [CrossRef]
12. Shang, X.Y.; Zhou, G.Q.; Kuang, L.F.; Cai, W. Compressibility of deep clay in East China subjected to a wide range of consolidation stresses. *Can. Geotech. J.* **2015**, *52*, 244–250. [CrossRef]
13. Prasad, M.; Kopycinska, M.; Rabe, U.; Arnold, W. Measurement of Young's modulus of clay minerals using atomic force acoustic microscopy. *Geophys. Res. Lett.* **2002**, *29*, 1172. [CrossRef]
14. Vanorio, T.; Prasad, M.; Nur, A. Elastic properties of dry clay mineral aggregates, suspensions and sandstones. *Geophys. J. Int.* **2003**, *155*, 319–326. [CrossRef]
15. Kopycinska-Müller, M.; Prasad, M.; Rabe, U.; Arnold, W. Elastic properties of clay minerals determined by atomic force acoustic microscopy technique. *Acoust. Imaging* **2007**, *28*, 409–416.
16. Yang, C.; Xiong, Y.Q.; Wang, J.F.; Li, Y.; Jiang, W.M. Mechanical characterization of shale matrix minerals using phase-positioned nanoindentation and nano-dynamic mechanical analysis. *Int. J. Coal Geol.* **2020**, *229*, 103571. [CrossRef]
17. Ortega, J.A. Micropormechanical Modeling of Shale. Ph.D. Thesis, Massachusetts Institute of Technology, Cambridge, MA, USA, 2010.

18. Seo, Y.S.; Ichikawa, Y.; Kawamura, K. Stress-strain response of rock-forming minerals by molecular dynamics simulation. *Mater. Sci. Res. Int.* **1999**, *5*, 13–20. [CrossRef]
19. Mitchell, J.K.; Soga, K. *Fundamentals of Soil Behavior*, 3rd ed.; John Wiley & Sons, Inc.: Hoboken, NJ, USA, 2005.
20. Mao, H.; Huang, Y.; Luo, J.Z.; Zhang, M.S. Molecular simulation of polyether amines intercalation into Na-montmorillonite interlayer as clay-swelling inhibitors. *Appl. Clay Sci.* **2021**, *202*, 105991. [CrossRef]
21. Wei, P.C.; Zhang, L.L.; Zheng, Y.Y.; Diao, Q.F.; Zhuang, D.Y.; Yin, Z.Y. Nanoscale friction characteristics of hydrated montmorillonites using molecular dynamics. *Appl. Clay Sci.* **2021**, *210*, 106155. [CrossRef]
22. Sato, H.; Yamagishi, A.; Kawamura, K. Molecular simulation for flexibility of a single clay layer. *J. Phys. Chem. B* **2001**, *105*, 7990–7997. [CrossRef]
23. Manevitch, O.L.; Rutledge, G.C. Elastic properties of a single lamella of montmorillonite by molecular dynamics simulation. *J. Phys. Chem. B* **2004**, *108*, 1428–1435. [CrossRef]
24. Chen, B.Q.; Evans, J.R.G. Elastic moduli of clay platelets. *Scr. Mater.* **2006**, *54*, 1581–1585. [CrossRef]
25. Mazo, M.A.; Manevich, L.I.; Balabaev, N.K. Molecular dynamics simulation of thermo-mechanical properties of montmorillonite crystal. *Nanotechnol. Russ.* **2009**, *4*, 676–699. [CrossRef]
26. Zartman, G.D.; Liu, H.; Akdim, B.; Pachter, R.; Heinz, H. Nanoscale tensile, shear, and failure properties of layered silicates as a function of cation density and stress. *J. Phys Chem. C* **2010**, *114*, 1763–1772. [CrossRef]
27. Fu, Y.T.; Zartman, G.D.; Yoonessi, M.; Drummy, L.F.; Heinz, H. Bending of layered silicates on the nanometer scale: Mechanism, stored energy, and curvature limits. *J. Phys Chem. C* **2011**, *115*, 22292–22300. [CrossRef]
28. Teich-McGoldrick, S.L.; Greathouse, J.A.; Cygan, R.T. Molecular dynamics simulations of structural and mechanical properties of muscovite: Pressure and temperature effects. *J. Phys Chem. C* **2012**, *116*, 15099–15107. [CrossRef]
29. Ebrahimi, D.; Pellenq, R.J.-M.; Whittle, A.J. Nanoscale elastic properties of montmorillonite upon water adsorption. *Langmuir* **2012**, *28*, 16855–16863. [CrossRef] [PubMed]
30. Carrier, B.; Vandamme, M.; Pellenq, R.J.-M.; van Damme, H. Elastic properties of swelling clay particles at finite temperature upon hydration. *J. Phys Chem. C* **2014**, *118*, 8933–8943. [CrossRef]
31. Zheng, Y.; Zaoui, A. Mechanical behavior in hydrated Na-montmorillonite clay. *Phys. A* **2018**, *505*, 582–590. [CrossRef]
32. Zhu, L.P.; Shens, W.Q.; Shao, J.F.; He, M.C. Insight of molecular simulation to better assess deformation and failure of clay-rich rocks in compression and extension. *Int. J. Rock Mech. Min.* **2021**, *138*, 104589. [CrossRef]
33. Schmidt, S.R.; Katti, D.R.; Ghosh, P.; Katti, K.S. Evolution of mechanical response of sodium montmorillonite interlayer with increasing hydration by molecular dynamics. *Langmuir* **2005**, *21*, 8069–8076. [CrossRef]
34. Suter, J.L.; Coveney, P.V.; Greenwell, H.C.; Thyveetil, M.A. Large-scale molecular dynamics study of montmorillonite clay: Emergence of undulatory fluctuations and determination of material properties. *J. Phys. Chem. C* **2007**, *111*, 8248–8259. [CrossRef]
35. Liu, X.D.; Lu, X.C.; Wang, R.C.; Zhou, H.Q. Effects of layer-charge distribution on the thermodynamic and microscopic properties of Cs-smectite. *Geochim. Et Cosmochim. Acta* **2008**, *72*, 1837–1847. [CrossRef]
36. Cygan, R.T.; Liang, J.J.; Kalinichev, A.G. Molecular models of hydroxide, oxyhydroxide, and clay phases and the development of a general force field. *J. Phys. Chem. B* **2004**, *108*, 1255–1266. [CrossRef]

applied sciences

MDPI

*Article*

# Experimental Study on Microstructure of Unsaturated Expansive Soil Improved by MICP Method

**Xinpei Yu [1], Hongbin Xiao [1,*], Zhenyu Li [1], Junfeng Qian [2], Shenping Luo [1] and Huanyu Su [1]**

[1] School of Civil Engineering, Central South University of Forestry and Technology, Changsha 410018, China; 20191100320@csuft.edu.cn (X.Y.); 13787024735hdlizhenyu@163.com (Z.L.); 20191100323@csuft.edu.cn (S.L.); 20201100370@csuft.edu.cn (H.S.)

[2] Department of Civil Engineering, Monash University, Clayton, VIC 3800, Australia; junfeng.qian@monash.edu

* Correspondence: t20090169@csuft.edu.cn; Tel.: +86-135-7482-6532

**Abstract:** The soil water characteristic curve and microstructure evolution of unsaturated expansive soil improved by microorganisms in Nanning, Guangxi were studied by means of filter paper method and scanning electron microscope imaging (SEM). Based on Fredlung & Xing model, the influence law of different cement content on the soil water characteristic curve of improved expansive soil is proved. According to the analysis of SEM test results, the influence mechanism of MICP method on the engineering characteristics of improved expansive soil is revealed. The results show that with the increase of cement content, the saturated water content and residual water content of the improved expansive soil gradually increased. At the same time, the water stability gradually increased while the air inlet value gradually decreased. The improved expansive soil changes from the superposition of flat particles and flake particles to the contact between spherical particles and flake particles, which indicates that the aggregate increases significantly. With the increase of the content of cement solution, the contact between particles tends to be smooth and the soil pores gradually tend to be evenly distributed. The particle size and microstructure of soil particles was changed and the connection between particles was enhanced in the improved expansive soil. Eventually the strength and water stability of expansive soil were improved. The conclusions above not only provide a theoretical basis for the in-depth study of engineering characteristics of unsaturated expansive soil improved by MICP method, but also offer theoretical evidence for perfecting engineering technology of expansive soil improved by MICP method.

**Keywords:** microbially induced carbonate precipitation (MICP); unsaturated soil; soil-water characteristic curves; matrix suction; microstructure

**Citation:** Yu, X.; Xiao, H.; Li, Z.; Qian, J.; Luo, S.; Su, H. Experimental Study on Microstructure of Unsaturated Expansive Soil Improved by MICP Method. *Appl. Sci.* **2022**, *12*, 342. https://doi.org/10.3390/app12010342

Academic Editor: Bing Bai

Received: 7 December 2021
Accepted: 23 December 2021
Published: 30 December 2021

**Publisher's Note:** MDPI stays neutral with regard to jurisdictional claims in published maps and institutional affiliations.

**Copyright:** © 2021 by the authors. Licensee MDPI, Basel, Switzerland. This article is an open access article distributed under the terms and conditions of the Creative Commons Attribution (CC BY) license (https://creativecommons.org/licenses/by/4.0/).

## 1. Introduction

Expansive soil is special catastrophic clay composed of strong hydrophilic minerals such as montmorillonite, illite, and kaolinite, which usually exhibit significant overconsolidation, multiple fissures, and swell-shrink characteristics. Expansive soils are distributed in a wide range in China and exist to varying degrees in more than 20 provinces such as Guangxi, Yunnan, and Sichuan. After expansive soil is exposed to water, it is highly susceptible to swelling deformation, softening and strength decay, and dry shrinkage cracks when water is lost. This repeated expansion and contraction deformation will lead to crack, subgrade uplift and slope sliding which will cause major engineering disasters [1–3]. Therefore, any construction work in expansive soil area must be treated and improved to eliminate potential engineering hazards. Traditional methods widely used in engineering for improving expansive soils are usually divided into physical and chemical improvement methods [4,5]. These methods of improving expansive soil could reduce expansive soil's swell-shrink characteristic effectively and also improve its strength. However, the traditional methods of improvement are not only labor-intensive and time-consuming, but also pollute the surrounding environment, and may even have negative impacts on the long-term ecosystem. Therefore, the academic and engineering circles urgently need a new, sustainable, and environmentally friendly alternative method to improve the poor engineering properties of expansive soil.

With the interpenetration of modern biotechnology and engineering science, biogeotechnical engineering has become a new and hot research field. In recent decades, the Microbially Induced Carbonate Precipitation (MICP) method was used by scholars at home and abroad to repair fractures, seepage control, sand consolidation and soft soil improvement with good results [6–9]. In terms of applying the MICP method to improve the engineering characteristics of soft soils, scholars from home and abroad have mainly researched in improving sandy soils and made great progress [10–14]. In recent years, a few scholars have used the MICP method to improve expansive soil and other soft clays, which has made gratifying research progress. Bai studied the coupled migration of ions in soil [15]. Liu demonstrated that the MICP method can effectively improve the strength of loess through unconfined compressive strength test, calcium carbonate content test and scanning electron microscope test, and found the optimal reaction conditions and cementation liquid content for the improvement [16]. Safdar and Gowthaman studied the MICP method for improving peat soils. It was found that *Bacillus licheniformis* was more effective in improving peat soils, and that scallop powder was effective in increasing the activity of microorganisms and promoting the cementation of peat soil particles [17,18]. Some scholars investigated the swelling properties, strength properties, and microstructure of MICP modified expansive soils through a series of tests such as one-dimensional swelling tests, tensile tests, consolidation tests and compression tests. The MICP method of improved expansive soils can control the swelling and shrinking characteristics of the soil and improve the strength of the soil, and the calcite produced by the reaction can also provide a linkage to the soil particles [19–21]. Expansive soil in nature is usually unsaturated. Based on the theory of unsaturated soil mechanics, scholars carried out research on the engineering properties of unsaturated soil [22–26]. Soil-water Characteristic Curves (SWCC) obtained from unsaturated soil tests can be used to study the hydrophilicity, swell-shrinkage and strength characteristics of expansive soil improved by the MICP method.

In this paper, a series of experimental studies were carried out on expansive soil improved by the MICP method using the filter paper method. The SWCC of the expansive soil was measured after the improvement of different solutions with different cementation liquid content. The relationship between the moisture content of the expansive soil and the matric suction was obtained. Following comparison of four empirical models, Fredlund & Xing model was chosen to analyze the SWCC of the expansive soil after improvement by different schemes. The air entry value and water stability of the expansive soil were obtained.

The particle shape and pore space changes in the improved expansive soil were gotten by Scanning Electron Microscope (SEM) tests. From the perspective of microstructural changes in soil samples, the mechanism of the effect of different cementation liquid content on the water stability and water sensitivity of improved expansive soil during the MICP process was revealed.

## 2. SWCC Test Materials and Methods

### 2.1. Test Materials

The expansive soil used in the study was taken from Nanning, Guangxi, and was off-white. The particle size distribution of the unimproved expansive soil was obtained by taking the expansive soil for particle analysis tests. The particle size distribution of the expansive soils, as shown in Table 1.

**Table 1.** Particle size distribution of expansive soil.

| ≤0.005 | (0.005,0.075] | (0.075,0.025] | (0.025,0.5] | (0.5,2] | (2,20) |
|---|---|---|---|---|---|
| 15.4 | 62.9 | 7.1 | 6.9 | 5.2 | 2.6 |

The obtained expansive soil was dried, crushed, adopted 2 mm sieve and a portion of the particles less than 2 mm in diameter was taken for testing. The basic physical properties of the expansive soil were obtained from the tests and are shown in Table 2.

**Table 2.** Indicators of physical property of expansive soil.

| Liquid Limit (%) | Plastic Limit (%) | Plastic Index (%) | Natural Moisture Content (%) | Optimal Moisture Content (%) | Maximum Dry Density (%) |
|---|---|---|---|---|---|
| 58.1 | 22.3 | 35.8 | 21.8 | 23.3 | 1.75 |

## *2.2. Sample Preparation of MICP Improved Expansive Soil*

### 2.2.1. Bacteria and Culture Media

The microorganism used to improve the expansive soil was *Bacillus pasteurii*, purchased from the Chinese General Microbial Strain Collection (CGMCC) under the number ATCC11859. This strain is a nonpathogenic, Gram-positive bacteria, which has no adverse effects on humans or the biological environment, a good ability to secrete urease. and is present in natural soil [27]. The *Bacillus pasteurii* used for the test is shown in Figure 1. The culture medium consisted of 20 g/L urea, 20 g/L agar, 15 g/L casein peptone, 5 g/L soy peptone and 5 g/L sodium chloride. *Bacillus pasteurii* was inoculated in a slant medium and incubated at 30 °C for 24 h and stored at 4 °C. The culture was inserted into an agar-free medium and incubated for 36–48 h in a constant temperature shaking incubator at a temperature of 30 °C and a speed of 150 r/min. The absorbance $OD_{600}$ value of the bacterial liquid at a wavelength of 600 nm was measured using a spectrophotometer. When the $OD_{600}\approx 1.6$, the bacterial solution is used to improve the expansive soil.

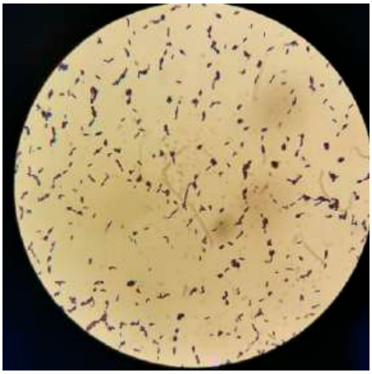

**Figure 1.** *Bacillus pasteurii* used in testing.

### 2.2.2. Preparation of Cementation Liquid

The cementation liquid is a source of calcium for the MICP process and provides the raw material and hydrolytic environment for the metabolic processes of the microorganisms. Based on the chemical reaction equation for the MICP process, it can be calculated that for every molecule of calcium carbonate produced, 1 molecule of calcium chloride and 1 molecule of urea are required [28]. Therefore, the ratio of calcium chloride to urea in the cementation liquid was determined to be 1:1 and the concentration of the cementation liquid was 1 mol/L. Each 100 mL of cementation liquid contained 21.91 g of $CaCl_2 \cdot 6H_2O$ and contained 6.01 g of urea.

### 2.2.3. Preparation of Soil Samples

The soil samples used in the test were divided into four groups, one of which was an unimproved expansive soil as a control group and the other three groups were samples that had been improved using the MICP method. Due to the high liquid limit and low permeability of expansive soil, conventional grouting and soaking methods cannot be used to improve expansive soil by the MICP method. In the tests, the expansive soil was amended by spraying and then mixing. The unimproved expansive soil was mixed with the cementation liquid and the bacterial fluid, respectively, and then kept in a constant temperature and humidity biochemistry cultivation cabinet at 30 °C for 14 days. During the curing process, holes need to be poked in the plastic film to provide the aerobic environment for bacterial metabolism to survive.

### *2.3. Test Scheme and Procedure*

Four sets of tests were set up to investigate the effect of cementation liquid content on the SWCC of expansive soil during MICP. In addition to one group of unimproved expansive soil samples, three other groups of expansive soil samples were successively improved with cementation liquid and bacterial liquid. The improved soil samples were dehumidified and absorbed after 14 days of curing and weighed regularly to make sure they reached the moisture content required for the experimental design. The maximum dry density $\rho_{dm}$ of the expansive soil is taken as the dry density of the specimen and the degree of compaction is 90%. Calculated the mass of loose soil required for the sample and made it into a ring-knife sample of size 61.8 × 20 mm. Based on relevant studies by Jiang [19] and Li [20] on the microbiological improvement of expansive soil, the admixture of cementation liquid and bacterial liquid in the experimental scheme was designed [19]. In the three groups of improved expansive soil samples, the content of cementation liquid was 100, 125, and 150 mL respectively, and the content of bacterial liquid was 50 mL. The test scheme for the MICP method of improving expansive soil is shown in Table 3.

**Table 3.** Test scheme of improved expansive soil by MICP method.

| Total Sample | Sample Number | Bacterial Liquid Content (mL) | Cementation Liquid Content (mL) | Degree of Compaction (%) |
|---|---|---|---|---|
| 112 | A1, A2, A3 | 50 | 100, 125, 150 | 90 |

Dried filter paper ("Double Circle" brand, No. 203) is placed between two soil samples and three layers of filter paper are placed in each set of samples. The top and bottom layers are qualitative filter paper with a diameter of 60 mm and the middle layer is quantitative filter paper with a diameter of 50 mm. Use electrical insulation tape to seal the contact surface of the two ring knives, then wrap the test sample in plastic film and then wrap the plastic film tightly with electrical insulation tape. The wrapped samples are placed in the basin, sealed twice using plastic film and placed in a 20 °C thermostat. After 7 days, moisture equilibrium is reached between the filter paper and the expansive soil, at which point the matric suction of the filter paper and the expansive soil can be considered equal. The middle layer of the filter paper is removed with forceps and the mass of the wet filter paper is quickly weighed and recorded.

The test needs to be conducted under three assumptions. Firstly, it was assumed that *Bacillus pasteurii* with consistent absorbance would have the same activity and produce the same urease activity. Secondly, it is assumed that the expansive soils are well mixed during the treatment of the MICP method. Thirdly, it is assumed that the resting specimen is completely sealed during the filter paper method of testing. To ensure the reliability of the test results and to minimize errors arising during the test, a control group was designed in the experimental study. Measure the matric suction, as shown in Figure 2.

(**a**) (**b**)

**Figure 2.** Measurement for matrix suction: (**a**) sealed storage; (**b**) dried filter paper.

According to the study of the calibration curve of the "double circle" brand filter paper by Bai Fuqing [29] and Zhang Hua [30], the matric suction of the soil sample is determined by using the calibration formula. The calibration result of matrix suction, as shown in Equation (1).

$$\begin{cases} \lg(S_m) = -0.0767\theta_e + 5.493 & \theta_e \leq 47\% \\ \lg(S_m) = -0.0120\theta_e + 2.470 & \theta_e > 47\% \end{cases} \quad (1)$$

where $S_m$ represents the matrix suction, and $\theta_e$ represents the moisture content of the filter paper after equilibrium.

## 3. Results and Analysis of SWCC Test

### *3.1. Selection of the SWCC Fitting Model*

To facilitate the analysis of the test data, empirical models of SWCC were used to fit the test results. Commonly used SWCC models include the Van Genuchten model (VG model) [31,32], the Gardner model [33] and the Fredlund & Xing model [34]. Among them, the VG model is in two- and three-parameter forms, and the commonly used empirical model equations are as follows.

$$\theta = \theta_r + \frac{\theta_s - \theta_r}{\left[1 + (\alpha\varphi)^n\right]^{\left(1-\frac{1}{n}\right)}} \quad (2)$$

$$\theta = \theta_r + \frac{\theta_s - \theta_r}{\left[1 + (\alpha\varphi)^n\right]^{(m)}} \quad (3)$$

$$\theta = \theta_r + \frac{\theta_s - \theta_r}{1 + \left(\frac{\varphi}{\alpha}\right)^n} \quad (4)$$

$$\theta = \theta_r + \frac{\theta_s - \theta_r}{\left\{ In\left[e + \left(\frac{\varphi}{\alpha}\right)^n\right]\right\}^m} \quad (5)$$

where $\theta$ represents the soil volumetric moisture content, $\theta_s$ represents the saturated volumetric moisture content, $\theta_r$ represents the residual volumetric moisture content, $e$ represents the base of the natural logarithm and $e \approx 2.71$, $\varphi$ represents the matric suction, $\alpha$, $n$, $m$ all represents the fitted parameters.

The four models mentioned above were used to fit the test results of the expansive soils after improvement with different cementation liquid contents. The SWCC was obtained for the improved expansive soils with different fitting models, as shown in Figure 3.

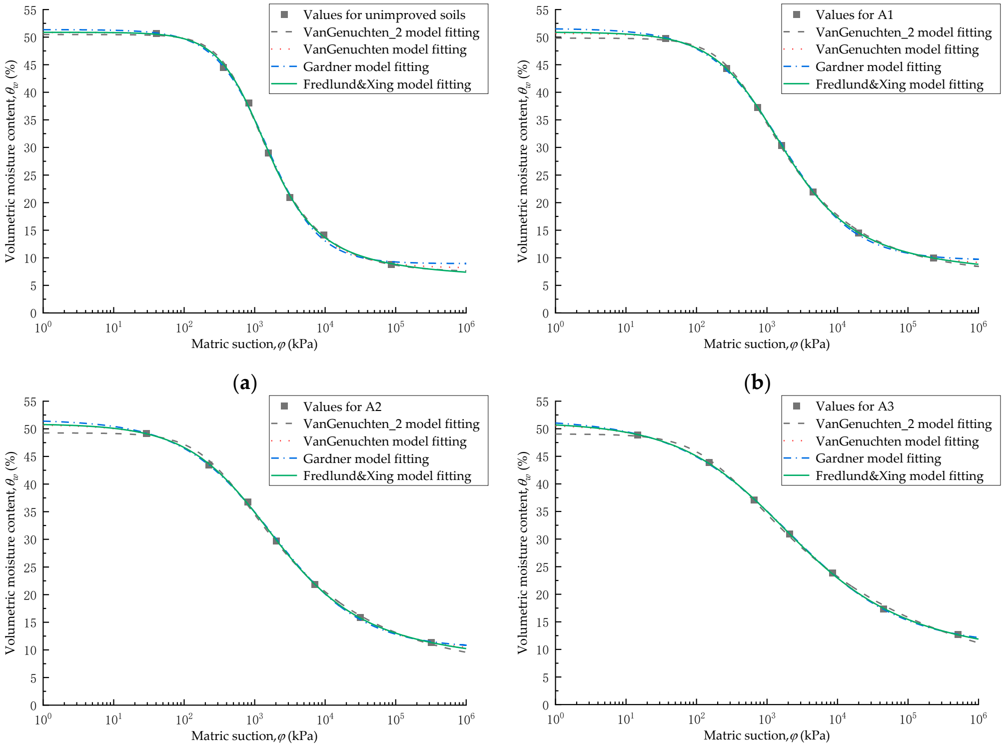

(**a**) (**b**)

(**c**) (**d**)

**Figure 3.** Soil-water characteristic curves obtained by model fitting: (**a**) fitted curve for unimproved expansive soil; (**b**) A1 fitted curve; (**c**) A2 fitted curve; (**d**) A3 fitted curve.

Figure 3 shows that the SWCC of the expansive soils is anti-"S" shaped after the different solutions. The transition section of SWCC in unimproved expansive soils is relatively steep, the rate of desorption in expansive soils is greater, matrix suction has a greater effect on the volumetric moisture content of the soil and the capacity to hold water is weaker. The transition section of the SWCC of the improved expansive soil tends to flatten out as the admixture of cementation liquid increases, the rate of desorption gradually decreases and the capacity to hold water gradually increases.

The saturated volumetric moisture content and residual volumetric moisture content of the improved expansive soils, and the fitting parameters of the different empirical models, as shown in Table 4.

**Table 4.** $\theta_s$, $\theta_r$, and correlation coefficient of fitting.

| Sample Number | $\theta_s$/% | $\theta_r$/% | Correlation Coefficient $R^2$ | | | |
|---|---|---|---|---|---|---|
| | | | VG_2 Model | VG Model | Gardner Model | F&X Model |
| Unimproved expansive soil | 50.873 | 5.534 | 0.99743 | 0.99708 | 0.99710 | 0.99777 |
| A1 | 50.904 | 5.901 | 0.99887 | 0.99999 | 0.99939 | 0.99999 |
| A2 | 50.919 | 6.225 | 0.99758 | 0.99944 | 0.99932 | 0.99957 |
| A3 | 51.179 | 6.467 | 0.99773 | 0.99980 | 0.99972 | 0.99972 |

From Table 4, the correlation coefficients of the four empirical models fitted above are all more than 0.99 when fitted by the models to the SWCCs of unsaturated expansive soils, indicating that the fitted results are reliable. The fitting of the various models, in descending order, is the Fredlund & Xing model, the three-parameter Van Genuchten model, the Gardner model and the two-parameter Van Genuchten model. The saturated volumetric moisture content of the expansive soil increased from 50.87% to 51.18% with an increase in the admixture of the cementation liquid at the same admixture of the bacterial liquid. Similarly, its residual volumetric moisture content increased from 5.53% to 6.47%. Furthermore, the increasing trend of both saturated and residual volumetric moisture content is non-linear. The Fredlund & Xing model with the optimum fit was selected to investigate the variation of the SWCC parameters of the improved expansive soils, to analyze the SWCC of the expansive soils under different cementation liquid content. It shows that the water-holding capacity of the improved expansive soil is gradually increasing, and the water stability of the soil, which is positively correlated with the water-holding capacity also tends to increase.

### *3.2. Effect of Cementation Liquid Content on SWCC of Soil Samples*

The Fredlund & Xing model was chosen to analyze the test results and the parameters of the model obtained after fitting, as shown in Table 5. As a result, the SWCC of the microbially improved expansive soil can be obtained for different cementation liquid content, as shown in Figure 4.

**Table 5.** Fitting parameters of Fredlund & Xing model.

| Sample Number | $\alpha$ | $n$ | $m$ | Air Entry Value |
|---|---|---|---|---|
| Unimproved expansive soil | 896.997 | 1.356 | 1.418 | 226.948 |
| A1 | 818.070 | 0.959 | 1.424 | 155.666 |
| A2 | 781.332 | 0.762 | 1.420 | 102.804 |
| A3 | 760.739 | 0.585 | 1.462 | 64.240 |

The Fredlund & Xing model assumes that the parameters $\alpha, n$ and $m$ are independent of each other. Where $\alpha$ is the soil parameter associated with the air entry value and can be used to characterize the value of matric suction at the inflection point of the soil-water characteristic curve [35]. As can be seen from Table 5, the air entry values for the expansive soils are 226.948, 155.666, 102.804 and 64.240 kPa from unimproved, A1 and A2 to A3 respectively. The air entry value of the improved expansive soil is significantly lower than that of the unimproved soil, and the air entry value of the improved soil tends to decrease slowly and non-linearly as the content of the cementation liquid increases. The reason for this is that there is a large amount of freedom $Ca^{2+}$ in the cementation liquid, which displaces with the $Na^{+}$ in the expansive soil, reducing the thickness of the electric double layer, increasing the gravitational force between the particles and effectively promoting the coalescence of the particles. At the same time, the coagulation of the soil particles results in a significant reduction in the dispersion of the soil, an increase in the agglomerates and an increase in the porous between the soil particles, which causes a reduction in the air entry value. On the other hand, the larger porous produced by the microbially induced carbonate precipitation, adsorbed on the contact surface between soil particles and the particle surface, effectively enhance the interparticle linkage and reduce the air entry value of the expansive soil [36,37]. $n$ is positively correlated with the slope at the inflection point of the SWCC, which can be used to characterize the water-holding capacity of the soil. The lower the slope at the SWCC inflection point, the better the water holding capacity of the soil [38].

As can be seen from Table 5, the values of the soil parameter $n$ for the improved expansive soils have decreased compared to before the improvement. According to the value of $n$ , the unimproved expansive soil has the weakest water-holding capacity. The value of $n$ in the improved expansive soil decreases gradually from A1, A2 to A3 as the content of cementation liquid in the expansive soil increases under the condition of controlling the content of bacterial liquid of 50 mL.

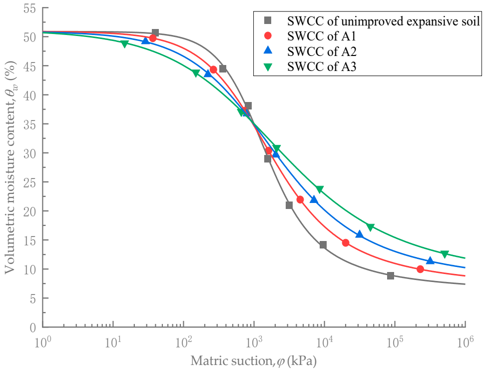

**Figure 4.** SWCCs of expansive soils under different cementing liquid content.

Figure 4 shows that the SWCC intersection of the expansive soils is located near the optimum moisture content under the conditions of the different improvement schemes. When low volumetric moisture content, the greater the content of cementation liquid, the greater the matric suction at the same volumetric moisture content. When the volumetric moisture content is higher than the moisture content at the SWCC intersection, the matric suction of the soil sample decreases with increasing the content of cementation liquid. From unimproved expansive soils to A1, A2, and A3, the SWCC of the expansive soils gradually levelled off, which means that the dehydration rate of the microbiological improved expansive soils gradually decreased, indicating that their water stability was gradually enhanced.

## 4. Microbial Improvement of the Microstructure of Expansive Soils

### *4.1. Scanning Electron Microscope Imaging*

To investigate the microstructural evolution mechanism of the effect of different cementation liquid content on the soil-water characteristics of expansive soils under the same bacterial liquid content conditions. The TESCAN MIRA4 field emission scanning electron microscope was used to image and analyze the expansive soils before and after modification by the MICP method to investigate the changes in particle morphology and porous structure. The sample is an irregular sphere less than 1 cm in diameter and the sample was dried before the test. The surface of the sample is identified as the test surface, which is sprayed with gold to enhance conductivity. Secondary electron imaging was performed using a scanning electron microscope with an electron energy of 10 kev and a magnification of 5 kx.

### *4.2. Analysis of Test Results*

Scanning electron microscope imaging tests were carried out to obtain SEM images of the expanded soil, as shown in Figure 5.

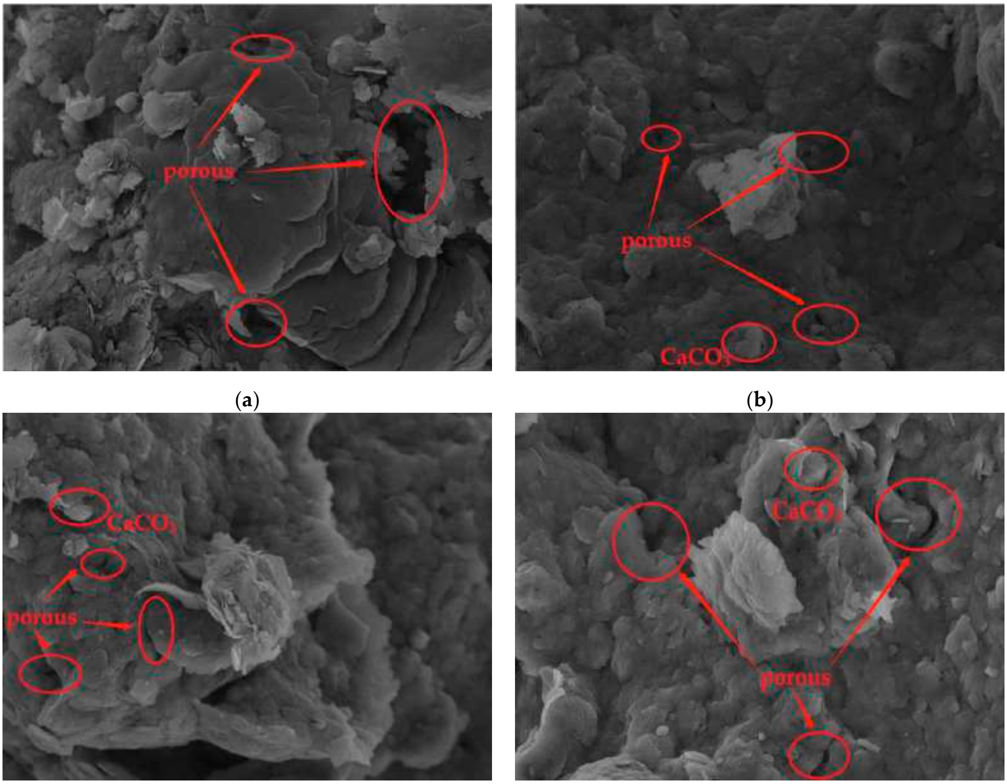

(**a**) (**b**)

(**c**) (**d**)

**Figure 5.** SEM images of expansive soil: (**a**) fitted curve for unimproved expansive soil; (**b**) A1 fitted curve; (**c**) A2 fitted curve; (**d**) A3 fitted curve.

Scanning electron microscope imaging tests were carried out to obtain SEM images of the expansive soil, as shown in Figure 5. The shape of the unimproved expansive soil particles is mainly flat and flake, the particles are mostly in edge-to-face or face-to-face contact, with large variability in pore size. The $CaCO_3$ crystals appeared at the contact points of the expansive soil particles after the MICP improved, and the morphology was mostly spherical particles. The contact between the particles tends to be smooth and the pore size distribution is relatively uniform. In the expansive soil improved by higher cementation liquid content, there are more $CaCO_3$ crystals and larger porous spaces, and the porous spaces are evenly distributed. At low levels of cementation liquid, the expansive soils contain mostly small or medium porous spaces that are uniformly distributed. Li carried out XRD analysis on the improved expansive soils, the study found that the calcite characteristic peaks increased significantly, and the main peak values were enhanced in the expansive soils treated by the MICP method [39]. The calcium carbonate precipitate produced by the test was of a different shape to the typical rhombohedral calcite. This phenomenon might be caused by the shape of the particles being obscured by the soil, or by some bacteria and fine clay particles remaining on the surface of the crystals. Based on the variation of the particle porous structure, a microscopic perspective reveals the internal mechanism by which the air entry value of expansive soils gradually decreases with increasing contents of the cementation liquid. Compared to that of the cohesion of unimproved expansive soils, which are strongly influenced by matric suction and are more water sensitive, matric suction no longer has a restraining effect on the structure after saturation [40]. After improvement by the MICP method, the $CaCO_3$ crystals produced better cementation between the soil particles. The greater the content of the cementation liquid, the more calcium carbonate precipitation is induced and the greater the contact surface of the particles formed, which promotes the agglomeration of the soil particles, and the strength of the expansive soil is improved. Moreover, due to the low solubility of calcium carbonate, it is less affected by water, thus significantly improving the water stability of the expansive soil.

The swelling-shrinkage characteristics of expansive soils in the unsaturated state are mainly related to the water film thickness on the surface of the soil particles when they react with water. The process of water swelling in expansive soils is in essence a process whereby hydrophilic soil particles are wrapped in water molecules under the influence of electric field forces to form a water film. The thickness of the water film gradually increases as the expansive soil absorbs water, resulting in the expansion of the soil particle lattice and the swelling of the soil [41–43]. The unimproved expansive soil particles are mostly in the form of tightly packed or stacked flakes, the lattice can only expand longitudinally outwards when exposed to water. With the increase in the content of the cementation liquid, the flaky particles in the improved expansive soil gradually decrease and the pore space gradually increases. When reacting with water, the lattice of the improved soil particles expands in every direction, balancing the expansion potential in the internal space of the soil before expanding outwards, effectively reducing the expansion deformation of the expansive soil. At the same time, the microbially induced formation of calcium carbonate adheres to the surface of the expansive soil particles, reducing the interaction area between hydrophilic soil particles and water, reducing the water film thickness and interparticle spacing, tightening the soil structure and improving the strength of the soil effectively.

## 5. Conclusions

The SWCC of the expansive soils improved by the MICP method was obtained using the filter paper method under different conditions of cementation liquid content. Based on the theory of unsaturated soil mechanics, the experimental study and theoretical analysis were carried out on the water stability of improved expansive soils. At the same time, scanning electron microscope imaging technology was used to test on expansive soil samples. Based on the analysis of SWCC, the microscopic mechanisms affecting the water sensitivity and strength properties of the improved expansive soil were revealed. The following conclusions were obtained.

(1) The content of the cementation liquid has a significant influence on the SWCC of the expansive soils improved by the MICP method. The saturated and residual water content of the improved expansive soils gradually increases with the content of cementation liquid increased. The air entry value decreases, and the water stability increases gradually.

(2) Scanning electron microscope imaging tests were carried out on the expansive soils before and after improvement. The change of particle morphology and porous structure of the expansive soils under different conditions of cementation liquid content was investigated. The study shows that, compared to that of the unimproved expansive soil, the particle composition of the improved expansive soil evolves from the mutual superposition of flattened and flaky particles to spherical particles in contact with flaky particles, which increased agglomerates significantly. At the same time, with the increase in cementation liquid content, the contact between the particles tends to be smoother and the soil porous tends to be uniformly distributed gradually.

(3) Based on the analysis of macroscopic and microscopic test results, it was found that the mineralization process of microorganisms changed the particle size of soil

particles and the porous structure of the soil. The microscopic mechanism affecting the water stability, swelling and shrinkage characteristics and strength properties of the improved expansive soil were revealed. After the improvement, the calcium carbonate formed by microbial induction precipitates on the surface of the soil particles and in the soil pores, enhancing the interparticle linkage, reducing the hydrophilicity and swelling-shrinkage of the soil, and improving the strength and water stability of the soil. The study also shows that the antierosion ability of the soil is improved significantly due to the increase of aggregates in the soil, the coarsening of the soil particles, and the decreasing water sensitivity of the soil.

The MICP method of improving expansive soils is effective in increasing the strength and water-holding capacity of the soil, but the ammonium ions produced during the reaction can also contaminate the soil [44,45]. The management of ammonium ions in the improvement process is an issue worthy of further study.

**Author Contributions:** Conceptualization, X.Y. and H.X.; methodology, X.Y. and H.X.; software, X.Y. and H.X.; validation, X.Y. and H.X.; formal analysis, X.Y., H.X., Z.L., J.Q., S.L. and H.S.; investigation, X.Y., H.X., Z.L., J.Q., S.L. and H.S.; resources, X.Y. and H.X.; data curation, X.Y. and H.X.; writing—original draft preparation, X.Y. and H.X.; writing—review and editing, X.Y., H.X. and Z.L.; visualization, X.Y., H.X., Z.L., J.Q., S.L. and H.S.; supervision, X.Y., H.X. and Z.L.; project administration, H.X.; funding acquisition, H.X. All authors have read and agreed to the published version of the manuscript.

**Funding:** This research was funded by the National Natural Science Foundation of China, grant number 50978097.

**Institutional Review Board Statement:** Not applicable.

**Informed Consent Statement:** Not applicable.

**Data Availability Statement:** The data presented in this study are available on request from the corresponding author.

**Acknowledgments:** The work described in this paper was supported by a grant from the National Natural Science Foundation of China (Project No. 50978097).

**Conflicts of Interest:** The authors declare no conflict of interest.

## References

1. Xu, Y. Hydraulic Mechanism and Swelling Deformation Theory of Expansive Soils. *Chin. J. Geotech. Eng.* **2020**, *42*, 1979–1987.
2. Ye, Y.; Zou, W.; Han, Z.; Xie, P.; Zhang, J.; Xu, Y. Study on One-dimensional Swelling Characteristics of Expansive Soils Considering the Influence of Initial States. *Chin. J. Geotech. Eng.* **2021**, *43*, 1518–1525.
3. Ning, X.; Xiao, H.; Zhang, C.; He, B.; Xie, J. Study on the Nonlinear Creep Model of Expansive Soil. *J. Nat. Disasters* **2017**, *26*, 149–155.
4. Li, G.; Gong, Q.; Li, T.; Wu, J.; Chen, W.; Cao, X. Experimental Study on Properties of Weak Expansive Soil Improved by Disintegrated Sandstone. *J. Eng. Geol.* **2021**, *29*, 34–43.
5. Chuang, X.; Zhou, M.; Tao, G.; Zhou, R.; Peng, C.; Lin, W. Experimental Study of Dynamic Elastic Modulus and Damping Ratio of Improved Expansive Soil under Cyclic Loading by Expanded Polystyrene. *Rock Soil Mech.* **2021**, *42*, 2427–2436.
6. Bai, B.; Long, F.; Rao, D.; Xu, T. The effect of temperature on the seepage transport of suspended particles in a porous medium. *Hydrol. Processes* **2017**, *31*, 382–393. [CrossRef]
7. He, X.; Liu, H.; Han, F.; Ma, G.; Zhao, C.; Chu, Q.; Xiao, Y. Spatiotemporal Evolution of Microbial-induced Calcium Carbonate Precipitation Based on Microfluidics. *Chin. J. Geotech. Eng.* **2021**, *43*, 1861–1869.
8. Seung, H.C.; Hyeonyong, C.; Kyoungphile, N. Evaluation of Microbially Induced Calcite Precipitation (MICP) Methods on Different Soil Types for Wind Erosion Control. *Environ. Eng. Res.* **2021**, *26*, 123–128.
9. Bai, B.; Nie, Q.Z.; Wang, X.; Hu, W. Cotransport of heavy metals and $SiO_2$ particles at different temperatures by seepage. *J. Hydrol.* **2021**, *597*, 125771. [CrossRef]
10. Zhang, Y.; Wan, X.; Li, N.; Zhao, W.; Chen, J. Analysis of Influencing Factors and Mechanism of Microbial Clay Reinforcement. *J. China Inst. Water Resour. Hydropower Res.* **2021**, *19*, 246–254+261.
11. Li, X.; Wang, S.; He, B.; Shen, T. Permeability Condition of Soil Suitable for MICP Method. *Rock Soil Mech.* **2019**, *40*, 2956–2964.
12. Zhao, C.; Zhang, J.; Zhang, Y.; He, X.; Ma, G.; Liu, H.; Xiao, Y. Research Progress on Multi-scale Biocemented Soil. *J. Beijing Univ. Technol.* **2021**, *47*, 792–801.

13. Xiao, Y.; Wang, Y.; Wang, S.; Evans, T.M.; Stuedlein, A.W.; Chu, J.; Zhao, C.; Wu, H.; Liu, H. Homogeneity and Mechanical Behaviors of Sands Improved by A Temperature-controlled One-phase MICP Method. *Acta Geotech.* **2021**, *2021*, 1417–1427. [CrossRef]
14. Konstantinou, C.; Biscontin, G.; Jiang, N.; Soga, K. Application of Microbially Induced Carbonate Precipitation to Form Bio-cemented Artificial Sandstone. *J. Rock Mech. Geotech. Eng.* **2021**, *13*, 579–592. [CrossRef]
15. Bai, B.; Jiang, S.; Liu, L.; Li, X.; Wu, H. The transport of silica powders and lead ions under unsteady flow and variable injection concentrations. *Powder Technol.* **2021**, *387*, 22–30. [CrossRef]
16. Liu, X.; Fan, J.; Yu, J.; Gao, X. Solidification of Loess Using Microbial Induced Carbonate Precipitation. *J. Mt. Sci.* **2021**, *18*, 265–274. [CrossRef]
17. Safdar, M.U.; Mavroulidou, M.; Gunn, M.J.; Garelick, J.; Payne, I.; Purchase, D. Innovative Methods of Ground Improvement for Railway Embankment Peat Fens Foundation Soil. *Géotechnique* **2021**, *71*, 985–998. [CrossRef]
18. Gowthaman, S.; Chen, M.; Nakashima, K.; Kawasaki, S.; Frontiers, M. Effect of Scallop Powder Addition on MICP Treatment of Amorphous Peat. *Front. Environ. Sci.* **2021**, *9*, 690376. [CrossRef]
19. Jiang, W.; Zhang, C.; Xiao, H.; Luo, S.; Li, Z.; Li, X. Preliminary Study on Microbially Modified Expansive Soil of Embankment. *Geomech. Eng.* **2021**, *26*, 301–310.
20. Li, X.; Zhang, C.; Xiao, H.; Jiang, W.; Qian, J.; Li, Z. Reducing Compressibility of the Expansive Soil by Microbiological-Induced Calcium Carbonate Precipitation. *Adv. Civ. Eng.* **2021**, *2021*, 1–12. [CrossRef]
21. Tiwari, N.; Satyam, N.; Sharma, M. Micro-mechanical Performance Evaluation of Expansive Soil Biotreated with Indigenous Bacteria Using MICP Method. *Sci. Rep.* **2021**, *29*, 1–12. [CrossRef]
22. Abdelbaki, A.M. Assessing the Best Performing Pedotransfer Functions for Predicting the Soil-water Characteristic Curve According to Soil Texture Classes and Matric Potentials. *Eur. J. Soil Sci.* **2021**, *72*, 154–173. [CrossRef]
23. Bai, B.; Xu, T.; Nie, Q.; Li, P. Temperature-driven migration of heavy metal $Pb^{2+}$ along with moisture movement in unsaturated soils. *Int. J. Heat Mass Transf.* **2020**, *153*, 119573. [CrossRef]
24. Bai, B.; Rao, D.; Chang, T.; Guo, Z. A nonlinear attachment-detachment model with adsorption hysteresis for suspension-colloidal transport in porous media. *J. Hydrol.* **2019**, *578*, 124080. [CrossRef]
25. Zhang, G.; Wang, L.; Cao, Z.; Li, Q. Comparative Study of Different Methods for Determining the Soil Water Characteristic Curve Model Considering Uncertainty. *J. Nat. Disasters* **2018**, *27*, 151–158.
26. Fredlund, D.G. State of Practice for Use of the Soil-Water Characteristic Curve (SWCC) in Geotechnical Engineering. *Can. Geotech. J.* **2019**, *56*, 1059–1069. [CrossRef]
27. Sarda, D.; Choonia, H.S.; Sarode, D.D.; Lele, S.S. Biocalcification by *Bsacillus pasteurii* Urease: A Novel Application. *J. Ind. Microbiol. Biotechnol.* **2009**, *36*, 1111–1115. [CrossRef]
28. Pei, D.; Liu, Z.; Hu, B.; Wu, W. Progress on Mineralization Mechanism and Application Research of *Sporosarcina pasteurii*. *Prog. Biochem. Biophys.* **2020**, *47*, 467–482.
29. Bai, F.; Liu, S.; Yuan, J. Measurement of SWCC of Nanyang Expansive Soil Using the Filter Paper Method. *Chin. J. Geotech. Eng.* **2011**, *33*, 928–933.
30. Zhang, H.; Zhang, F.; Yuan, M. Study of Temperature Effect on Domestic Quantitative Filter Paper's Calibration Curves. *Rock Soil Mech.* **2016**, *37*, 274–280.
31. van Genuchten, M.T. A Closed-form Equation for Predicting the Hydraulic Conductivity of Unsaturated Soils. *Soil Sci. Soc. Am. J.* **1980**, *44*, 892–898. [CrossRef]
32. Pan, D.; Ni, W.; Yuan, K.; Zhang, Z.; Wang, X. Determination of Soil-water Characteristic Curve Variables Based on VG Model. *J. Eng. Geol.* **2020**, *28*, 69–76.
33. Gardner, W.R. Some Steady-state Solutions of the Unsaturated Moisture Flow Equation with Application to Evaporation from A Water Table. *Soil Sci.* **1958**, *85*, 228–232. [CrossRef]
34. Fredlund, D.; Xing, A. Equations for the Soil-Water Characteristic Curve. *Can. Geotech. J.* **1994**, *31*, 521–532. [CrossRef]
35. Zhou, B.; Kong, L.; Chen, W.; Bai, H.; Li, X. Analysis of Characteristic Parameters of Soil-water Characteristic Curve (SWCC) and Unsaturated Shear Strength Prediction of Jingmen Expansive Soil. *Chin. J. Rock Mech. Eng.* **2010**, *29*, 1052–1059.
36. Li, C.; Shi, G.; Wu, H.; Wang, C.; Gao, Y. Experimental Study on Bio-mineralization for Dispersed Soil Improvement Based on Enzyme Induced Calcite Precipitate Technology. *Rock Soil Mech.* **2021**, *42*, 333–342.
37. Wang, Z.; Zhang, N.; Cai, G.; Jin, Y.; Ding, N.; Shen, D. Review of Ground Improvement Using Microbial Induced Carbonate Precipitation (MICP). *Mar. Georesour. Geotechnol.* **2017**, *35*, 1135–1146. [CrossRef]
38. Wang, X.; Xu, C.; Wang, S.; Li, X. Study on Overburden Pressure Effect of Expansive Soil-water Characteristic Curve. *Chin. J. Rock Mech. Eng.* **2020**, *39*, 3067–3075.
39. Li, X. Study on Microstrcture and Mechanical Propeities of Expansive Soil Improved by MICP Technology. Ph.D. Thesis, Central South University of Forestry and Technology, Changsha, China.
40. Yao, H.; Liu, S.; Cheng, C. Scopic Essence of Cohesion of a Natural Cemented Soil. *Chin. J. Rock Mech. Eng.* **2001**, *20*, 871–874.
41. Leng, T.; Tang, C.; Xu, D.; Li, Y.; Zhang, Y.; Wang, K.; Shi, B. Advance on the Engineering Geological Characteristics of Expansive Soil. *J. Eng. Geol.* **2018**, *26*, 112–128.
42. Bai, B.; Nie, Q.; Wu, H.; Hou, J. The attachment-detachment mechanism of ionic/nanoscale/microscale substances on quartz sand in water. *Powder Technol.* **2021**, *394*, 1158–1168. [CrossRef]

43. Tan, L. The Effect of Lattice Expansion and Contraction of Montmorillonite on its Volume Change. *Hydrogeol. Eng. Geol.* **1981**, *06*, 5–7+38.
44. Keykha, H.A.; Mohamadzadeh, H.; Asadi, A.; Kawasaki, S. Ammonium-Free Carbonate-Producing Bacteria as an Ecofriendly Soil Biostabilizer. *Geotech. Test. J.* **2019**, *42*, 19–29. [CrossRef]
45. Mohsenzadeh, A.; Aflaki, E.; Gowthaman, S.; Kawasaki, S.; Ebadi, T. A two-stage treatment process for the management of produced ammonium by-products in ureolytic bio-cementation process. *Int. J. Environ. Sci. Technol.* **2021**, *9*, 18313. [CrossRef]

*applied sciences*

*Article*

# Experimental Investigation on the Effects of Ethanol-Enhanced Steam Injection Remediation in Nitrobenzene-Contaminated Heterogeneous Aquifers

**Ruxue Liu [1,2,3], Xinru Yang [1,2,3], Jiayin Xie [1,2,3], Xiaoyu Li [1,2,3] and Yongsheng Zhao [1,2,3,*]**

[1] Key Laboratory of Groundwater Resources and Environment of Ministry of Education, College of New Energy and Environment, Jilin University, Changchun 130021, China; liurx18@mails.jlu.edu.cn (R.L.); xryang19@mails.jlu.edu.cn (X.Y.); xiejy20@mails.jlu.edu.cn (J.X.); xyl21@mails.jlu.edu.cn (X.L.)
[2] Jilin Provincial Key Laboratory of Water Resources and Environment, Jilin University, Changchun 130021, China
[3] National and Local Joint Engineering Laboratory for Petrochemical Contaminated Site Control and Remediation Technology, Jilin University, Changchun 130021, China
[*] Correspondence: zhaoyongsheng@jlu.edu.cn

**Abstract:** Steam injection is an effective technique for the remediation of aquifers polluted with volatile organic compounds. However, the application of steam injection technology requires a judicious selection of stratum media because the remediation effect of hot steam in heterogeneous layers with low permeability is not suitable. In this study, the removal effect of nitrobenzene in an aquifer was investigated through a series of two-dimensional sandbox experiments with different stratigraphic structures. Four types of alcohols were used during steam injection remediation to enhance the removal effect of nitrobenzene (NB)-contaminated heterogeneous aquifers. The principle of the removal mechanism of alcohol-enhanced organic compounds is that alcohols can reduce the surface tension of the contaminated water, resulting in Marangoni convection, thereby enhancing mass and heat transfer. The addition of alcohol may also reduce the azeotropic temperature of the system and enhance the volatility of organic compounds. The study revealed that all four alcohol types could reduce the surface tension from 72 mN/m to <30 mN/m. However, among these, only ethanol reduced the azeotropic temperature of NB by 15 °C, thereby reducing energy consumption and remediation costs. Therefore, ethanol was selected as an enhancing agent to reduce both surface tension and azeotropic temperature during steam injection. In the 2-D simulation tank, the interface between the low-and high-permeability strata in the layered heterogeneous aquifer had a blocking effect on steam transportation, which in turn caused a poor remediation effect in the upper low-permeability stratum. In the lens heterogeneous aquifer, steam flows around the lens, thereby weakening the remediation effect. After adding ethanol to the low-permeability zone, Marangoni convection was enhanced, which further enhanced the mass and heat transfer. In the layered and lens heterogeneous aquifers, the area affected by steam increased by 13% and 14%, respectively. Moreover, the average concentration of NB was reduced by 51% in layered heterogeneous aquifers and by 58% in low-permeability lenses by ethanol addition. These findings enhance the remediation effect of steam injection in heterogeneous porous media and contribute to improve the remediation efficiency of heterogeneous aquifers by steam injection.

**Keywords:** steam injection; ethanol; azeotropic temperature; heterogeneous aquifers; nitrobenzene

**Citation:** Liu, R.; Yang, X.; Xie, J.; Li, X.; Zhao, Y. Experimental Investigation on the Effects of Ethanol-Enhanced Steam Injection Remediation in Nitrobenzene-Contaminated Heterogeneous Aquifers. *Appl. Sci.* **2021**, *11*, 12029. https://doi.org/10.3390/app112412029

Academic Editor: Bing Bai

Received: 1 November 2021
Accepted: 24 November 2021
Published: 17 December 2021

**Publisher's Note:** MDPI stays neutral with regard to jurisdictional claims in published maps and institutional affiliations.

**Copyright:** © 2021 by the authors. Licensee MDPI, Basel, Switzerland. This article is an open access article distributed under the terms and conditions of the Creative Commons Attribution (CC BY) license (https://creativecommons.org/licenses/by/4.0/).

## 1. Introduction

Steam injection is an important remediation technology that can effectively remove organic pollutants during site remediation [1–3]. In particular, steam injection technology can remediate contaminated sites containing multiple volatile or semi-volatile organic pollutants [4]. The remediation efficiency of steam injection technology primarily depends on the permeability of the stratum medium [2,5,6]. The volatility of organic compounds in water is closely related to temperature [7–10]. However, the transmission of steam may be limited by the soil particle size, resulting in a reduction in remediation efficiency [11,12]. In general, the remediation efficiency is the highest in homogeneous sand because of the large particle size and non-layered nature of the soil. Many researchers have used homogeneous sand to analyze the characteristics of steam injection [4,13,14]. However, a heterogeneous stratum structure is quite common at actual remediation sites [15,16]; thus, the impact of heterogeneous strata on the remediation effect should be considered.

Some studies have shown that the heterogeneity of the stratum can lead to unsatisfactory remediation effects [2]. Even in sandy soils, the heterogeneity of soil also affects the remediation effect. At present, systematic research on the migration, distribution, and remediation effects of steam in heterogeneous aquifers is lacking. In addition, only a few studies exist on the enhanced steam remediation of heterogeneous aquifers.

In the present study, a combination of thermal technologies such as steam injection with thermal conduction heating (TCH) [17] or steam injection with electrical resistance heating (ERH) was adopted to improve the remediation efficiency of steam injection in heterogeneous layers [18], with the aim of using steam injection in high-permeability zones and TCH or ERH in low-permeability zones. However, these methods are more expensive and complicated. Therefore, a method for strengthening steam injection to repair heterogeneous aquifers is needed.

Chao et al. proposed the addition of alcohol in the repair process of air sparging (AS) to enhance remediation efficiency [19]. N-pentanol and n-heptanol were selected as strengthening reagents as both could enhance the removal efficiency of organic compounds; however, the effect of n-heptanol was stronger than that of n-pentanol. The key mechanism is that alcohol molecules can interact with organic compounds at the interface, resulting in increased organic compound volatilization. Based on the theory of enhanced volatilization, it is assumed that alcohols can enhance volatilization more than surfactants [19,20]. Volatility is also a key factor in the process of steam injection and remediation of organic pollutants, which also determines the increased volatilization of organic compounds [21]. According to some studies, alcohol can be used as a surfactant to reduce the surface tension of the solution [22,23] and thus can be used to enhance the volatilization of organic compounds. Previous studies have shown that the addition of ethanol, n-propanol, and n-butanol can reduce surface tension and enhance mass transfer [24]. This study aimed to explore the effects of these alcohols on organic compounds as strengthening reagents.

During steam injection remediation, the removal rate of organic compounds increases with an increase in temperature, and the remediation efficiency increases significantly at boiling point [8,25,26]. Some organics can form azeotropes with water at temperatures lower than their boiling point [27,28]. Therefore, a lower azeotropic temperature can quickly remove organic matter. As alcohol and water can form azeotropes, this study investigated which alcohol could better reduce the azeotropic temperature of organic compounds using the common semi-volatile organic compound nitrobenzene (NB) in contaminated sites as the target pollutant.

Alcohol-enhanced steam injection has rarely been studied, therefore, this study investigated the effects of alcohol on the remediation of heterogeneous aquifers. The effects of the four alcohols (ethanol, n-butanol, n-pentanol, and n-heptanol) on the surface tension and azeotropic temperature of NB were studied. Heterogeneous layers with different permeability ratios (R) were selected to compare the temperature distribution and removal efficiency of organic pollutants under different permeability ratios. The migration and distribution mechanisms of steam in a lens heterogeneous aquifer were also studied. In addition, the effect of alcohol-enhanced remediation was studied for a stratum with a weak remediation effect. This study aims to select an alcohol to enhance the effect of steam injection to remediate contaminated heterogeneous aquifers, thus extending the application of steam injection technology.

## 2. Theoretical Background

### *2.1. Marangoni Effect*

In a gas–liquid mass transfer process, the interface condition is important. Interfacial tension, molecular structure of the interface, intermolecular forces of combining gas and liquid molecules, and interface turbulence all have an important impact on the gas–liquid mass transfer process [29]. During gas–liquid mass transfer, the interfacial convection phenomenon is caused by the change in some physical properties of the liquid such as surface tension and density due to the mass transfer at the interface, which may lead to convective movement of the interfacial fluid [29–31]. Researchers attribute this to the Marangoni effect or Rayleigh effect caused by transmission, which in turn strengthens the transmission process [30,32]. During interphase mass transfer, when the temperature or concentration in different areas on the surface are different, a surface tension gradient is generated, resulting in the movement of liquid on the surface layer and liquid under the interface. This interfacial convection phenomenon is known as the Marangoni effect. The Marangoni effect not only has various geometric patterns on the flow structure, but also enhances the heat and mass transfer processes. Marangoni convection can be characterized by the dimensionless number Ma, which is expressed as follows:

$$\mathrm{Ma} = \frac{\mathrm{d}\Delta\sigma}{\mathrm{D}\mu} \tag{1}$$

where d is the characteristic length (m); $\Delta\sigma$ is the difference in surface tension between the surface fluid and the main fluid (N $\mathrm{m}^{-1}$); D is the diffusion coefficient of the solute in the fluid ($\mathrm{m}^2$ $\mathrm{s}^{-1}$); and $\mu$ is the viscosity of the fluid (Pa s). In Equation (1), when Ma > 0 and exceeds a certain critical value, the surface tension gradient generated by the interface will cause Marangoni convection. In gas–liquid and liquid–liquid liquefaction processes, due to the changes in the physical and chemical properties of the system [33,34], the heat and mass transfer processes cause interfacial instability, and the surface tension is a function of concentration and temperature, which causes the temperature and concentration gradient of the interface to lead to the surface tension gradient of the interface, resulting in Marangoni convection.

### *2.2. Alcohol-and Heat-Enhanced Marangoni Convection*

As the temperature change along the interphase surface can promote the surface tension gradient, it will also cause the Marangoni convection [35,36]. After heating, the surface tension decreases and the surface tension gradient increases, thereby enhancing the Marangoni convection and strengthening the mass transfer process [37,38]. The addition of alcohol reduces the surface tension, and with the evaporation of alcohol, the concentration of alcohol on the liquid film decreases, promoting the diffusion of alcohol molecules to the liquid film and enhancing the gradient of surface tension. This enhances the Marangoni convection [39,40]. The existence of interfacial convection can greatly enhance the interphase mass transfer process and reduce energy consumption.

## 3. Materials and Methods

### *3.1. Materials*

Analytically pure (AR)-grade NB was obtained from Sinopharm Chemical Reagent Co. Ltd., and the alcohols used in this study are shown in Table 1. All the materials were used without further purification, and all aqueous solutions were prepared with deionized water.

### *3.2. Experimental Methods*

#### 3.2.1. Surface Tension

Because ethanol and water are miscible, the surface tension at different volume fractions of ethanol was measured using a surface tension meter. Different volumes of ethanol and water were added to 40 mL headspace bottles and mixed well. The surface tension of the mixtures was measured at room temperature (20 °C). Reagents were added as shown in Table 2.

**Table 1.** List of alcohols used in this study.

| Alcohols | Purity | Manufacturer |
|---|---|---|
| Ethanol | AR | Tianjin Huihang Chemical Technology Co. Ltd. |
| N-butanol | | Guangdong Guanghua Technology Co. Ltd. |
| N-pentanol | | Beijing Chemical Plant Co. Ltd. |
| N-heptanol | | Beijing Chemical Plant Co. Ltd. |

**Table 2.** Specific plan of reagent addition.

| Ethanol: Water | Ethanol Volume Fraction | Ethanol (mL) | Water (mL) |
|---|---|---|---|
| 1 | 1 | 40 | — |
| 9:1 | 0.9 | 36 | 4 |
| 8:2 | 0.8 | 32 | 8 |
| 7:3 | 0.7 | 28 | 12 |
| 6:4 | 0.6 | 24 | 16 |
| 5:5 | 0.5 | 20 | 20 |
| 4:6 | 0.4 | 16 | 24 |
| 3:7 | 0.3 | 12 | 28 |
| 2:8 | 0.2 | 8 | 32 |
| 1:9 | 0.1 | 4 | 36 |
| 0 | 0 | — | 40 |

A total of 3 × 32 mL of ultrapure water was added into three 40 mL headspace bottles separately, followed by 8 mL of n-butanol, n-amyl alcohol, and n-heptanol. The samples were placed in a shaker for 24 h, and the speed of the shaker was set at 180 rpm/min. The headspace bottles were left to stand for 30 min, and then samples were extracted with 5 mL syringes to measure the surface tension by using a surface tension meter. Each experiment was performed in triplicate to avoid experimental errors.

### 3.2.2. Effect of Alcohol on Azeotropy

An azeotropic experimental device is shown in Figure 1. The azeotropic experiment primarily included the binary mixed system and ternary mixed system. The specific experimental scheme is presented in Table 3. The ratio of organic compound/water/alcohol was determined based on the optimal ratio of organic compound/water and the optimal ratio of water/alcohol obtained from previous studies on azeotropes of binary systems. The temperature measurement probes were placed in the upper, middle, and lower positions of the solution; subsequently, a condensate pipe was connected, and the solution was heated to 140 °C in an oil bath. The temperature reading was recorded every minute. Each experimental group was repeated thrice to avoid experimental errors.

### 3.2.3. Steam Remediation of Nitrobenzene-Contaminated Heterogeneous Aquifer

This part of the experiment was conducted in a 2-D simulation tank with the dimensions of 60 cm (length) × 50 cm (height) × 4 cm (width) (Figure 2). The steam injection well installed at the bottom of the tank for stem injection comprised a cylinder with a diameter of 4 cm and height of 7.5 cm, having many tiny pores at the top. The tiny pores were covered with gauze to prevent sand from entering the steam injection well. There were 24 sampling ports in front of the tank to monitor the temperature using a multi-channel temperature detector (Shenzhen Hua Xin Measuring Instrument Company, Shenzhen, China). Figure 2a,b illustrates the experimental schematic design and the layered heterogeneous aquifer device, and Figure 2c shows the lens heterogeneous aquifer. The physical properties of the quartz sand samples used in the tests are presented in Table 4. The experimental filling medium of the layered heterogeneous aquifer is presented in Table 5. The purpose of the experimental design was to simulate the influence of the interface on steam migration when the upper layer was a low-permeability medium and the lower layer was a high-permeability medium in the actual site. The R values of the two groups differed by an order of magnitude, which depicts the scenario of stratified heterogeneous aquifers.

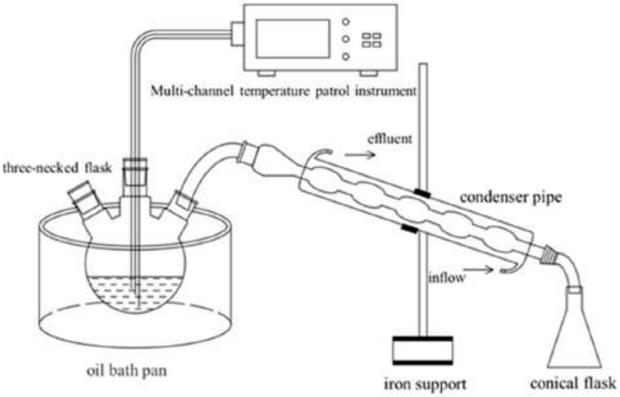

**Figure 1.** Schematic of the azeotropic test device.

**Table 3.** Specific scheme of the experiment.

| Test No. | Reagent Composition | Reagent Addition |
|---|---|---|
| 1 | water + NB | 100 mL + 30 mL |
| 2 | water + NB + ethyl alcohol | 25 mL + 30 mL + 100 mL |
| 3 | water + NB + n-butyl alcohol | 40 mL + 30 mL + 80 mL |
| 4 | water + NB + n-amyl alcohol | 60 mL + 30 mL + 60 mL |
| 5 | water + NB + n-heptanol | 90 mL + 30 mL + 30 mL |

**Figure 2.** Schematic (**a**) and photo (**b**) of the experimental setup for the layered heterogeneous aquifer, and schematic of the experimental device for the lens heterogeneous aquifer (**c**).

**Table 4.** Properties of quartz sand samples in the tests.

| Soil Type | Particle Size (mm) | Hydraulic Conductivity K (cm/s) |
|---|---|---|
| Gravel | 3–5 | $6.1 \times 10^{-1}$ |
| Coarse sand | 0.4–0.85 | $6.5 \times 10^{-2}$ |
| Medium sand | 0.2–0.4 | $3.5 \times 10^{-2}$ |
| Fine sand | 0.1–0.2 | $1.6 \times 10^{-3}$ |

**Table 5.** Specific experimental plan for the layered heterogeneous aquifer experiment.

| Test No. | Packing Configuration | | R |
|---|---|---|---|
| 1 | Upper layer | Medium sand | 17.4 |
| | Lower layer | Gravel | |
| 2 | Upper layer | Fine sand | 381 |
| | Lower layer | Gravel | |

Note: R = hydraulic conductivity of lower layer medium $K_l$/hydraulic conductivity of upper layer medium $K_u$.

The background medium of the lens heterogeneous aquifer was filled with coarse sand and the lens was filled with fine sand. Before the experiment, tap water was continuously injected at a rate of 0.5 m $d^{-1}$ by a peristaltic pump to ensure uniformity of the porous media and to remove entrapped air. Subsequently, 300 mg/L NB was injected into the lower left water inlet until the concentration detected at the upper right water outlet was the same as the water inlet, which simulated the formation and stabilization of the NB contaminant plume. Steam was generated at a constant rate by a 3 kW steam generator (Norbest Machinery Manufacturing Co. Ltd., Wuhan, China), which was supplied by a constant flux of water producing saturated steam at a temperature of 120 °C and pressure of 200 kPa. The steam flow was set to 1 kg $h^{-1}$. The temperatures were continuously measured in the sandbox. Water samples were collected at selected intervals (0–270 min) using a disposable syringe. The concentration of NB in water was analyzed using liquid chromatography (HPLC, Agilent 1260, Santa Clara, CA, USA). The hydraulic conductivity ratio R is defined in the layered heterogeneous aquifer as follows:

$$R = K_l/K_u \tag{2}$$

where $K_l$ is the hydraulic conductivity of the lower layer medium and $K_u$ is the hydraulic conductivity of the upper layer medium.

### 3.2.4. Ethanol-Enhanced Steam Remediation of Nitrobenzene-Contaminated Layered Heterogeneous Aquifers

The experimental device shown in Figure 2 was the same as the previous experimental device. An experimental setting with a hydraulic conductivity ratio R of 381 in the layered heterogeneous aquifer remediation experiment was selected to accelerate the remediation rate experiment. On the completion of the experiment, samples were analyzed for the distribution of pollutants in the aquifer. Furthermore, 500 mL of ethanol at a flow rate of 5 mL/min with a peristaltic pump was injected above the interface to enhance the repair efficiency of the interface in the upper low-permeability zone. The injection positions are shown in Figure 2. In the lens heterogeneous aquifer, 300 mL ethanol was injected into the lens. The ethanol injection volume was calculated using Equation (3). Ethanol distribution stabilization for 2 h was conducted after injecting the ethanol. Later, the concentration distribution of the pollutants before remediation was analyzed. The concentration of NB was determined using liquid chromatography. After injecting hot steam, the sandbox temperature was continuously measured. Water samples were collected at 0–270 min-intervals using a disposable syringe. Ethanol injection volume was calculated using the equation:

$$V = A \times D \times \sigma \times 0.3 \tag{3}$$

where A is the affected area of the low-permeability ($cm^2$); D is the thickness of the simulated tank (cm); σ is the porosity of the medium; and 0.3 is the volume fraction of ethanol.

## 4. Results and Discussion

### *4.1. Effect of Alcohol on Surface Tension*

After adding different volumes of ethanol, the surface tension of the mixture system gradually decreased, with surface tension values of 72.6 mN/m, 22.3 mN/m, and 30 mN/m at 0, 1, and 0.3 volume fractions of ethanol, respectively (Figure 3). Thus, when the volume of ethanol was >0.3 mL, the surface tension of the system significantly reduced, indicating that ethanol can reduce the surface tension of the solution and thus can be used as a surfactant. The optimal ratio of ethanol was 0.3.

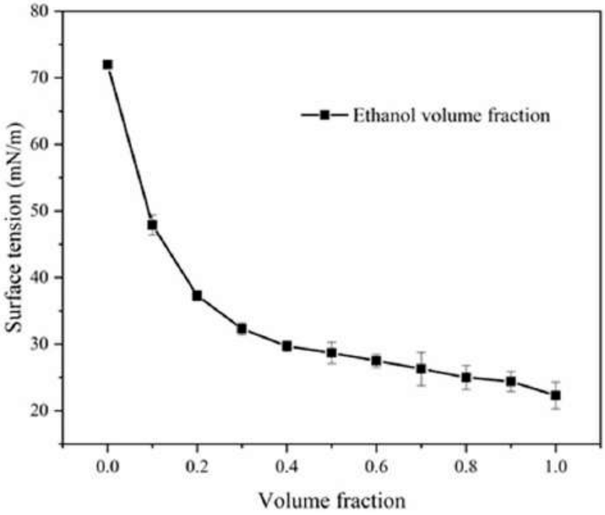

**Figure 3.** Change curve of surface tension under different ethanol volume fractions.

Figure 4 shows the surface tension of different alcohol–water mixtures. N-butanol, n-pentanol, and n-heptanol can greatly reduce the surface tension of the solution, reducing the surface tension of the mixture to below 30 mN/m. The surface tension of the mixed system was almost equal to that of pure alcohol, thereby proving that alcohol is a good agent for reducing surface tension.

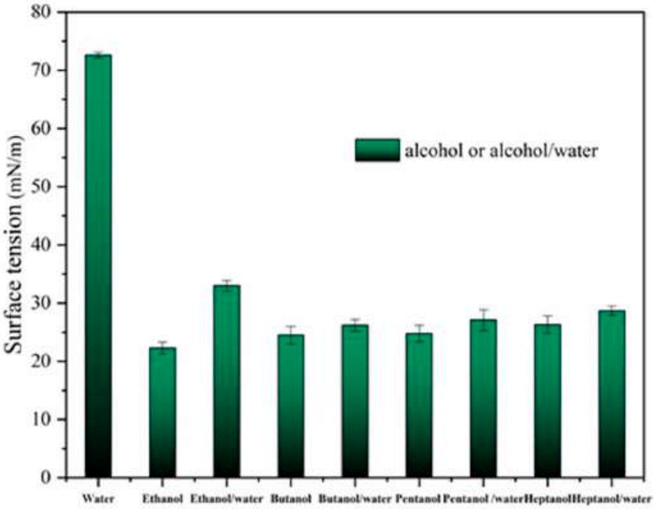

**Figure 4.** Surface tension of different alcohol–water systems, and the volume fraction of alcohol was 0.2.

### *4.2. Effect of Alcohol on Azeotrope*

#### 4.2.1. Azeotropic Temperature of Binary Mixture

Figure 5a shows the azeotropic temperature between NB and water. Initially, an azeotropic plateau occurred, during which the temperature growth rate was approximately 0, azeotropic time was approximately 8 min, and the azeotropic temperature was approximately 97.4 °C. As the temperature increased, the balance of the azeotropic ratio between the liquid phase and the gas phase was disturbed, azeotropic plateau period ended, and the temperature gradually increased to the boiling point of water at 100 °C. The short azeotropic time was primarily due to the low NB content, which did not allow the same proportion of gas and liquid mixture for a long time, thereby ending the azeotrope process. Furthermore, previous studies have shown that the organic compound content is only related to the azeotropic time.

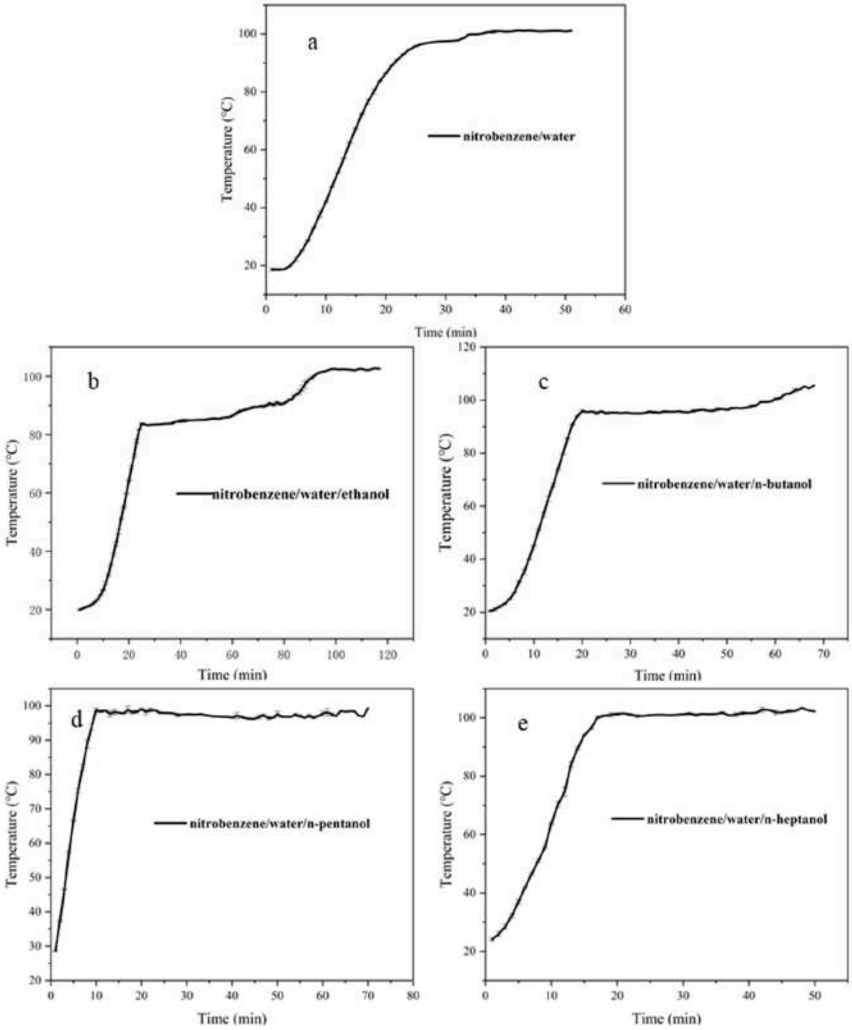

**Figure 5.** Temperature curves of nitrobenzene (NB)–water (**a**), NB/water/ethanol (**b**), NB/water/ n-butanol (**c**), NB/water/ n-pentanol (**d**), and NB/water/ n-heptanol (**e**).

#### 4.2.2. Azeotropic Temperature of Ternary Mixture

The ternary mixture of NB/water/ethanol had an azeotropic plateau (Figure 5b), the azeotropic time lasted for 30 min, azeotropic temperature was 83.2 °C, and temperature increased at 56 min. Compared with the azeotrope of NB and water, adding ethanol could have reduced the azeotrope point by approximately 15 °C, which helped to advance the azeotrope stage by removing NB with hot steam and improving the removal effect. This indicated that ethanol could be used as an azeotropic agent to reduce the azeotropic temperature of NB. The reduction in azeotropic temperature can not only improve the removal efficiency of organic compounds, but also reduce the remediation costs.

The ternary azeotropic mixture of NB, water, and n-butanol entered the azeotropic platform period after 25 min of recording (Figure 5c). The azeotropic temperature was 95.8 °C, and the azeotropic time was 30 min. The azeotropic temperature of the ternary mixture after adding n-butanol was close to that of the binary mixture, which indicated that n-butanol was not effective in reducing the azeotropic temperature.

The azeotropic temperature of the NB/water/n-pentanol ternary azeotropic mixture was 97.7 °C (Figure 5d). N-heptanol was added to the binary mixture of NB/water to form the ternary mixture. The azeotropic temperature was 101.4 °C (Figure 5e). Compared to the boiling point of water, the addition of n-heptanol increased the boiling point of the binary mixture. This indicates that n-pentanol and n-heptanol cannot be used as azeotropic agents to reduce the azeotropic temperature of NB. Only ethanol among the four alcohols could reduce the azeotropic temperature of organic compounds, therefore, ethanol was selected as the enhanced repair reagent in subsequent experiments.

### *4.3. Steam Remediation of Heterogeneous Aquifers Contaminated by Nitrobenzene*

#### 4.3.1. Temperature Distribution of Layered Heterogeneous Aquifer

The temperature distribution of the layered heterogeneous aquifer is shown in Figure 6. Due to the high hydraulic conductivity of the lower medium and the low hydraulic conductivity of the upper medium, the upward transmission of steam was inhibited, resulting in heat accumulation below the interface. Therefore, when R > 1, a blocking interface is formed, resulting in the formation of steam override below the interface and high temperature in the area below the interface. The higher the R value, the higher the temperature below the interface, and the greater the lateral migration distance of the steam. The steam in the lower layer primarily relies on heat convection to transfer heat, whereas it primarily relies on heat conduction in the upper low-permeability zone.

#### 4.3.2. Nitrobenzene Removal in 2-D Layered Heterogeneous Porous Media

When R = 17.4 and steam injection time was 3 h, the NB concentration in the center of the 2-D simulation tank (the position closest to the steam injection point) was the lowest, and the concentration on both sides was high (Figure 7a). This was primarily due to the effect of buoyancy. The vertical migration of steam was faster, resulting in the preferential removal of vertical pollutants. After 6 h of steam injection, the concentration distribution of NB was affected by the interface, and the concentration was the lowest below the interface, with a concentration of 60 mg/L. After 6 h, the NB removal rate in the simulated tank was 68%, of which the removal rates in gravel and medium sand were 70.3% and 65.3%, respectively, and the average NB concentration in medium sand was 1.13 times that of gravel.

When R = 381, the blocking effect of the interface was enhanced (Figure 7b). The NB concentration in the upper layer was evidently higher than that in the lower layer after 3 h of steam injection, and the difference was more obvious with the increase in steam injection time. After 6 h of steam injection, the lowest concentration of NB in gravel reached 28 mg/L, and the average concentration of NB in fine sand was 3.13 times that of gravel. The total removal rate of NB was 60.6%, among which the removal rates in gravel and fine sand were 79.9% and 37%, respectively. Compared with R = 17.4, the total removal rate of NB decreased, while the removal rate of NB in gravel increased.

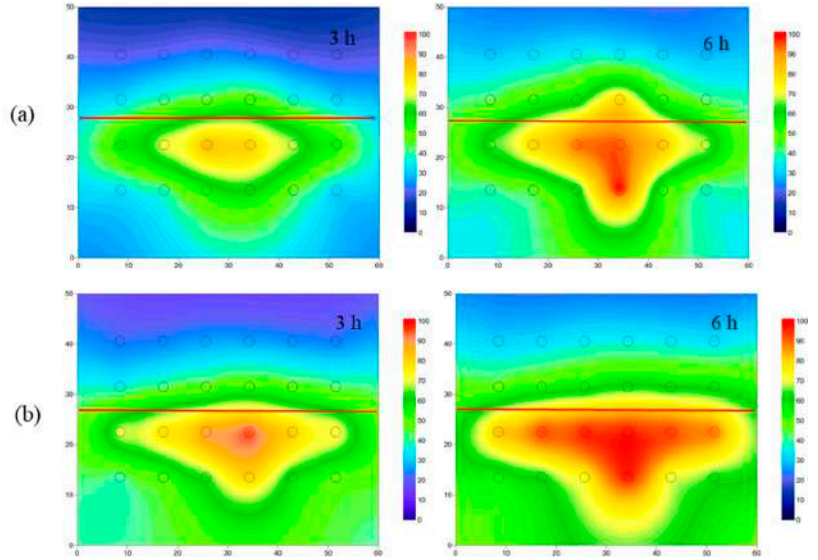

**Figure 6.** Temperature distribution of the layered heterogeneous aquifers (**a**) R = 17.4 (**b**) R = 381.

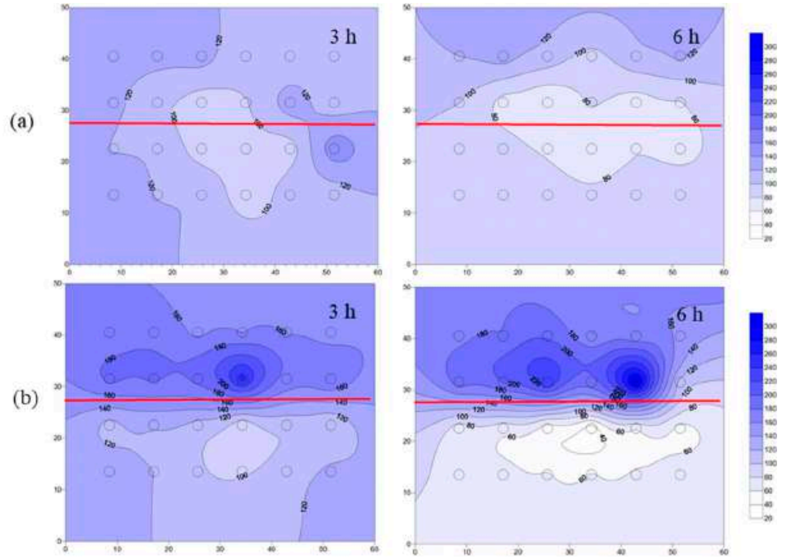

**Figure 7.** Isograms of NB concentrations with different R values: (**a**) R = 17.4; (**b**) R = 381.

#### 4.3.3. Alcohol-Enhanced Steam Remediation of Layered Heterogeneous Aquifer Contaminated by Nitrobenzene

After adding ethanol, some heat was accumulated at the interface, but the temperature difference between the upper and lower layers decreased significantly, the average temperature increased by 15 °C, and the area affected by steam in the low-permeability zone increased by 35% (Figure 8). Alexeev et al. (2005) found that Marangoni convection could enhance liquid phase heat transfer through experimental and numerical simulation [41].

Therefore, the addition of ethanol produces Marangoni convection and enhances mass and heat transfer.

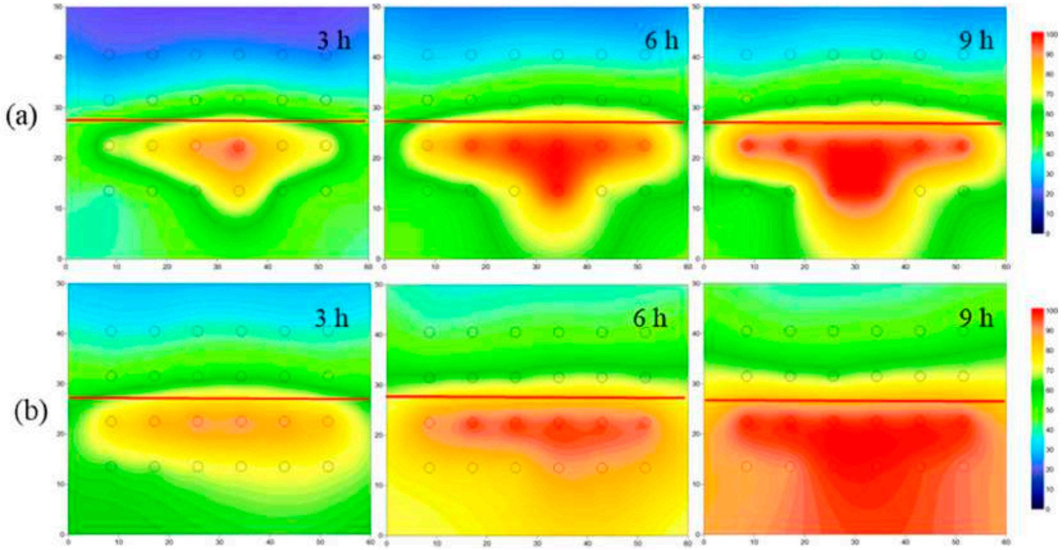

**Figure 8.** Temperature distribution without ethanol (**a**) and with ethanol (**b**) at R = 381.

After adding ethanol, the remediation effect of NB was significantly increased, particularly in the fine sand medium (Figure 9) and the average NB concentration in the simulated tank was reduced by 51%. The average concentration of NB in the lower gravel and upper fine sand decreased by 43.7% and 43.5%, respectively, indicating that ethanol addition enhanced the gas–liquid mass transfer. During the repair process, ethanol volatilized at the gas–liquid interface, forming a surface tension gradient at the interface and increasing the convective vortices in the flow field, resulting in the Marangoni convection [20,40,42]. The Marangoni convection can also enhance heat transfer, and an increase in temperature also enhances NB removal. In addition, ethanol reduces the azeotropic temperature of NB, promoting the boiling of NB at 83.2 °C, thus, improving the removal rate and efficiency of NB.

#### 4.3.4. Alcohol-Enhanced Steam Remediation of Lens Heterogeneous Aquifer Contaminated with NB

Figure 10 shows the temperature distribution of the aquifers containing lenses with and without ethanol solution. Due to the existence of a low-permeability lens, a blocking interface was formed below the lens, and steam flowed around the lens. Only a small amount of steam could enter the fine-sand lens, causing the temperature inside the lens to increase. However, most steam will flow around the lens from the high-permeability area in the form of preferential flow, resulting in an uneven distribution of steam, which affects the removal effect of NB. After adding ethanol, the average temperature in the simulated tank increased by 8 °C, and the steam-affected area increased by 14%, which further confirms that the Marangoni convection generated by ethanol can enhance heat and mass transfer.

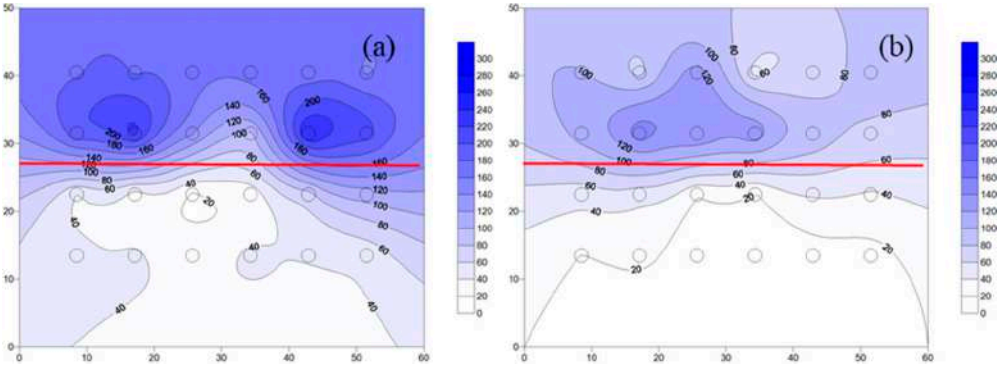

**Figure 9.** Isograms of NB concentration without ethanol (**a**) and with ethanol (**b**) at 9 h.

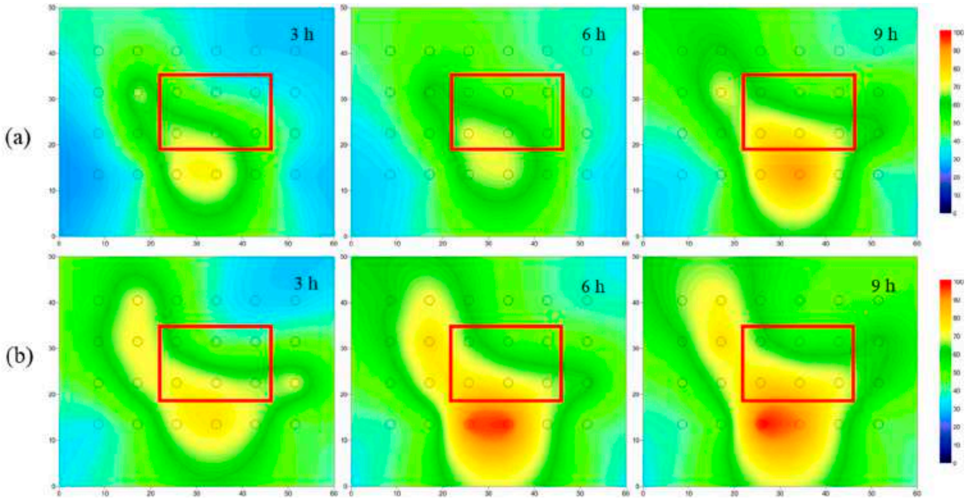

**Figure 10.** Temperature distribution without ethanol (**a**) and with ethanol (**b**) in the lens heterogeneous aquifer.

Figure 11 shows the isolines of NB concentration in the heterogeneous aquifer with the lens. In the lens heterogeneous aquifer, the remediation effect of steam at the edge of the simulation tank and in the lens was weakened due to the preferential flow. After ethanol was added, the mass transfer and heat transfer were enhanced, and the boiling area increased, resulting in an increase in the removal efficiency of NB. The removal efficiency of the tank was increased by 10%, and the NB concentration in the lens was reduced by approximately 58%. Under the same steam flow rate, ethanol addition enhanced the remediation effect of the lens heterogeneous aquifer and reduced the remediation time and cost.

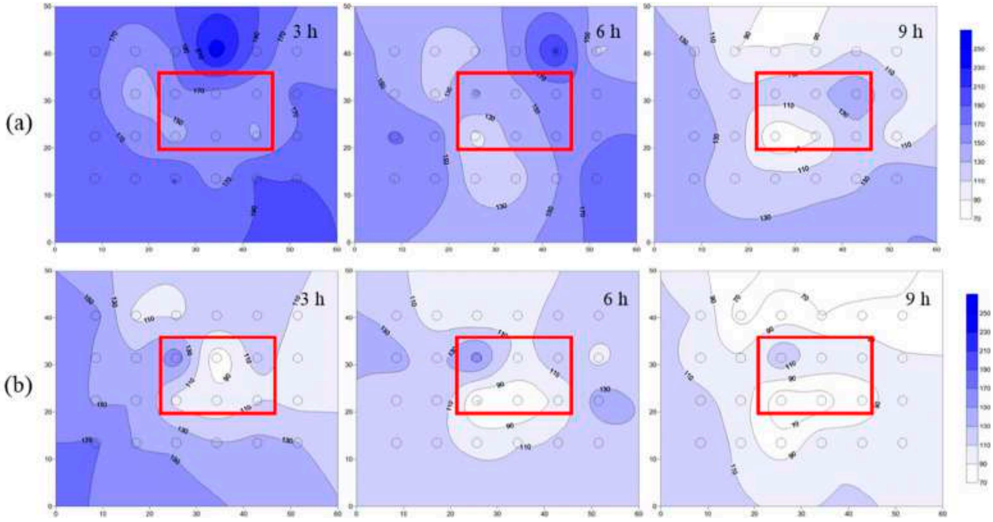

**Figure 11.** Isograms of NB concentration without ethanol (**a**) and with ethanol (**b**) in the heterogeneous aquifer.

## 5. Conclusions

(1) The four alcohols reduced the surface tension of the solution from 72 mN/m to less than 30 mN/m; however, among the four alcohols, only ethanol reduced the azeotropic temperature of NB by 15 °C. Therefore, ethanol can be used as a remediation agent to enhance the steam remediation of heterogeneous aquifers.

(2) When steam entered the layered heterogeneous aquifer, the interface between the low-and high-permeability strata blocked the steam transmission, resulting in poor remediation effect of the low-permeability stratum. After adding ethanol, the average temperature increased, and the area affected by steam increased by 13%, which proved that ethanol addition increased the steam transmission. Moreover, the removal effect of NB was significantly improved, and the average concentration of NB in the simulation tank decreased by 51%.

(3) In the lens heterogeneous aquifer, steam flowed around the lens, forming a preferential flow that resulted in the reduced removal of NB from the lens. After adding ethanol, the steam-affected area increased by 14%, the removal rate of NB increased by 10%, and the NB concentration in the lens decreased by 58%.

(4) Ethanol-enhanced steam injection remediation of heterogeneous aquifers not only enhances the remediation effect and increases the remediation range, but also reduces the remediation costs.

**Author Contributions:** R.L.: Conceptualization, Investigation, Formal analysis, Writing-original draft. X.Y.: Investigation, Validation. J.X.: Investigation, Validation. X.L.: Investigation, Validation. Y.Z.: Conceptualization, Resources, Writing-review & editing. All authors have read and agreed to the published version of the manuscript.

**Funding:** This work was supported by the National Nature Science Foundation of China (Grant No. 41530636), the National and Local Joint Engineering Laboratory for Petrochemical Contaminated Site Control and Remediation Technology of Jilin University, the Jilin Provincial Key Laboratory of Water Resources and Environment of Jilin University, and the Key Laboratory of Groundwater Resources and Environment of Ministry of Education (Jilin University).

**Institutional Review Board Statement:** Not applicable.

**Informed Consent Statement:** Not applicable.

**Data Availability Statement:** Some or all data, models, or codes that support the findings of this study are available from the corresponding authors on request.

**Acknowledgments:** This study was financially supported by the Key Project of the National Natural Science Foundation of China (Grant No. 41530636). The authors thank the Key Laboratory of Groundwater Resources and Environment, Ministry of Education for providing financial assistance.

**Conflicts of Interest:** The authors declare no conflict of interest.

## References

1. Al Yousef, Z.; AlDaif, H.; Al Otaibi, M. An overview of steam injection project in Fractured Carbonate Reservoirs in the Middle East. *J. Pet. Sci. Res.* **2014**, *3*, 101–110. [CrossRef]
2. Davis, E.L. Steam injection for soil and aquifer remediation. *Environ. Prot. Agency* **1998**, *505*, 1–16.
3. Udell, K.S. Application of in situ thermal remediation technologies for DNAPL removal. *Groundw. Qual. Remediat. Prot.* **1998**, *250*, 367–374.
4. Gudbjerg, J.; Sonnenborg, T.O.; Jensen, K.H. Remediation of NAPL below the water table by steam-induced heat conduction. *J. Contam. Hydrol.* **2004**, *72*, 207–225. [CrossRef]
5. Basel, M.D.; Udell, K.S. *Effect of Heterogeneities on the Shape of Condensation Fronts in Porous Media*; American Society of Mechanical Engineers: New York, NY, USA, 1991; pp. 63–70.
6. Schmidt, R.; Gudbjerg, J.; Sonnenborg, T.O.; Jensen, K.H. Removal of NAPLs from the unsaturated zone using steam Prevention. *J. Contam. Hydrol.* **2002**, *55*, 233–260. [CrossRef]
7. Heron, G.; Christensen, T.H.; Enfield, C.G. Henry's law constant for trichloroethylene between 10 and 95 °C. *Environ. Sci. Technol.* **1998**, *32*, 1433–1437. [CrossRef]
8. Schwardt, A.; Dahmke, A.; Köber, R. Henry's law constants of volatile organic compounds between 0 and 95 °C—Data compilation and complementation in context of urban temperature increases of the subsurface. *Chemosphere* **2021**, *272*, 129858. [CrossRef]
9. Sleep, B.E.; McClure, P.D. The effect of temperature on adsorption of organic compounds to soils. *Can. Geotech. J.* **2001**, *38*, 46–52. [CrossRef]
10. Philippe, N.; Davarzani, H.; Colombano, S.; Dierick, M.; Klein, P.-Y.; Marcoux, M. Experimental study of the temperature effect on two-phase flow properties in highly permeable porous media: Application to the remediation of dense non-aqueous phase liquids (DNAPLs) in polluted soil. *Adv. Water Resour.* **2020**, *146*, 103783. [CrossRef]
11. Tzovolou, D.N.; Aggelopoulos, C.A.; Theodoropoulou, M.A.; Tsakiroglou, C.D. Remediation of the unsaturated zone of NAPL-polluted low permeability soils with steam injection: An experimental study. *J. Soils Sediments* **2010**, *11*, 72–81. [CrossRef]
12. Heron, G.; Vanzutphen, M.; Christensen, H.T.; Enfield, G.C. Soil heating for enhanced remediation of chlorinated solvents_a laboratory study on resistive heating and vapor extraction in a silty, low-permeable soil contaminated with trichloroethylene. *Environ. Sci. Technol.* **1998**, *32*, 1474–1481. [CrossRef]
13. Ochs, S.O.; Class, H.; Färber, A.; Helmig, R. Methods for predicting the spreading of steam below the water table during subsurface remediation. *Water Resour. Res.* **2010**, *46*, 1–16. [CrossRef]
14. Class, H.; Helmig, R. Numerical simulation of non-isothermal multiphase multicomponent processes in porous media. 2. Applications for the injection of steam and air. *Adv. Water Resour.* **2002**, *25*, 551–564. [CrossRef]
15. Nilsson, B.; Tzovolou, D.; Jeczalik, M.; Kasela, T.; Slack, W.; Klint, K.E.; Haeseler, F.; Tsakiroglou, C.D. Combining steam injection with hydraulic fracturing for the in situ remediation of the unsaturated zone of a fractured soil polluted by jet fuel. *J. Environ. Manage.* **2011**, *92*, 695–707. [CrossRef] [PubMed]
16. Davis, E.; Akladiss, N.; Hoey, R.; Brandon, B.; Nalipinski, M.; Carroll, S.; Herom, G.; Novakowski, K.; Udell, K. Steam Enhanced Remediation Research for DNAPL in Fractured Rock. *EPA* **2005**, *10*, 1–190.
17. Baker, R.S.; Heron, G. In-Situ Delivery of Heat by Thermal Conduction and Steam Injection for Improved Dnapl Remediation. In Proceedings of the 4th International Conference on Remediation of Chlorinated and Recalcitrant Compounds, Monterey, CA, USA, 24–27 May 2004; Battelle Press: Monterey, CA, USA, 2004.
18. Heron, G.; Carroll, S.; Nielsen, S.G. Full-Scale Removal of DNAPL Constituents Using Steam-Enhanced Extraction and Electrical Resistance Heating. *Ground Water Monit. Remediat.* **2005**, *25*, 92–107. [CrossRef]
19. Chao, H.P.; Hsieh, L.C.; Tran, H.N. Increase in volatilization of organic compounds using air sparging through addition in alcohol in a soil-water system. *J. Hazard. Mater.* **2018**, *344*, 942–949. [CrossRef]
20. Chang, Y.; Yao, M.; Bai, J.; Zhao, Y. Study on the effects of alcohol-enhanced air sparging remediation in a benzene-contaminated aquifer: A new insight. *Environ. Sci. Pollut. Res. Int.* **2019**, *26*, 35140–35150. [CrossRef]
21. Abd Rahman, N.; Azizan, N.A.; Kamaruddin, S.A.; Chelliapan, S.; Mohd Jaini, Z.; Yunus, R.; Rahmat, S.N. Steam-Enhanced Extraction Experiments, Simulations and Field Studies for Dense Non-Aqueous Phase Liquid Removal: A Review. *MATEC Web Conf.* **2016**, *47*, 05012. [CrossRef]
22. Yuan, Z.; Herold, K.E. Surface tension of pure water and aqueous lithium bromide with 2-ethyl-hexanol. *Appl. Therm. Eng.* **2001**, *21*, 881–897. [CrossRef]
23. Biscay, F.; Ghoufi, A.; Malfreyt, P. Surface tension of water-alcohol mixtures from Monte Carlo simulations. *J. Chem. Phys.* **2011**, *134*, 044709. [CrossRef]

24. Moraveji, M.K.; Sajjadi, B.; Davarnejad, R. Gas-Liquid Hydrodynamics and Mass Transfer in Aqueous Alcohol Solutions in a Split-Cylinder Airlift Reactor. *Chem. Eng. Technol.* **2011**, *34*, 465–474. [CrossRef]
25. Chen, F.; Freedman, D.L.; Falta, R.W.; Murdoch, L.C. Henry's law constants of chlorinated solvents at elevated temperatures. *Chemosphere* **2012**, *86*, 156–165. [CrossRef] [PubMed]
26. Koproch, N.; Dahmke, A.; Kober, R. The aqueous solubility of common organic groundwater contaminants as a function of temperature between 5 and 70 °C. *Chemosphere* **2019**, *217*, 166–175. [CrossRef]
27. Komninos, N.P.; Rogdakis, E.D. Geometrical investigation and classification of three-suffix margules binary mixtures including single and double azeotropy. *Fluid Phase Equilib.* **2019**, *494*, 212–227. [CrossRef]
28. Maalem, Y.; Zarfa, A.; Tamene, Y.; Fedali, S.; Madani, H. Prediction of thermodynamic properties of the ternary azeotropic mixtures. *Fluid Phase Equilib.* **2020**, *517*, 112613. [CrossRef]
29. Imaishi, N.; Suzuki, Y.; Hozawa, M.; Fujinawa, K. Interfacial turbulence in gas-liquid mass transfer. *Int. Chem. Eng.* **1982**, *22*, 659–665. [CrossRef]
30. Marangoni, C. Ueber die Ausbreitung der Tropfen einer Flüssigkeit auf der Oberfläche einer anderen. *Ann. Der Phys. Und Chem.* **1871**, *219*, 337–354. [CrossRef]
31. Bénard, H. *Les Tourbillons Cellulaires—Dans une Nappe Liquide Propageant de la Chaleur par Convection, en Régime Permanent*; Thèse Présentée à la Faculté des Sciences de Paris; Par, M., Bénard, H., Eds.; Gauthier-Villars: Paris, France, 1901.
32. Rayleigh, L. LIX. On convection currents in a horizontal layer of fluid, when the higher temperature is on the under side. *Lond. Edinb. Dublin Philos. Mag. J. Sci.* **1916**, *32*, 529–546. [CrossRef]
33. Mao, Z.-S.; Chen, J. Numerical simulation of the Marangoni effect on mass transfer to single slowly moving drops in the liquid–liquid system. *Chem. Eng. Sci.* **2004**, *59*, 1815–1828. [CrossRef]
34. Ma, Y.; Yu, G.; Li, H.Z. Note on the mechanism of interfacial mass transfer of absorption processes. *Int. J. Heat Mass Transf.* **2005**, *48*, 3454–3460. [CrossRef]
35. Bodenschatz, E.; de Bruyn, J.R.; Ahlers, G.; Cannell, D.S. Transitions between patterns in thermal convection. *Phys. Rev. Lett.* **1991**, *67*, 3078–3081. [CrossRef]
36. Vidal, A.; Acrivos, A. Effect of Nonlinear Temperature Profiles on Onset of Convection Driven by Surface Tension Gradients. *Ind. Eng. Chem. Fundam.* **1968**, *7*, 53–58. [CrossRef]
37. McTaggart, C.L. Convection driven by concentration- and temperature-dependent surface tension. *J. Fluid Mech.* **1983**, *134*, 301–310. [CrossRef]
38. Buffone, C.; Sefiane, K.; Easson, W. Marangoni-driven instabilities of an evaporating liquid-vapor interface. *Phys. Rev. E* **2005**, *71*, 056302. [CrossRef]
39. Sha, Y.; Chen, H.; Yin, Y.; Tu, S.; Ye, L.; Zheng, Y. Characteristics of the Marangoni Convection Induced in Initial Quiescent Water. *Ind. Eng. Chem. Res.* **2010**, *49*, 8770–8777. [CrossRef]
40. Liu, D.; Tran, T. Vapor-Induced Attraction of Floating Droplets. *J. Phys. Chem. Lett.* **2018**, *9*, 4771–4775. [CrossRef] [PubMed]
41. Alexeev, A.; Gambaryan-Roisman, T.; Stephan, P. Marangoni convection and heat transfer in thin liquid films on heated walls with topography: Experiments and numerical study. *Phys. Fluids* **2005**, *17*, 062106. [CrossRef]
42. Zhang, J.; Oron, A.; Behringer, R.P. Novel pattern forming states for Marangoni convection in volatile binary liquids. *Phys. Fluids* **2011**, *23*, 072102. [CrossRef]

applied sciences

MDPI

*Article*

# Use of Foamed Cement Banking for Reducing Expressways Embankment Settlement

**Yuedong Wu [1,2], Hui Liu [1,2] and Jian Liu [1,2,*]**

[1] College of Civil and Transportation Engineering, Hohai University, Nanjing 210098, China; hhuwyd@163.com (Y.W.); lxiao_hui@hhu.edu.cn (H.L.)
[2] Key Laboratory of Ministry of Education for Geomechanics and Embankment Engineering, Hohai University, Nanjing 210098, China
* Correspondence: 20170053@hhu.edu.cn; Tel.: +86-183-6296-0323

**Abstract:** Expressways are often built on soft ground, the foundation of which is not processed adequately during the construction period. Consequently, the traffic safety and embankment stability will be seriously affected due to uneven settlement. The technology of holing the embankment and replacing foamed cement banking (FCB) could control the settlement of an embankment without road closure, thus reduce the impact of construction on normal operation of highways. In this paper, the principle of FCB is described. Additionally, a sedimentation ratio calculation method, through the analysis of the settlement load ratio, is proposed for calculating the roadbed replacement thickness. This paper takes the example of the test section EK0 + 323 on Shen-Jia-Hu expressway in Zhejiang Province and combines with site settlement monitoring data to confirm the effectiveness of the calculation method proposed.

**Keywords:** construction disturbance; replacement of embankment; foamed cement banking technology; post-construction settlement; method of replacement thickness calculation

**Citation:** Wu, Y.; Liu, H.; Liu, J. Use of Foamed Cement Banking for Reducing Expressways Embankment Settlement. *Appl. Sci.* **2021**, *11*, 11959. https://doi.org/10.3390/app112411959

Academic Editors: Daniel Dias and Bing Bai

Received: 14 October 2021
Accepted: 13 December 2021
Published: 15 December 2021

**Publisher's Note:** MDPI stays neutral with regard to jurisdictional claims in published maps and institutional affiliations.

**Copyright:** © 2021 by the authors. Licensee MDPI, Basel, Switzerland. This article is an open access article distributed under the terms and conditions of the Creative Commons Attribution (CC BY) license (https://creativecommons.org/licenses/by/4.0/).

## 1. Introduction

With the rapid development of expressway construction, in China, construction on soft ground is sharply increasing, such as Shen-Jia-Hu Expressway that passes through soft soil [1,2]. Owing to shortened construction periods and to the rheological properties of soft soil, among other reasons, the embankment after settlement of many highways opened abroad is too high, which does not meet relevant regulatory requirements (i.e., post-construction should be less than 30.0 cm) [3]. The post-construction settlement of expressways has become a major type of expressway damage, which will not only seriously affect the vehicle's road speed, traffic safety, and driving comfort, but also seriously affect the stability and safety of the highway itself [4–6].

In order to reduce post-construction settlement, the embankment is replaced with light soil to reduce the overburden load and control the settlement [7,8]. At present, the widely used light soils mainly include EPS beads-mixed lightweight soil, EPS block, and foamed cement banking, which include good integrity, light mass, and convenient construction. The lightweight soil's cohesion, global strength, bulk density, and other parameters can be adjusted by adjusting the output of cement and foam [9]. The advantages and disadvantages of various methods are shown in Table 1. Foamed cement banking research is already well underway in numerous countries [10–12], and some results have been achieved in practice. Compared with other materials, the FCB has a shorter construction period, lower curing time, and higher construction quality, thus it has broad application prospects [13,14]. As FCB's bulk density is only conventional soil bulk density of 1/4 to 1/8, its use as a replacement of embankment material [15–17], can not only reduce the base load pressure, but can also reduce the total settlement and differential settlement [18]. Replacing the undisturbed soil with lightweight soil to process the post-construction settlement of expressway under traffic control seriously affected highway traffic operations. Especially, there are no closed roads (ramps) during construction, the lightweight soil is being put down to achieve subgrade compactness, that causes huge economic losses due to the road closure.

**Table 1.** Comparison of different lightweight fills.

| Material Type | Advantage | Disadvantage |
|---|---|---|
| EPS beads-mixed lightweight soil | Low density and compressibility; high strength; environmental protection. | Difficult construction; high material cost; poor corrosion resistance. |
| EPS block | Low density; stable nature; convenient construction. | High material cost; poor impact resistance; easy to local cavity. |
| Foamed cement banking | Low density; good integration; high strength and corrosion resistance; short construction period. | High cement hydration heat; high material cost. |

In this paper, foamed cement replacement is carried out on both sides of the embankment, which does not affect the normal traffic operation during replacement construction, its use is targeted and flexible, and only small settlement occurs after improvement. Combined with Shen-Jia-Hu EK0 + 323 highway section, this paper verifies the advantages of FCB in dealing with embankment settlement without road closure. Through the analysis of dynamic monitoring data of Shen-Jia-Hu expressway's subgrade settlement, and according to the proportional relationship between settlement and load, the calculation method of embankment replacement thickness is proposed, which can be applied to complex construction processes, this work can thus provide a reference for similar future projects.

## 2. Design Principles and Calculation Method

### 2.1. Principle of FCB

FCB is a new technology for reducing embankment settlement while ensuring the normal operation of road transport, its schematic diagram is shown in Figure 1. First, the amount of FCB replacement needed is based on the amount of static load of embankment to be uninstalled, which is, in turn, used to design the transverse hole construction plan. Then, drilling horizontal holes on the embankment continuously, with the hole machinery along the embankment on one side or both sides, next, FCB is injected directly into the holes using perfusion enrichment after the hole formed. The unit weight of regular FCB filling is 5.5–6.0 kN/m$^3$, which is 1/3 to 1/4 of the general soil bulk density (i.e., 20 kN/m$^3$), to effectively reduce the embankment permanent load. The undisturbed foundation soil becomes super-solid, and the effect of the improvement is clear. The normal operation of the highway will not be affected during construction.

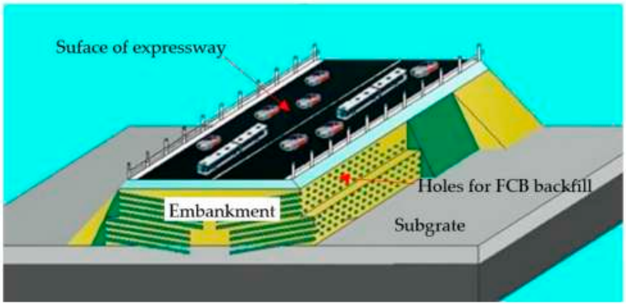

**Figure 1.** Embankment FCB replacement construction by citing transverse holes.

### 2.2. Calculation Method

The most important link of FCB displacement control of a subgrade is to identify the replacement thickness of the roadbed. This currently relies heavily on the layerwise summation method for estimation of total deposition, as well as comparative analysis with settlement monitoring data available before improvement, leading to the determination of the replacement thickness [18] in the transverse hole for the filling of the road embankment stage, which mainly depends on the layerwise summation method. When this method is used to calculate the settlement under complex loading and unloading conditions, it produces large errors.

For easier calculation of displacement thickness. Chen [19] had proposed a calculation formula of unloading quantity, but it is necessary to be combined with engineering practice to determine the parameters, which has a high cost. Thus, based on the formula proposed by Chen and the ratio variation between load and settlement, a method for calculating unloading according to the settlement is proposed as follows:

$$P_c = h \cdot (\gamma_1 - \gamma_0) \tag{1}$$

where $\gamma_1$ is the embankment unit weight that generally ranges between 19.0 and 21.0 kN/m$^3$, and $\gamma_0$ is the foamed lightweight concrete embankment wet unit weight ranging between 5.5 and 6.0 kN/m$^3$; $P_c$ is the embankment unloading amount, and $h$ is the replacement thickness.

At present, the existing settlement data is mainly used to predict the settlement curve, and the replacement thickness is determined according to the result. The weight of embankment was reduced by replacing the undisturbed soil, which can reduce settlement. Therefore, when the monitored settlement data does not meet the requirements, the embankment should be improved. The unloading value is mainly determined by the difference between the bulk density of the replacement material and the undisturbed soil mass. Thus, the method proposed in this paper has an advantage of calculating the unloading value of the overload embankment to a certain extent, even though there is a difference in establishing the initial expression. To devise an expression that can calculate the replacement thickness under different conditions, including overload, equivalent load, and under load conditions (i.e., after embankment soil replacement with FCB), further research on the relationship between foundation consolidation settlement and pressure must be conducted.

Based on the assumption that unloading construction is not performed on the embankment, the embankment ultimate settlement under pressure $P_0$ is $S_\infty^{p+\Delta p}$, and the observed foundation settlement before unloading construction is $S_m$. If embankment unloading construction is implemented and the unloading amount is $P_c$, the embankment residual weight $P_u^1$ induces the ultimate settlement $S_\infty^h$, and a formula for settlement calculation can be given as follows:

$$\frac{S_\infty^{p+\Delta p}}{S_\infty^h} = \frac{P_0}{P_u^1} \tag{2}$$

Owing to the fact that the settlement calculation considers rebound under unloading conditions, the following concepts should be clarified. When unloading $P_c$ in FCB embankment replacement is completed, the load $P_c \cdot S_m / S_\infty^{P+\Delta P}$ had converted into effective load, unloading this part of the load will cause rebound. As a result, this part of the capacity should take the swelling index caused by unloading into account, the swelling index is usually taken as $\delta$ times the compression settlement (engineering empirical suggested range of values: 0.05–0.03). Meanwhile, the other part of the load that is not converted is $P_c \cdot (1 - S_m / S_\infty^{P+\Delta P})$, and its settlement computation is suggested to confirm normal compression settlement. Therefore, the settlement caused by unloading is expressed as:

$$S_c = \frac{\left[1 - (1-\delta)\frac{S_m}{S_\infty^{P+\Delta P}}\right]}{P_0} \cdot P_c \cdot S_\infty^{P+\Delta P} \tag{3}$$

After unloading construction, the actual remaining consolidation settlement $S_m^1$ is expressed as:

$$S_m^1 = S_m - S_c = S_m - \frac{[1-(1-\delta)\frac{S_m}{S_\infty^{P+\Delta P}}]}{P_0} \cdot P_c \cdot S_\infty^{P+\Delta P} \tag{4}$$

Considering the allowable post-construction settlement $\Delta S$ in design work, by summing the actual remaining settlement $S_m^1$ and allowable post-construction settlement $\Delta S$, the total ultimate settlement $S_\infty^h$ induced by the residual embankment load after moving the load $P_c$ is obtained:

$$S_m^1 + \Delta S = S_\infty^h \tag{5}$$

$$P_c = \frac{P_0 \cdot (S_\infty^{P+\Delta P} - S_m - \Delta S)}{(1-\delta) \cdot S_m} = \vartheta \cdot P_0 \cdot (\frac{S_r - \Delta S}{S_m}) \tag{6}$$

where $S_r$ is the residual settlement before improvement with FCB, $S_r = S_\infty^{P+\Delta P} - S_m$; $S_m$ is the monitoring data during construction; $S_\infty^{P+\Delta P}$ is the computed ultimate settlement under the embankment load $P_0$ function; $P_0$ is the embankment gravity load, and $\Delta S$ is the design-allowable post-construction settlement for which a local standard is suggested for determining its value. $\vartheta$ is the rebound correction factor expressed as $\vartheta = 1/(1-\delta)$, where $\delta$ is the swelling index within the range 0.05–0.3.

Under the condition that the embankment design applies overload pre-loading, if the calculated subgrade unloading confirms that $P_c \leq P_0 - P_u$, $P_u$ is the amount of overload, the post-construction settlement requirement can be satisfied after removing the overload pressure. When $P_c > P_0 - P_u$, except for removing overload, it is necessary to apply FCB to process the excess load, $P_c - (P_0 - P_u)$. If equivalent load pre-compression is applied in embankment reinforcement, the computation of FCB replacement thickness should take the unloading value $P_c$ into account. If the embankment design condition is under load pre-compression $(P_0 \leq P_u)$, computation of the FCB replacement thickness should confirm the expression: $P_c + P_u - P_0$.

In order to use equation (6) to calculate unloading value, parameters $P_0$ and $S_m$ can be acquired by measuring before unloading, and $\delta$ is determined either by laboratory sample testing or by practical engineering empirical estimation. $\Delta S$ is allowable post-construction settlement decided by local standard regulations [20]. The ultimate settlement $S_\infty^{P+\Delta P}$ contributing to the pre-loading effect before unloading, it can be obtained by conventional layerwise summation method or by prediction of measured settlement during preloading construction.

## 3. Field Study on Shen-Jia-Hu Highway

### 3.1. Engineering Situation

The practical site for experiments was part of the Zhejiang Shenjiahua Hangzhou Expressway (Lianhang Section) project (hereafter referred to as the Shen-Jia-Hu expressway), which is located on Hang-jia-hu plain, the geographical location of Shen-Jia-Hu is shown in Figure 2. This region has a developed economy, high population density, and high transportation requirements. However, the numerous lakes and rivers cause a large amount of soft soil in this region. Most of its road sections pass through soft soil foundation, which contain soils characterized by high moisture content, high compression, low strength, and low permeability, which will cause greater road settlement.

In view of the engineering geological conditions, in addition to conventional improvement methods such as grout spray pile (pile diameter 500.0 mm, 3.05 million linear meters) and prestressed concrete pipe pile (pile diameter 400.0 mm, wall thickness 60.0 mm, 590 thousand linear meters), Shen-Jia-Hu expressway also adopted equal preloading (2.39 million m$^3$) along the whole line. The expressway subgrade was filled with earthworks mixture. The foundation improvement mainly adopted stacking load pre-compaction and combined the plastic wick drain. The road section chosen for experiments is the EK0 + 323 ramp bridge road, which has a 10 m wide pavement, a 3.25 m high embankment, and a 1:1.5 slope grade. The soil cohesion and internal friction angle were obtained through direct shear experiment, and the soil water content was obtained through the oven-drying method. The other parameters and specific steps were determined according to the Standard for geotechnical testing method [3], and the parameters are given in Table 2. It should be noted that the soil parameters were obtained after the surcharge preloading method. The cohesion values were relatively higher than other soil.

**Figure 2.** Geographic position of Shen-Jia-Hu expressway.

**Table 2.** Soil parameters.

| Type of Soil Layer | Thickness (m) | Water Content (%) | Natural Density (g/cm$^3$) | Void Ratio | Compression Modulus (MPa) | Compression Factor (Mpa$^{-1}$) | Cohesion (kPa) | Internal Friction Angle |
|---|---|---|---|---|---|---|---|---|
| Planting soil | 2.1 | - | - | - | - | - | - | - |
| Silty clay | 1.2 | 22.7 | 1.95 | 0.64 | 7.24 | 0.22 | 45.00 | 15.20 |
| Silt clay | 10.4 | 51.5 | 1.70 | 1.40 | 2.91 | 0.83 | 32.50 | 20.30 |
| Clay | 11.2 | 30.7 | 1.90 | 0.86 | 5.89 | 0.32 | 30.30 | 23.90 |
| Fine sand interlayer | 0.4 | 24.5 | 1.98 | 0.70 | 16.81 | 0.10 | - | - |
| Silty clay | 3.9 | 23.4 | 1.99 | 0.68 | 10.93 | 0.15 | 40.00 | 26.50 |

### *3.2. Construction Process*

According to the FCB construction process, the embankment slope was excavated to prepare a construction plane, and then drilling equipment was used to drill lateral holes to a designed depth in the embankment, which would not affect highway traffic operations. PVC plastic tubing or plug gauge was inserted in the hole to test the hole quality, and then the FCB material was cast in the holes, the holes were drilled in the embankment slop by the drilling machine as shown in Figure 3. A construction point worthy of attention is that the FCB pouring process should be implemented immediately after drilling the holes avoid a hole deforming under the overlying embankment load. The slope cover was cast using FCB material after all the holes were filled with FCB. The key point in this construction step is to cast the slope according to design's required proportional grading. Finally, the embankment slope was covered with soil and landscaped with plants.

### *3.3. Improvement before Analysis of Monitoring Data*

Settlement observation was conducted during the period January 2010 to August 2010. In the EK0 + 323 section, the largest settlement, reaching over 129.0 mm, occurred on a road bridge, affecting the speed of traffic and highway safety. In September 2010, asphalt concrete pavement filling was applied, and it was later observed that the roadbed continued sinking at a larger sedimentation rate (i.e., 9.1 mm/month). On 25 March 2011, the settlement reached its maximum, 219.0 mm. Measurements of the settlement before the application of FCB are shown in Figure 4.

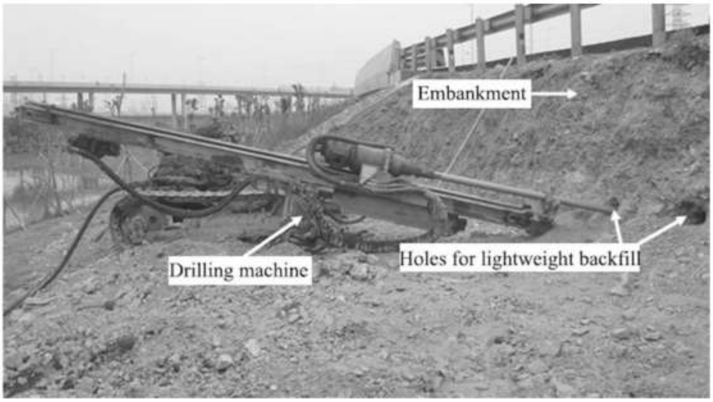

**Figure 3.** Drilling holes on north sides of the embankment. Reprinted with permission from Ref. [18]. Copyright 2021 IEEE Proceedings.

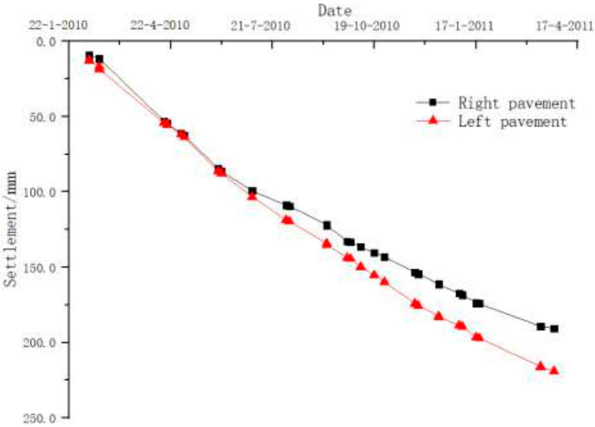

**Figure 4.** Total embankment settlement before improvement with FCB.

As shown in Figure 4, until 25 March 2011, no obvious convergence trend in the subsidence curves was noted, based on the post-construction monitoring settlement data. The reason may be due to tight deadlines resulting in inadequate preloading foundation, making the work required after settlement too large in scope. A settlement prediction formula [21] for EK0 + 323 settlement was used to demonstrate this method. Based on the bridge sections of EK0 + 323 and two settlement observation sections, the settlement prediction results are shown in Table 3. To simplify the forecasting process and meet the requirements of settlement prediction analysis with prediction process, secondary consolidation settlement was not considered.

The settlement prediction results showed that section EK0 + 323′s settlement will be up to 402.2 mm. Not taking into account the largest remaining secondary consolidation, settlement will again lead to vehicle bumping; thus, holes filled with bubbled and mixed FCB were introduced in section EK0 + 323 for improvement.

Following the above-described unloading calculation method, the FCB replacement quantity was 102.4 m$^3$, and the total FCB volume for embankment improvement was separated into 774 lateral holes with diameters of Φ 150 mm (including 719 holes that were 6.0 m deep and 55 holes that were 4.0 m deep).

**Table 3.** Settlement forecast.

| Section | | Settlement Rate March (mm/month) | Present Settlement (mm) | The Settlement Forecast (mm) | Residual Settlement (mm) |
|---|---|---|---|---|---|
| EK0 + 323 | left | 9.2 | 189.6 | 292.9 | 103.3 |
| | right | 11.2 | 219.3 | 402.2 | 182.9 |

### 3.4. Effectiveness Analysis of Improvement

For the FCB improvement of section EK0 + 323, the embankment settlement data based on dynamic monitoring data analysis is shown in Figure 5.

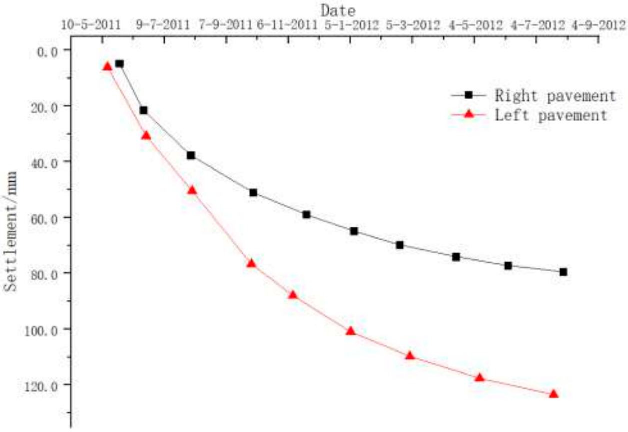

**Figure 5.** Total embankment settlement after improvement with FCB.

Section EK0 + 323 is located on a bridgehead segment, and according to the pre-construction settlement prediction, the remaining post-construction settlement of the left and right sides were 182.9 and 103.3 mm, respectively, until May 2011. As shown in Figure 5, after improvement with FCB on both the left and right sides, the settlements were 57.1 and 44.2 mm after embankment improvement finished (i.e., October 2011), respectively. Comparing the two sites, after initial construction of the section, the settlement exhibited a relatively sharp decreasing trend. The reason was that during the improvement process, the construction disturbance caused an impact on the embankment. The settlement after improvement was approximately 70% of the predicted settlement. Additionally, the average remaining settlement was 43.2 mm, meeting the residual settlement thresholds (i.e., less than the 30.0 cm) of the expressway embankment after improvement.

The results of EK0 + 323 after replacement improvement using the proposed technology revealed a monthly settlement rate of 50%, which was a reduction from the remaining settlement after construction of 70%. After improvement with the lateral hole replacement technology, the remaining settlement met the threshold for the settlement control after construction standards, and effectively suppressed the recurrence of bumping.

## 4. Discussion

Using FCB to replace the undisturbed soil of embankment on both sides cannot affect the normal operation of the highway. It can avoid economic losses caused by closure. FCB has very good fluidity, so it can be pumped to the designed depth and has a fast construction speed, so the construction period can be greatly shortened.

By calculating the replacement thickness of the embankment by using the formula proposed in this paper, after improving the embankment with this thickness, the settlement of embankment begins to stabilize. The residual settlement of embankment meets the thresholds (i.e., less than the 5.0 cm). Thus, this calculation formula, proposed in this paper, can be used in embankment improvement projects. During the improvement of the embankment, the settlement has a sharply increasing trend. It may be caused by embankment disturbance during the construction period. Thus, embankments should be replaced by the undisturbed soil in the same section, which is used to analyze the impact of construction disturbance. Additionally, monitoring the road surface settlement without embankment improvement, which is used to prove that the decrease in foundation settlement rate is caused by FCB improvement.

## 5. Conclusions

In this paper, Shen-Jia-Hu Expressway section EK0 + 323 served as the basis for a project to introduce new FCB design principles and calculation methods. From the results obtained through experiments on the test section as well as via subgrade settlement dynamic monitoring data analysis, the following conclusions can be drawn.

(1) The FCB method is an effective means to reduce highway embankment differential settlement without disturbing normal traffic, which has the following advantages: (1) convenience for continued highway operation, (2) high flexibility, and (3) an ideal improvement effect.

(2) Based on the proportional relationship between unloading amount and settlement value, a calculation method for unloading amount determination was developed herein. This method was used to determine the amount of embankment replacement and apply it to actual projects, which was then verified to be practical and accurate.

(3) According to the theoretical settlement value predicted in the previous article, and from the analysis of field monitoring data from practical highway projects, the pavement monthly settlement ratio was theoretically reduced by 50% and the residual post-construction settlement by 60% when transverse drilling and FCB improvement were completed. Therefore, in practice, FCB improvement is an effective means to control and reduce embankment differential settlement.

**Author Contributions:** The formal analysis, formula reasoning, and the performance of the experiment, as well as the original draft preparation, were completed by H.L.; Review and editing were completed by Y.W. and J.L. All authors have read and agreed to the published version of the manuscript.

**Funding:** The research was funded by supported by the Fundamental Research Funds for the Central Universities, number B200204036.

**Institutional Review Board Statement:** Not applicable.

**Informed Consent Statement:** Not applicable.

**Data Availability Statement:** Data sharing not applicable. No new data were created or analyzed in this study.

**Conflicts of Interest:** The authors declare no conflict of interest.

## References

1. Wang, Y.S. Settlement of soft soil foundation of Expressway. *China J. Highw. Transp.* **1993**, *6*, 61–66.
2. Zhou, S.; Wang, B.L.; Shan, Y. Review of research on high-speed railway subgrade settlement in soft soil area. *Railw. Eng. Sci.* **2020**, *28*, 129–145. [CrossRef]
3. CCCC Second Highway Survey and Design Institute. *Specifications for Design of Highway Subgrades*; China Communications Press: Beijing, China, 2015; pp. 69–70, 84–85.
4. Li, J.; He, D.P.; Peng, Y.H. Alleviating bump at bridge-head using geocell flexible approach slab. In Proceedings of the Third International Conference on Transportation Engineering, Chengdu, China, 23–25 July 2011; ASCE: Reston, VA, USA, 2011; pp. 1609–1617.

5. Pan, X.D.; Du, Z.G.; Yang, X.G. Evaluation indexes of the impact of vehicle bumping at bridge-head on driving safety. *J. Tongji Univ. Nat. Sci.* **2006**, *34*, 634–637.
6. Zhao, X.X.; Yang, L.J. Analysis and management methods for the road and bridge transition's sedimentation on the soft clay ground in Shanghai. *J. Lanzhou Jiaotong Univ.* **2008**, *27*, 37–40.
7. Lu, T.; Yang, P.; Li, M.X.; Yi, L.H. Analysis of deformation behavior of foamed lightweight soil subgrade on soft soil foundation. *Subgrade Eng.* **2018**, *46*, 38–41.
8. Liu, H.L.; Yi, F.; Chen, Y.H. Study on method of laterally replacing subgrade of existing expressway by light soil. *J. Highw. Transp. Res. Dev.* **2019**, *36*, 19–27.
9. Huang, T.Y.; Wang, X.Q.; Fang, G.W.; Zhang, H.P.; Diao, H.G. Design and calculation methods of light soil replacement after preloading in the soft soil foundation of the highway. *Urban Rapid Rail Transit* **2019**, *37*, 59–63.
10. Jones, M.R.; McCarthy, A. Utilizing unprocessed low-lime coal fly ash in foamed concrete. *Fuel* **2005**, *84*, 1398–1409. [CrossRef]
11. Wang, Z.J.; Sun, Z.C.; Lu, L.; Li, J.B. Study on the uniaxial compressive mechanical properties of foamed mixture lightweight soil with polypropylene fibers. *Chin. J. Undergr. Space Eng.* **2018**, *16*, 1021–1029.
12. Li, Y.Z. Foamed cement banking for reinforcing soft ground. *Miner. Explor.* **2008**, *11*, 66–68.
13. Gao, Y.L.; Xiao, M.Q.; Guan, H.X. Foamed cement banking and its utilization in highway engineering. *Bull. Chin. Silic. Soc.* **2016**, *35*, 2432–2438.
14. Deng, H.W. Bubble-mixed light soil applied in a metro high-fill roadbed. *Urban Rapid Rail Transit* **2018**, *31*, 88–91.
15. Ding, X.H. Study on design and calculation of foamed cement banking. *Subgrade Eng.* **2017**, *35*, 146–151.
16. Jamnongpipatkul, P.; Dechasakulsom, M.; Sukolrat, J. Application of air foam stabilized soil for bridge-embankment transition zone in Thailand. In Proceedings of the American Society of Civil Engineers GeoHunan International Conference, Changsha, China, 3–6 August 2009; ASCE: Reston, VA, USA, 2009; pp. 181–193.
17. Xiao, L.J. Foamed Cement Banking and Applications in Highway Construction. Master's Thesis, Hunan University, Changsha, China, 2003.
18. Wu, Y.D.; Liu, J. Research on foamed cement banking for non-uniform differential settlement in used super highway. In Proceedings of the International Conference on Electric Technology and Civil Engineering, Lushan, China, 22–24 April 2011; IEEE: Washington, DC, USA, 2011; pp. 5334–5337.
19. Chen, Y.H.; Shi, G.C.; Cao, D.H.; Ying, H.J.; Wang, X.Q. Control of post-construction settlement by replacing subgrade with foamed cement banking. *Chin. J. Geotech. Eng.* **2011**, *33*, 1854–1862.
20. Cao, D.H.; Chen, Y.H.; Wang, X.Q.; Sun, H.; Wei, J. A study on dynamic controlling to embankment settlement of Shen-jia-hu-hang expressway. *Highway* **2010**, *55*, 45–48.
21. Nanjing Hydraulic Research Institute. *Standard for Geotechnical Testing Method*; China Planning Press: Beijing, China, 2019; pp. 16–125.

applied sciences

MDPI

*Article*

# Analysis of Hydrogeochemical Characteristics and Origins of Chromium Contamination in Groundwater at a Site in Xinxiang City, Henan Province

**Wenfang Chen [1], Yaobin Zhang [2,*], Weiwei Shi [1], Yali Cui [2], Qiulan Zhang [2], Yakun Shi [1] and Zexin Liang [2]**

[1] The First Institute of Geo-Environment Survey of Henan, Zhengzhou 450045, China; chenwf.hndk@hotmail.com (W.C.); shiweiwei.hjyy@hotmail.com (W.S.); shiyakun@yeah.net (Y.S.)
[2] School of Water Resources and Environment, China University of Geosciences (Beijing), Beijing 100083, China; cuiyl@cugb.edu.cn (Y.C.); qlzhang919@cugb.edu.cn (Q.Z.); 2105190003@cugb.edu.cn (Z.L.)
* Correspondence: 3005190010@cugb.edu.cn

**Abstract:** Hexavalent chromium contamination in groundwater has become a very serious and challenging problem. Identification of the groundwater chemical characteristics of the sites and their control mechanisms for remediation of pollutants is a significant challenge. In this study, a contaminated site in Xinxiang City, Henan Province, was investigated and 92 groundwater samples were collected from the site. Furthermore, the hydrogeochemical characteristics and the distribution patterns of components in the groundwater were analyzed by a combination of multivariate statistical analysis, Piper diagram, Gibbs diagram, ions ratio and hydrogeochemical simulation. The results showed that the $HCO_3$-Cl-Mg-Ca type, $SO_4$-$HCO_3$-Na type, and $HCO_3$-Mg-Ca-Na type characterize the hydrogeochemical composition of shallow groundwater and $HCO_3$-Cl-Mg-Ca type, $HCO_3$-Na-Mg type, and $HCO_3$-$SO_4$-Mg-Na-Ca type characterize the hydrogeochemical composition of deep groundwater. Ion ratios and saturation index indicated that the groundwater hydrogeochemical characteristics of the study area are mainly controlled by water–rock action and evaporative crystallization. The dissolution of halite, gypsum and anhydrite, the precipitation of aragonite, calcite and dolomite, and the precipitation of trivalent chromium minerals other than $CrCl_3$ and the dissolution of hexavalent chromium minerals occurred in groundwater at the site. The minimum value of pH in groundwater at the site is 7.55 and the maximum value is 9.26. The influence of pH on the fugacity state of minerals was further investigated. It was concluded that the saturation index of dolomite, calcite, aragonite and $MgCr_2O_4$ increases with the increase of pH, indicating that these minerals are more prone to precipitation, and the saturation index of $Na_2Cr_2O_7$, $K_2Cr_2O_7$ and $CrCl_3$ decreases with the increase of pH, implying that $Na_2Cr_2O_7$, $K_2Cr_2O_7$ and $CrCl_3$ are more prone to dissolution. The saturation index of the remaining minerals is less affected by pH changes. The study can provide a scientific basis for groundwater remediation.

**Keywords:** groundwater; hydrochemistry; hexavalent chromium contamination; water chemistry simulation

**Citation:** Chen, W.; Zhang, Y.; Shi, W.; Cui, Y.; Zhang, Q.; Shi, Y.; Liang, Z. Analysis of Hydrogeochemical Characteristics and Origins of Chromium Contamination in Groundwater at a Site in Xinxiang City, Henan Province. *Appl. Sci.* **2021**, *11*, 11683. https://doi.org/10.3390/app112411683

Academic Editor: Bing Bai

Received: 29 October 2021
Accepted: 22 November 2021
Published: 9 December 2021

**Publisher's Note:** MDPI stays neutral with regard to jurisdictional claims in published maps and institutional affiliations.

**Copyright:** © 2021 by the authors. Licensee MDPI, Basel, Switzerland. This article is an open access article distributed under the terms and conditions of the Creative Commons Attribution (CC BY) license (https://creativecommons.org/licenses/by/4.0/).

## 1. Introduction

In many parts of the world, water scarcity has posed a great threat to socio-economic development and the ecological environment [1,2]. Due to the limited surface water resources and precipitation, groundwater resources have become indispensable freshwater resources for domestic drinking, irrigation water and industrial activities [3–6]. With large-scale industrial activities, groundwater pollution has become a serious problem affecting human health and life in many countries and regions, and as of 2018, the number of declared contaminated sites in 31 provincial capitals in China reached 174. In the process of industrial development, chromium has been used in a growing number of industries, and chromium salt production has subsequently developed to a certain extent [7–11]. At the same time, a large amount of chromium slag was produced, and after its long-term open piling, Cr(VI) will seep into the soil and groundwater with surface runoff, thus causing pollution to the surrounding soil and groundwater, and since Cr(VI) is a highly migratory and toxic pollutant, chromium pollution in groundwater has therefore become a serious worldwide problem [12–15]. Cr(VI) has been identified as highly toxic and one of the carcinogens, posing a threat to human health when chromium exceeds drinking water standards.

Groundwater contamination investigation and remediation is urgent, and the analysis of hydrogeochemical parameters are important to grasp the groundwater quality status [16–21]. The study of hydrogeochemical composition and its origins is the basis of groundwater protection and restoration. There are many methods, with the most common ones being multivariate statistical analysis [22,23], the isotope labeling method and the hydrogeochemical simulation method [24–26]. Xiao Yong et al. studied the characteristics and controlling factors of groundwater chemistry in the long-term use area of reclaimed water in Beijing by Piper's trilinear diagram, ionic proportional relationship and saturation index method, and concluded that the changes in the types of groundwater chemistry and water–rock action during the rainy and dry season, and believed that the hydrogeological conditions of the area should be fully considered when reclaimed water was used for agricultural irrigation and ecological landscape [27]. Zhang Jingtao et al. explored the hydrogeochemical characteristics and evolution of groundwater in the Dachaidan area from the pre-mountain alluvial fan to the salt lake by ion ratio analysis, Gibbs plot and hydrogeochemical simulation, and concluded that the water–rock interaction was dominated by the dissolution of halite and gypsum and positive cation exchange [28]. Ashwani used a multivariate statistical and hydrogeochemical approach to analyze Cr(VI) concentration levels, pollutant sources and groundwater geochemistry in an industrial town in Italy to provide an effective aid for water resource management in the region [29]. By testing chemical parameters related to fluoride in groundwater during the periods of abundance, flatness and depletion, D. Laxmankumar concluded that weathering, ion exchange and anthropogenic activities played an important role on the chemical composition of groundwater using Gibbs plot and principal component analysis [30].

Chromium exists in groundwater mainly as trivalent chromium and hexavalent chromium [31]. The migration and transformation of chromium in groundwater is influenced by the redox potential, acidity and concentration [32,33]. Under acidic conditions with low redox potential, chromium mainly exists as Cr(III). As pH increases, the solubility of Cr(III) decreases and $Cr(OH)_3$ precipitation is formed. Under alkaline conditions with high redox potential, chromium is mainly present as Cr(VI) [34,35]. Most of the research focused on the chromium migration and transformation by performing batch and column experiments indoors. The chromium presence pattern was analyzed by varying different pH and concentration values by the controlled variable method. Column experiments usually take a lot of time to complete. In this study, the presence pattern of Cr in representative samples was characterized by numerical simulation using saturation index.

Xinxiang City is a significant industrial base in the North China Plain. To date, there are many left industrial contaminated sites. Thus, it is necessary to get insight into the influence of contaminants on groundwater. Although it has been determined that the groundwater quality at the contaminated site exceeds the Class III water standard, the groundwater hydrogeochemical characteristics and their governing mechanisms are still poorly known. The purpose of this work was to investigate the level of contamination in groundwater, hydrogeochemical characteristics and their origins at a contaminated site in Xinxiang by using mathematical statistics, correlation analysis, ion ratio analysis and saturation index, and to study the hydrogeochemical processes controlling the evolution of groundwater chemistry and the influencing factors of chromium-containing mineral by means of hydrogeochemical simulation. This study will provide effective assistance for groundwater remediation in the region.

## 2. Description of the Study Area

The study area is located in the northwestern part of Xinxiang City, Henan Province (Figure 1), with a temperate continental monsoon climate and a multi-year average temperature of 14 °C. The multi-year average precipitation is 586.32 mm, with more than 70% occurring in the rainy season spanning June to September. The multi-year average evaporation is 1772.62 mm, which is three to four times the precipitation with the strongest evaporation in June.

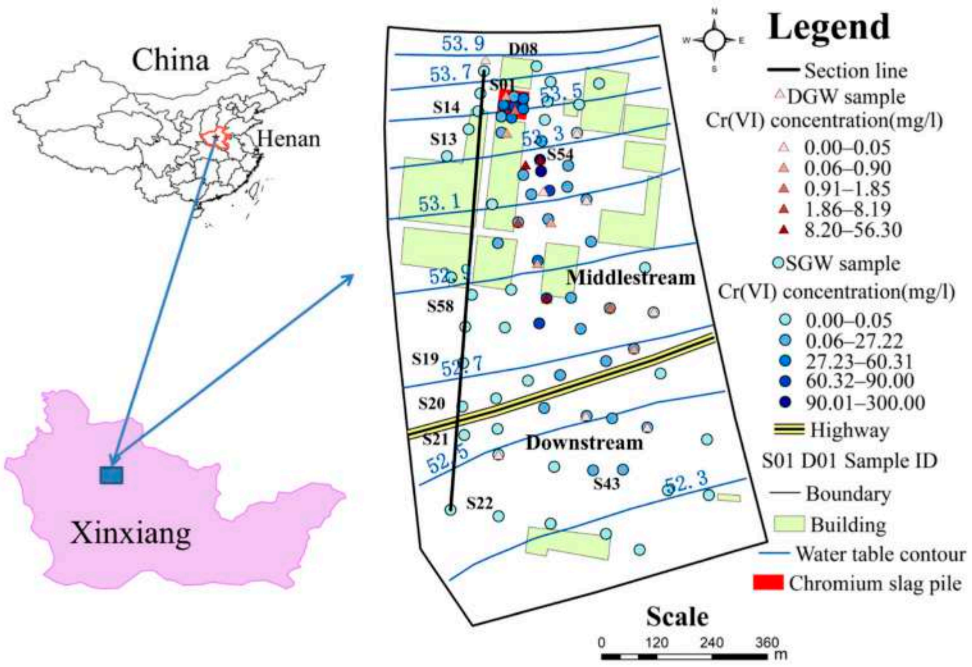

**Figure 1.** Location of the study area and the sampling sites. DGW represents deep groundwater. SGW represents shallow groundwater. Dots represent shallow sampling points. Triangles represent deep sampling points. The boundary represents the boundary of the numerical model. Henan is located in the central part of China. Xinxiang City is located in the north of Henan Province.

Xinxiang City is located at the southeastern foot of Taihang Mountains and the northern edge of the alluvial plain in the middle and lower reaches of the Yellow River. The terrain generally inclines from northwest to southeast. The regional landform types are divided into three types of landforms: alluvial valley, alluvial sloping plains and alluvial plains. The geomorphological type of the study area is alluvial sloping plain. The surface of the study area reveals the Quaternary river-phase sedimentary layer with a thickness of 50–60 m, and the lithology is mainly clay and sand. The groundwater type is pore water of loose rock of the Quaternary, and the media of the aquifer are mainly medium sand and fine sand, with coarse sand locally. According to the profile, it can be seen that the lithology from 56 m to 49 m is silty clay and silt. The lithology from 59 m to 49 m is silty clay and silt. This is followed by a shallow aquifer with a thickness of 3 m. However, the aquifer thickness increased significantly at borehole S22. The lithology from 46 m to 36 m is mainly silty clay. The bottom lithology is mainly fine sand. The aquifer is mainly recharged by atmospheric precipitation, lateral runoff and irrigation recharge, and groundwater discharge is mainly exploitation, evaporation and lateral runoff.

Chromium salt chemical plants existed in the study area during the historical period, and chromium slag from the production process brought serious contamination to the site soil and groundwater (Figure 2). Test results showed that the average concentration of total chromium in the soil was 12,100 mg/kg, and work has been carried out to remediate the soil and groundwater.

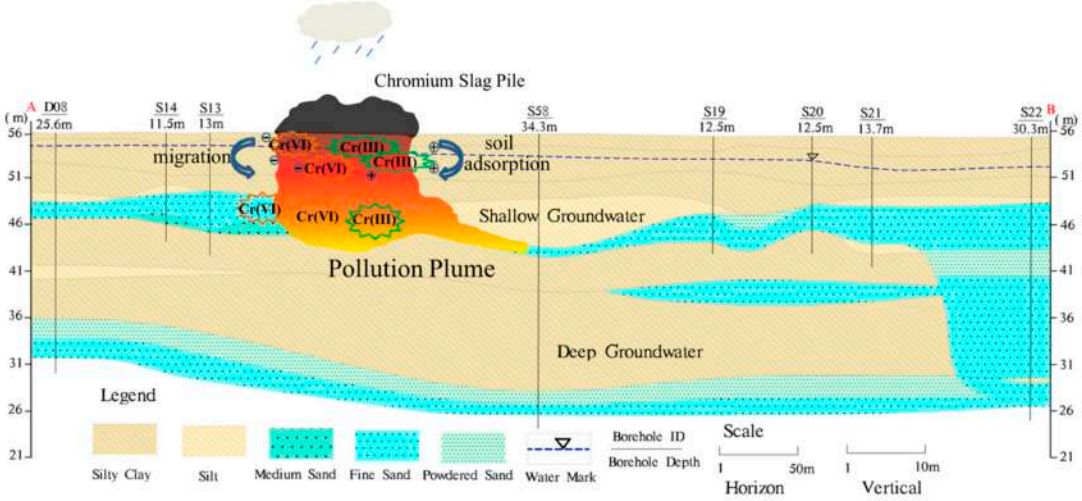

**Figure 2.** The hydrogeological cross section along the A–B and pollution conceptual model. In the pollution plume, the red color represents the high concentration value. Yellow color represents low concentration value.

## 3. Materials and Methods

### 3.1. Sample Collection and Analysis

In groundwater contamination investigation sampling, determining the location of sampling sites was a key factor. This sampling was mainly based on the following principles. Firstly, samples should uniformly along the groundwater flow direction. Secondly, the sampling points are encrypted in the seriously polluted areas. Thirdly, the general shape of the contamination plume can be determined according to the sampling points.

In December 2020, field investigations and sampling were conducted in the study area, and 92 groundwater samples were collected, including 73 shallow groundwater (SGW) samples and 19 deep groundwater (DGW) samples, with the locations of the sampling sites as shown in Figure 1. The total dissolved solids (TDS) and pH were measured in the field using a multiparameter tester. Other chemical indicators ($Na^+$, $Ca^{2+}$, $Mg^{2+}$, $K^+$, Cr(VI), $HCO_3^-$, $SO_4^{2-}$, $Cl^-$, $NO_3^-$) were measured in the laboratory of Henan Province Rock and Mineral Testing Center. The charge balance errors of all samples were within 5%, and the accuracy of each indicator met the quality requirements.

### 3.2. Multivariate Statistical Analyses

Statistical methods are an effective tool in groundwater quality assessment. Groundwater contamination can be determined by graphical and multivariate statistical methods, such as, Piper diagram, Gibbs diagram and Ion ratio. Multivariate statistical methods play an important role in the identification of pollution sources, such as correlation analysis. It can determine the degree of correlation between different parameters. Pearson's correlation coefficient was used to analyze the degree of dependency of one parameter to the other [26,36].

## 4. Results and Discussion

### *4.1. Hydrochemistry*

The analysis of groundwater chemistry data can help to determine the geochemical parameters of groundwater and the distribution characteristics of contaminants. The statistics and analysis of the test results of groundwater samples were shown below.

The minimum value of pH of shallow groundwater in the study area was 7.55 and the maximum value was 9.26, which was alkaline overall and favorable to the precipitation and oxidation of trivalent chromium. The average distribution of the main cation concentrations: $Na^+ > Ca^{2+} > Mg^{2+} > Cr > K^+ > Fe > Mn > NH_4^+ > As > Pb$, and the average distribution of the main anion concentrations: $HCO_3^- > SO_4^{2-} > Cl^- > NO_3^- > CO_3^{2-} > NO_2^-$. The order of triple nitrogen content in groundwater in the study area was $NO_3^- > NO_2^- > NH_4^+$, which mainly polluted groundwater in the form of nitrate nitrogen [37].

Among the ionic components of shallow groundwater, the coefficients of variation of $SO_4^{2-}$, $Cl^-$, $NO_3^-$, $Na^+$, $Ca^{2+}$, $Mg^{2+}$, $HCO_3^-$ and Fe were relatively small, and the contents of these ions in shallow groundwater were relatively stable. In contrast, the coefficients of variation (C.V.) of $NO_2^-$, Mn, $NH_4^+$, As, Pb, Cr(VI), $CO_3^{2-}$ and $K^+$ all exceeded 100%, which belonged to a strong degree of variation, indicating that the contents of these ions in shallow groundwater were highly variable, and at the same time these ions were sensitive factors that vary with environmental and anthropogenic factors.

The pH of deep groundwater in the study area was 7.8 at minimum and 8.34 at maximum, which was alkaline overall. The distribution of the main cation concentration: $Na^+ > Ca^{2+} > Mg^{2+} > Cr(VI) > K^+ > Fe > Mn > NH_4^+$, the distribution of the main anion concentration: $HCO_3^- > SO_4^{2-} > Cl^- > NO_3^- > NO_2^-$, and As, Pb, $CO_3^{2-}$ were not detected in the deep aquifer. The distribution of the remaining ions was similar to that of the shallow layer.

As can be seen from Table 1, the coefficients of variation of $SO_4^{2-}$, $Cl^-$, $NO_3^-$, $Na^+$, $Ca^{2+}$, $Mg^{2+}$, $HCO_3^-$, Fe and $K^+$ in the deep groundwater were relatively small, and the contents of these ions in deep groundwater were relatively stable. The coefficients of variation of $NO_2^-$, Mn, $NH_4^+$, Cr(VI) and $CO_3^{2-}$ all exceeded 100%, which belonged to strong degree of variation.

**Table 1.** Statistical descriptions of chemical parameters.

| Index | Shallow Groundwater | | | | | Deep Groundwater | | | | |
|---|---|---|---|---|---|---|---|---|---|---|
| | Min | Max | Mean | SD | C.V./% | Min | Max | Mean | SD | C.V./% |
| pH | 7.55 | 9.26 | 8.03 | 0.32 | 3.99 | 7.80 | 8.34 | 8.19 | 0.19 | 2.27 |
| TDS | 738.36 | 2532.60 | 1206.26 | 389.76 | 32.31 | 504.00 | 1198.26 | 798.04 | 185.94 | 23.30 |
| $SO_4^{2-}$ | 100.94 | 1963.05 | 413.64 | 403.01 | 97.43 | 8.61 | 475.94 | 160.72 | 125.68 | 78.20 |
| $Cl^-$ | 83.05 | 461.59 | 204.31 | 72.86 | 35.66 | 7.81 | 206.98 | 109.56 | 45.42 | 41.46 |
| $NO_3^-$ | 0.56 | 322.92 | 117.82 | 81.63 | 69.28 | 3.95 | 200.17 | 70.75 | 57.29 | 80.97 |
| $NO_2^-$ | 0.00 | 2.43 | 0.39 | 0.61 | 156.41 | 0.00 | 1.29 | 0.25 | 0.31 | 123.05 |
| $Na^+$ | 77.34 | 1372.00 | 292.15 | 266.48 | 91.21 | 63.94 | 322.5 | 129.35 | 62.76 | 48.52 |
| Fe | 0.04 | 4.88 | 1.09 | 1.05 | 96.33 | 0.01 | 1.64 | 0.49 | 0.45 | 91.63 |
| Mn | 0.01 | 7.17 | 0.53 | 1.05 | 198.11 | 0.00 | 1.36 | 0.26 | 0.35 | 132.48 |
| $NH_4^+$ | 0.00 | 1.80 | 0.12 | 0.30 | 250.00 | 0.00 | 0.50 | 0.07 | 0.15 | 230.90 |
| As | 0.00 | 0.10 | 0.005 | 0.02 | 400.00 | 0.00 | 0.00 | 0.00 | 0.00 | 0.00 |
| Pb | 0.00 | 0.02 | 0.002 | 0.004 | 200.00 | 0.00 | 0.00 | 0.00 | 0.00 | 0.00 |
| Cr(VI) | 0.00 | 299.99 | 18.34 | 50.86 | 277.32 | 0.00 | 56.30 | 8.31 | 17.85 | 214.79 |
| $Fe^{3+}$ | 0.04 | 2.55 | 0.70 | 0.65 | 92.86 | 0.01 | 1.01 | 0.31 | 0.30 | 96.93 |
| $CO_3^{2-}$ | 0.00 | 40.76 | 1.17 | 5.50 | 470.09 | 0.00 | 0.00 | 0.00 | 0.00 | 0.00 |
| $HCO_3^-$ | 298.39 | 1052.65 | 589.11 | 140.58 | 23.86 | 389.56 | 687.95 | 518.25 | 83.32 | 16.08 |
| $K^+$ | 0.38 | 14.48 | 1.45 | 2.04 | 140.69 | 0.45 | 3.23 | 0.80 | 0.61 | 75.94 |
| $Ca^{2+}$ | 15.57 | 231.90 | 143.59 | 34.95 | 24.34 | 38.54 | 148.10 | 101.48 | 30.01 | 29.58 |
| $Mg^{2+}$ | 26.65 | 246.90 | 117.38 | 32.88 | 28.01 | 52.27 | 143.50 | 95.11 | 24.25 | 25.49 |
| Cr | 0.00 | 332.90 | 21.81 | 57.36 | 263.00 | 0.00 | 63.28 | 10.41 | 21.69 | 208.33 |

Note: The units of minimum, maximum and average values in the table are mg/L except for pH. SD: Standard Deviation. C.V.: Coefficient of Variation.

## *4.2. Spatial Distribution Characteristics of Groundwater Chemistry*

### 4.2.1. Hydrogeochemical Facies

A Piper diagram can help to evaluate the geochemical relationships between different dissolved ions and dominant types of water chemistry in groundwater [38]. The TDS of shallow groundwater was 738.4–2532.6 mg/L [39]. The shallow groundwater was highly variable with $HCO_3^-$, $SO_4^{2-}$, $Cl^-$, $NO_3^-$ as the main anions and $Na^+$, $Ca^{2+}$, $Mg^{2+}$ as the main cations. The $NO_3^-$ concentration in the water samples was high and exceeded the quality standard for domestic drinking water, probably due to the inappropriate use of fertilizers making $NO_3^-$ enter the groundwater with rainfall and irrigation [40]. The $HCO_3$-Cl-Mg-Ca type, $SO_4$-$HCO_3$-Na type and $HCO_3$-Mg-Ca-Na type characterized the hydrogeochemical composition of shallow groundwater (Figure 3). The groundwater below the chromium slag pile (CSP) was $SO_4$-$HCO_3$-Na type. The reason was related to the production process of chromium salt, and the specific chemical reaction was $2Na_2CrO_4 + H_2SO_4 = Na_2Cr_2O_7 + Na_2SO_4 + H_2O$, so $SO_4^{2-}$ and $Na^+$ will enter the groundwater under the leaching effect of chromium slag. The downstream was basically uncontaminated, and the groundwater was $HCO_3$-Mg-Ca-Na type. The groundwater of middle reaches and east of the chromium slag piles was $HCO_3$-Cl-Mg-Ca type.

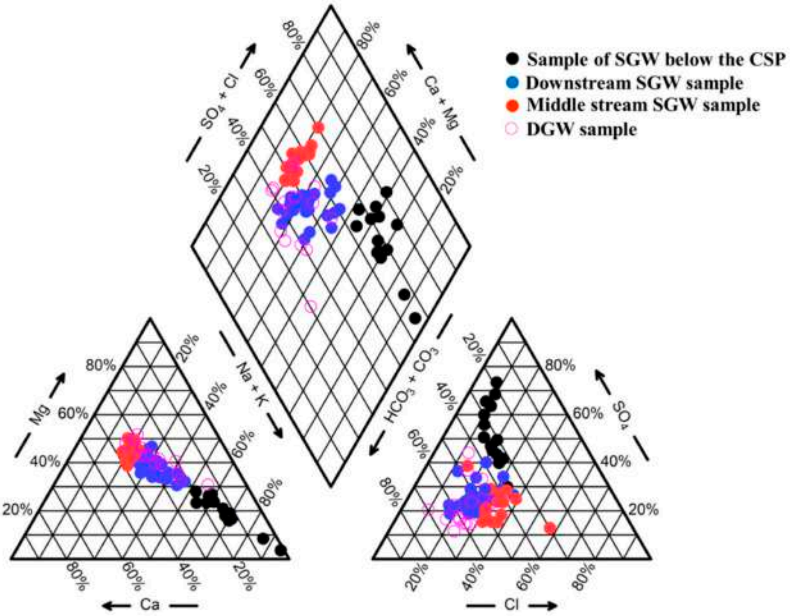

**Figure 3.** Piper diagram for shallow and deep groundwater. CSP represents chromium slag pile.

The TDS of deep groundwater in the site was 504–1198.26 mg/L. The anions were mainly $HCO_3^-$, $SO_4^{2-}$, $Cl^-$, $NO_3^-$, and the cations were mainly $Na^+$, $Ca^{2+}$, $Mg^{2+}$. The $NO_3^-$ concentration in the deep groundwater was lower than that in the shallow groundwater, but still exceeded the quality standard of domestic drinking water. It may be that the shallow groundwater overflowed into the deep groundwater, resulting in abnormal $NO_3^-$ concentration in the deep groundwater. The deep hydrogeochemical composition was simpler than the shallow ones, and the groundwater was mainly $HCO_3$-Cl-Mg-Ca type, $HCO_3$-Na-Mg type and $HCO_3$-$SO_4$-Mg-Na-Ca type.

#### 4.2.2. Spatial Distribution Pattern of Ions

##### Spatial Distribution Pattern of Ions in Shallow Groundwater

Based on the analytical results of shallow groundwater samples, the spatial distribution pattern of ions was analyzed to study the spatial contamination characteristics of each ion component in groundwater (Figure 4a). The pollutant correlation coefficient matrix was plotted using R (Figure 4b). The Pearson's correlation coefficient was used to characterize the correlation between different pollutants.

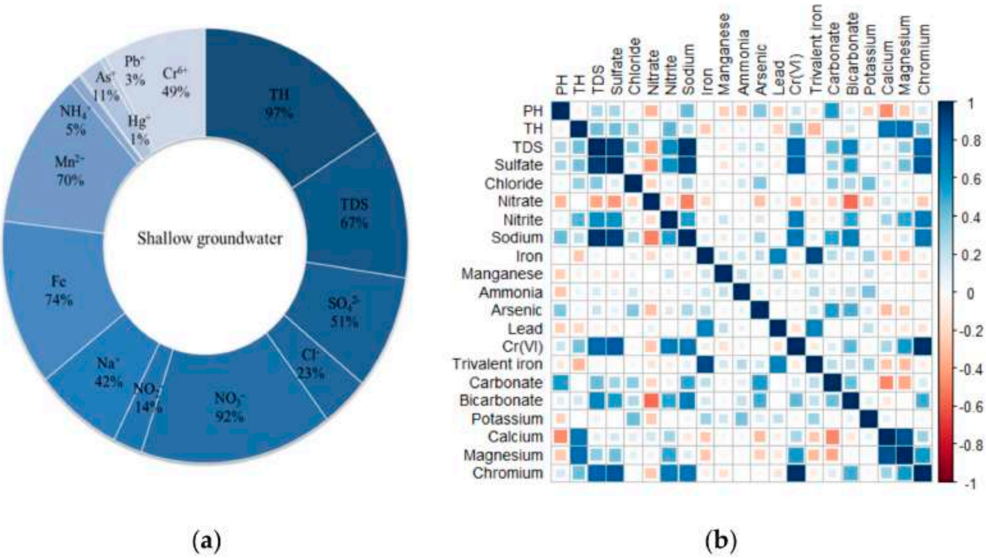

**Figure 4.** (**a**) Exceedance rate of each component of groundwater, (**b**) pollutant correlation coefficient matrix.

The TDS of 67% of the shallow groundwater samples exceeded three types of groundwater standards, especially the TDS concentration below the chromium slag pile and near the slag pile was the highest, and the water quality was poor, which was seriously affected by the chromium slag pile. Among the tested samples, the total hardness of 97% of the groundwater samples exceeded three types of groundwater standards, and the distribution of total hardness was similar to that of $Ca^{2+}$ and $Mg^{2+}$ concentration distribution, and the correlation coefficient reached 75%, indicating that the total hardness was mainly affected by the $Ca^{2+}$ and $Mg^{2+}$. The $SO_4{}^{2-}$ concentration of 51% of the groundwater samples exceeded three types of groundwater standards, and the distribution of sulfate concentration was extremely similar to that of TDS, and the correlation coefficient reached 95%. Generally, $SO_4{}^{2-}$ ions came from the dissolution of gypsum or sulfate sedimentary rocks. However, it can be seen that a large amount of sulfuric acid was used in the production of chromium salt, so it can be concluded that the $SO_4{}^{2-}$ exceeded the standard in groundwater and was closely related to the production of chromium salt, and the correlation coefficient with Cr(VI) reached 83%. The $NO_3{}^-$ concentration of 92% of the groundwater samples exceeded three types of groundwater standard. $Na^+$ concentration distribution was similar to that of TDS and $SO_4{}^{2-}$ with a correlation coefficient of 96%, and the correlation coefficient between $Na^+$ and Cr(VI) was 0.72, mainly due to the fact that a large amount of sodium chromate and sodium sulfate will be produced in the chromium salt production process, resulting in the exceedance of $Na^+$ concentration in groundwater. The exceedance of Fe and Mn reached 74% and 70%, respectively. The exceedance of Cr(VI) was 49%, which had a certain contribution rate to TDS, and the correlation coefficient reached 78%. Pb and Hg concentrations in groundwater samples had low exceedance rates, which may be related to human activities.

Spatial Distribution Pattern of Ions in Deep Groundwater

According to the analysis results of deep groundwater samples, it can be concluded that the total hardness of 68% of the tested samples exceeded the three groundwater standards, and the distribution of total hardness was similar to the distribution of $Ca^{2+}$ and $Mg^{2+}$ concentrations, with a correlation coefficient of 75% (Figure 5). The over-standard rate of TDS was 16%. For cations, $Mg^{2+}$ had the highest correlation coefficient with TDS, reaching 0.81, followed by Cr(VI), reaching 0.79, indicating that $Mg^{2+}$ contributed the most to the increase of TDS, and for anions, $SO_4{}^{2-}$ had the highest correlation coefficient with TDS, reaching 0.89, indicating that $SO_4{}^{2-}$ contributed the most to the increase of TDS. $Na^+$ exceeded the standard by 5%, and the correlation coefficient reached 79% with hexavalent chromium. The over-standard rate of $NO_3{}^-$ was 79%. The over-standard rates of Fe and Mn reached 68% and 74%, respectively, which were comparable to those of Fe and Mn in shallow groundwater. The 58% of Cr(VI) concentration exceeded the standard in deep groundwater, and the highest correlation coefficient between Cr(VI) and $SO_4{}^{2-}$ reached 0.92. Deep groundwater was less polluted than shallow groundwater, and the ion concentration was less than that of shallow groundwater, and the overall exceedance rate of each component was lower than that of shallow groundwater. The reason for exceeding the standard was mainly due to the shallow groundwater overflowing into deep groundwater.

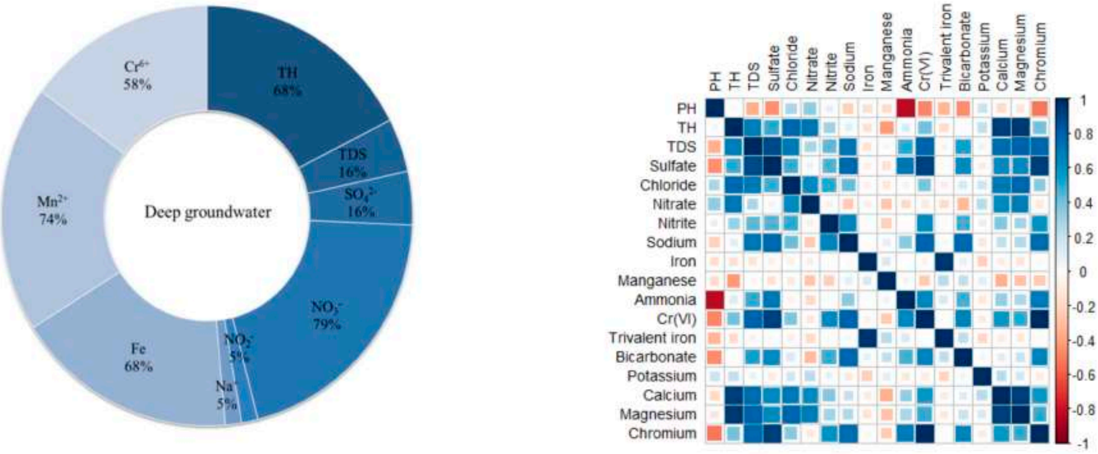

**(a)** **(b)**

**Figure 5.** (**a**) Exceedance rate of each component of groundwater, (**b**) pollutant correlation coefficient matrix.

### *4.3. Analysis of the Causes of Groundwater Chemistry Types*

#### 4.3.1. Groundwater Chemistry Control Mechanisms

A Gibbs plot can be used to illustrate the causal mechanism of water chemical composition [41]. In the Gibbs plot, if the TDS value is high and the $Na^+/(Na^++Ca^{2+})$ or $Cl^-/(Cl^-+HCO_3{}^-)$ ratio is close to 1, the ion control mechanism is evaporative crystallization. If the TDS value is medium and the $Na^+/(Na^++Ca^{2+})$ or $Cl^-/(Cl^-+HCO_3{}^-)$ ratio is less than 0.5, the ion control mechanism is water rock effect. If TDS value is low and the $Na^+/(Na^++Ca^{2+})$ or $Cl^-/(Cl^-+HCO_3{}^-)$ ratio is close to 1, the water chemistry component control mechanism is the rainfall effect [42,43]. From the Figure 6, it can be seen that the chemical composition of groundwater in the study area is mainly dominated by water–rock action.

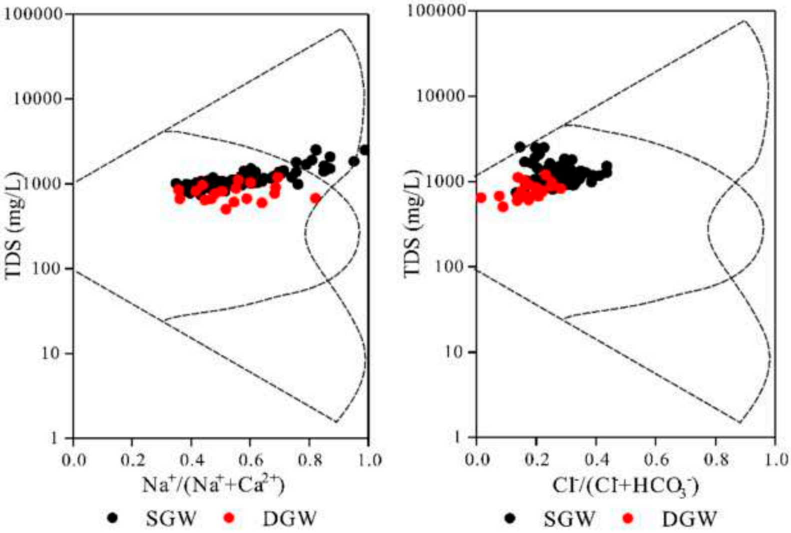

**Figure 6.** Gibbs diagrams showing the groundwater chemistry controlling mechanisms.

4.3.2. Major Ion Ratio Relationship

In order to further explore the process of site water chemistry, the interrelationship between each major ion was analyzed [42]. As can be seen from Figure 7a, most of the shallow groundwater samples were distributed along the Na/Cl ratio 1:1 line (halite dissolution line), and the Na/Cl ratio of a few samples was greater than 1, indicating that there were other sources of $Na^+$ in the groundwater in addition to halite dissolution filtration, mainly related to the production process of sodium dichromate, which led to the increase of $Na^+$ concentration in the groundwater around the chromium slag dumps. Most of the deep groundwater samples were distributed along the Na/Cl ratio 1:1 line, and the Na/Cl ratio values of a few samples were greater than 1, mainly because the shallow contaminated groundwater entered the deep aquifer, leading to the $Na^+$ concentration to increase.

The sources of $Ca^{2+}$ and $SO_4{}^{2-}$ are commonly the dissolution of gypsum and anhydrite. As can be seen from Figure 7b, most of the shallow groundwater samples were distributed along the $Ca/SO_4$ ratio 1:1 line (gypsum and anhydrite dissolution line), and a few samples had $Ca/SO_4$ ratio less than 1, mainly because the plant will use a large amount of sulfuric acid in the production process leading to the increase of $SO_4{}^{2-}$ concentration in groundwater around the chromium slag pile, while the groundwater sample points near the $Ca/SO_4$ ratio 1:1 line showed most samples with $Ca/SO_4$ ratios greater than 1, and it may be alternate cation adsorption with constant $Ca^{2+}$ release. The deep groundwater samples were all distributed along the $Ca/SO_4$ ratio 1:1 line, but most of the samples presented $Ca/SO_4$ ratios greater than 1, indicating that the dissolution of aragonite, calcite and dolomite was a potential source of $Ca^{2+}$ in the site groundwater.

From the relationship pattern of $(Ca^{2+}+Mg^{2+})/(SO_4{}^{2-}+HCO_3{}^-)$ [44], it was clear that the majority of water samples were distributed along the 1:1 line, except for groundwater samples with heavily contaminated samples, further indicating that calcite, dolomite, gypsum and anhydrite dissolution were potential sources of major ions in the groundwater mineralization process (Figure 7c).

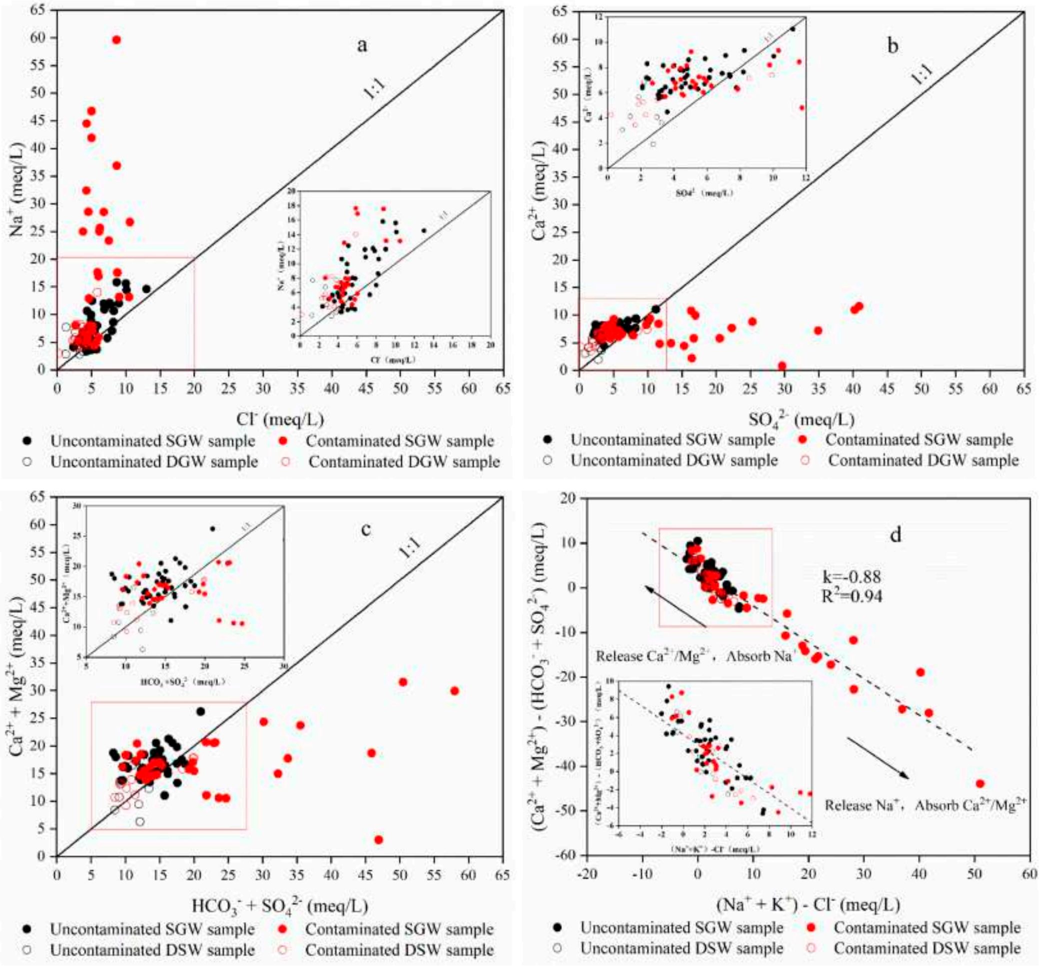

**Figure 7.** Groundwater main ion relationship diagram. (**a**) represents the ratio of $Na^+$ and $Cl^-$, which generally indicates the dissolution of halite. (**b**) rep-resents the ratios of $Ca^{2+}$ and $SO_4{}^{2-}$, which generally indicates the dissolution of gypsum and an-hydrite. (**c**) indicates the dissolution of calcite and dolomite. (**d**) can indicate the presence or ab-sence of ion exchange interaction.

In addition, the relationship between $(Ca^{2+}+Mg^{2+})$-$(SO_4{}^{2-}+HCO_3{}^-)$ and $(Na^++K^+)$-$Cl^-$ can usually be used to determine whether there is an ion alternate adsorption reaction in the aquifer. If the two are linear and the slope is close to –1, it indicates the existence of ion exchange, where the sample points distributed along the fitted line on the right side of the origin are the cation alternate. The sample points distributed along the fitted line to the left of the origin were the reverse reaction of alternate cation adsorption, and $R^2$ = 0.94 as shown in Figure 7d. This indicated that ion exchange existed in the groundwater of the site, which further illustrated that the part of groundwater sample points continuously released $Ca^{2+}$ under the reverse reaction of alternate cation adsorption. It verified the result that the Ca/$SO_4$ ratio was greater than 1.

### *4.4. Hydrogeochemical Simulation and Analysis*

The potential hydrogeochemical processes in the groundwater were investigated through ion ratio relationships. In this section, the minerals saturation index (SI) was calculated by Phreeqc 2.8 [45] to further determine the forms of the various minerals present and the geochemical interactions.

#### 4.4.1. Mineral Saturation Index Analysis

The saturation index of minerals can visualize the dissolved equilibrium state of components in groundwater. Three representative water samples were selected for this study: the severely contaminated water sample S54 with hexavalent chromium concentration of 257 mg/L, the moderately contaminated water sample S01 with hexavalent chromium concentration of 60.3 mg/L, and the lightly contaminated water sample S43 with hexavalent chromium concentration of 0.729 mg/L. For the water sample S54, the saturation index of hexavalent chromium minerals was $CaCrO_4 > Na_2CrO_4 > MgCrO_4 > K_2CrO_4 > Na_2Cr_2O_7 > K_2Cr_2O_7 > CrO_3$, and the saturation index was less than 0, which indicated that hexavalent chromium minerals were easily dissolved in the groundwater, and the proportion of chromium oxide was the largest among chromium minerals. The saturation index of trivalent chromium minerals was ordered as $Cr_2O_3 > MgCr_2O_4 > Cr(OH)_3 > CrCl_3$, and the saturation index of $Cr_2O_3$, $MgCr_2O_4$ and $Cr(OH)_3$ were greater than 0, while the saturation indices of $CrCl_3$ were less than 0. It can be concluded from the saturation index of trivalent chromium minerals that most of the trivalent chromium minerals were insoluble in groundwater, and $CrCl_3$ made the greatest contribution to the concentration of trivalent chromium ions. For groundwater sample S01, the saturation index of hexavalent chromium minerals and trivalent chromium minerals showed the same variation pattern with S54. For groundwater sample S43, the saturation index of hexavalent chromium minerals was ranked as $CaCrO_4 > Na_2CrO_4 > MgCrO_4 > K_2CrO_4 > CrO_3 > K_2Cr_2O_7 > Na_2Cr_2O_7$, and the saturation index of hexavalent chromium minerals was less than 0, indicating that hexavalent chromium minerals were easy to dissolve into groundwater, but the order of mineral saturation index had changed, and the $Na_2Cr_2O_7$ component had the largest proportion in chromium-containing minerals. The saturation index of trivalent chromium minerals showed the same change pattern as S54 and S01(Figure 8a).

By comparing the saturation index of chromium-containing minerals at S54, S01 and S43, and it can be concluded that the higher the chromium ion concentration in the aquifer, the greater the saturation index of chromium-containing minerals, the smaller the tendency for hexavalent chromium minerals to dissolve and the greater the tendency for trivalent chromium minerals to precipitate.

Figure 8b showed the simulation results of the saturation index of the main minerals. The results showed that anhydrite, gypsum and halite were under unsaturated state in groundwater, and halite was the most prone to dissolution, and calcite, aragonite and dolomite were under saturated state, and dolomite was the most prone to precipitation.

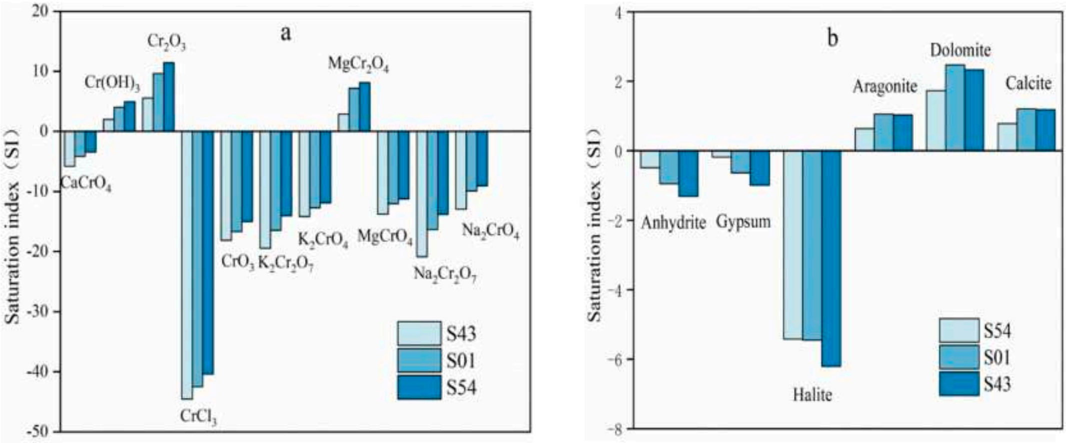

**Figure 8.** Comparison of saturation index (SI) at three points, (**a**) refers to chromium-containing minerals, including trivalent chromium and hexavalent chromium. (**b**) contains anhydrite, gypsum, halite, aragonite, dolomite and calcite.

### 4.4.2. Analysis of the Effect of pH on Minerals

After statistical analysis, the pH variation range of the site groundwater was 7.55–9.26, so the trend of minerals in the aquifer was further determined by analyzing the effect of pH variation on the saturation index of minerals. Taking S01 as an example, the pH was taken as 7.55, 8, 8.26, 9 and 9.26, respectively, which can truly reflect the trend of dissolution and precipitation of minerals in the aquifer.

As can be seen from Figure 9, the saturation index of dolomite, calcite, aragonite and $MgCr_2O_4$ is increasing with the increase of pH, indicating that $MgCr_2O_4$ was more prone to precipitation in the alkaline environment, mainly because the ionic activity product increases with the increase of pH under the condition of constant temperature, which led to the easy precipitation. With the increase of pH, the saturation index of $Na_2Cr_2O_7$, $K_2Cr_2O_7$ and $CrCl_3$ were decreasing, indicating that the dissolution of $Na_2Cr_2O_7$, $K_2Cr_2O_7$ and $CrCl_3$ was more likely to occur in the alkaline environment, mainly because the ionic activity product decreased with the increase of pH under the condition of constant temperature, which led to the dissolution to occur easily, and the saturation index of the remaining minerals was less affected by the change of pH.

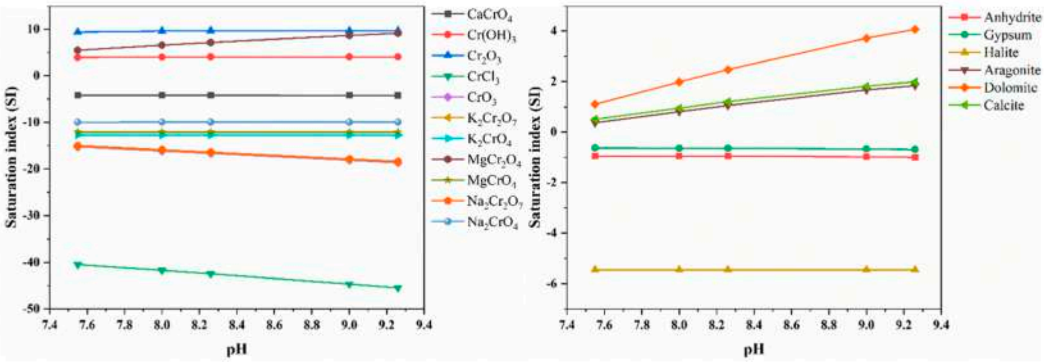

**Figure 9.** The influence of pH on the SI of minerals.

## 5. Conclusions

In this study, the distribution pattern of hydrogeochemical characteristics at a contaminated site in Xinxiang was analyzed by combination of multivariate statistical analysis and hydrochemistry, and the following conclusions were drawn.

1. The hydrochemical type of groundwater in the study area have obvious differences in the horizontal and the vertical directions, reflecting the influence of the chromium slag pile on groundwater. In the shallow groundwater, the groundwater below the chromium slag heap is the $SO_4$-$HCO_3$-Na type, the hydrogeochemical composition east of the chromium slag heap and in the midstream is the $HCO_3$-Cl-Mg-Ca type, and the downstream is basically uncontaminated with the $HCO_3$-Mg-Ca-Na type. The deep groundwater shows the $HCO_3$ type.
2. Gibbs plots, ion ratios and saturation index indicated that the hydrogeochemical characteristics of the study area are mainly controlled by water-rock action and evaporative crystallization, with dissolution of halite, gypsum and anhydrite, precipitation of aragonite, calcite and dolomite, and precipitation of trivalent chromium minerals other than $CrCl_3$ and dissolution of hexavalent chromium minerals occurring in the groundwater of the site.
3. The groundwater in the study area is generally alkaline with a minimum pH of 7.55, which is conducive to the precipitation of trivalent chromium and the dissolution of hexavalent chromium. With the increase of pH, the saturation index of dolomite, calcite, aragonite and $MgCr_2O_4$ keeps increasing, and these minerals are more likely to precipitate. The saturation index of $Na_2Cr_2O_7$, $K_2Cr_2O_7$ and $CrCl_3$ is decreasing, and the more easily $Na_2Cr_2O_7$, $K_2Cr_2O_7$ and $CrCl_3$ dissolve, and the saturation index of the remaining minerals is less affected by the change of pH.
4. Currently, the groundwater at the site is heavily contaminated and the groundwater chemistry type is altered. First, we should analyze the effects of other contaminants on chromium remediation in conjunction with indoor experiments. Second, we should maintain the concept of joint management of soil and groundwater. Third, the site groundwater runoff conditions are relatively poor and can be remediated by permeable reactive barriers technology and in situ injection of pharmaceuticals.

**Author Contributions:** Formal analysis, Y.C. and Q.Z.; investigation, Y.Z., Y.S., W.S. and Z.L.; writing-original draft preparation, W.C.; writing-review and editing, W.C. and Y.Z. (Co-first authors); supervision, Y.C. and Q.Z. All authors have read and agreed to the published version of the manuscript.

**Funding:** This research is funded by Science and Technology Research Project of Henan Provincial Department of Natural Resources (Yu Natural Resources Letter [2019] No. 373-8); National Key R&DProgram of China (No. 2019YFC1804801).

**Institutional Review Board Statement:** Not applicable.

**Informed Consent Statement:** Not applicable.

**Data Availability Statement:** Data is contained within the article.

**Acknowledgments:** We sincerely thank the reviewers for useful comments and suggestions.

**Conflicts of Interest:** The authors declare that we do not have any commercial or associative interest that represents a conflict of interest in connection with the work submitted.

## References

1. Gu, X.; Xiao, Y.; Yin, S.; Shao, J.; Pan, X.; Niu, Y.; Huang, J. Groundwater level response to hydrogeological factors in a semi-arid basin of Beijing, China. *J. Water Supply Res. Technol.* **2017**, *66*, 266–278. [CrossRef]
2. Elgallal, M.; Fletcher, L.; Evans, B. Assessment of potential risks associated with chemicals in wastewater used for irrigation in arid and semiarid zones: A review. *Agric. Water Manag.* **2016**, *177*, 419–431. [CrossRef]

3. Esmaeili-Vardanjani, M.; Rasa, I.; Amiri, V.; Yazdi, M.; Pazand, K. Evaluation of groundwater quality and assessment of scaling potential and corrosiveness of water samples in Kadkan aquifer, Khorasan-e-Razavi Province, Iran. *Environ. Monit. Assess.* **2015**, *187*, 53. [CrossRef] [PubMed]
4. Xiao, Y.; Gu, X.; Yin, S.; Shao, J.; Cui, Y.; Zhang, Q.; Niu, Y. Geostatistical interpolation model selection based on ArcGIS and spatio-temporal variability analysis of groundwater level in piedmont plains, northwest China. *SpringerPlus* **2016**, *5*, 425. [CrossRef]
5. Lu, S.; Zhang, X.; Liang, P. Influence of drip irrigation by reclaimed water on the dynamic change of the nitrogen element in soil and tomato yield and quality. *J. Clean. Prod.* **2016**, *139*, 561–566. [CrossRef]
6. Bai, B.; Jiang, S.; Liu, L.; Li, X.; Wu, H. The transport of silica powders and lead ions under unsteady flow and variable injection concentrations. *Powder Technol.* **2021**, *387*, 22–30. [CrossRef]
7. Megharaj, M.; Avudainayagam, S.; Naidu, R. Toxicity of hexavalent chromium and its reduction by bacteria isolated from soil contaminated with tannery waste. *Curr. Microbiol.* **2003**, *47*, 51–54. [CrossRef]
8. Yang, G.; Xia, J. Chromium Contamination Accident in China: Viewing Environment Policy of China. *Environ. Sci. Technol.* **2011**, *45*, 8605–8606.
9. Priti, S.; Vipin, B.; Agarwal, S.K.; Vipin, V.; Kesavachandran, C.N.; Pangtey, B.S.; Neeraj, M.; Pal, S.K.; Mithlesh, S.; Goel, S.K. Groundwater Contaminated with Hexavalent Chromium [Cr (VI)]: A Health Survey and Clinical Examination of Community Inhabitants (Kanpur, India). *PLoS ONE* **2012**, *7*, e47877.
10. Hori, M.; Shozugawa, K.; Matsuo, M. Hexavalent chromium pollution caused by dumped chromium slag at the urban park in Tokyo. *J. Mater. Cycles Waste Manag.* **2015**, *17*, 201–205. [CrossRef]
11. Kumari, B.; Tiwary, R.K.; Srivastava, K.K. Physico-Chemical Analysis and Correlation Study of Water Resources of the Sukinda Chromite Mining Area, Odisha, India. *Mine Water Environ.* **2017**, *36*, 356–362. [CrossRef]
12. Bai, B.; Nie, Q.; Zhang, Y.; Wang, X.; Hu, W. Cotransport of heavy metals and SiO2 particles at different temperatures by seepage. *J. Hydrol.* **2021**, *597*, 125771. [CrossRef]
13. Guo, H.; Chen, Y.; Hu, H.; Zhao, K.; Li, H.; Yan, S.; Xiu, W.; Coyte, R.M.; Vengosh, A. High Hexavalent Chromium Concentration in Groundwater from a Deep Aquifer in the Baiyangdian Basin of the North China Plain. *Environ. Sci. Technol.* **2020**, *54*, 10068–10077. [CrossRef]
14. Bai, B.; Rao, D.; Chang, T.; Guo, Z. A nonlinear attachment-detachment model with adsorption hysteresis for suspension-colloidal transport in porous media. *J. Hydrol.* **2019**, *578*, 124080. [CrossRef]
15. Bai, B.; Long, F.; Rao, D.; Xu, T. The effect of temperature on the seepage transport of suspended particles in a porous medium. *Hydrol. Process.* **2017**, *31*, 382–393. [CrossRef]
16. Lockhart, K.M.; King, A.M.; Harter, T. Identifying sources of groundwater nitrate contamination in a large alluvial groundwater basin with highly diversified intensive agricultural production. *J. Contam. Hydrol.* **2013**, *151*, 140–154. [CrossRef]
17. Alam, F. Evaluation of hydrogeochemical parameters of groundwater for suitability of domestic and irrigational purposes: A case study from central Ganga Plain, India. *Arab. J. Geosci.* **2014**, *7*, 4121–4131. [CrossRef]
18. Yang, J.; Graf, T.; Ptak, T. Impact of climate change on freshwater resources in a heterogeneous coastal aquifer of Bremerhaven, Germany: A three-dimensional modeling study. *J. Contam. Hydrol.* **2015**, *177–178*, 107–121. [CrossRef]
19. Li, P.; Wu, J.; Qian, H. Hydrochemical appraisal of groundwater quality for drinking and irrigation purposes and the major influencing factors: A case study in and around Hua County, China. *Arab. J. Geosci.* **2016**, *9*, 15. [CrossRef]
20. Nematollahi, M.J.; Ebrahimi, P.; Razmara, M.; Ghasemi, A. Hydrogeochemical investigations and groundwater quality assessment of Torbat-Zaveh plain, Khorasan Razavi, Iran. *Environ. Monit. Assess.* **2016**, *188*, 2. [CrossRef]
21. Tiwari, A.K.; Pisciotta, A.; Maio, M.D. Evaluation of groundwater salinization and pollution level on Favignana Island, Italy. *Environ. Pollut.* **2019**, *249*, 969–981. [CrossRef]
22. Rezaei, A.; Hassani, H.; Hayati, M.; Jabbari, N.; Barzegar, R. Risk assessment and ranking of heavy metals concentration in Iran's Rayen groundwater basin using linear assignment method. *Stoch. Environ. Res. Risk Assess.* **2018**, *32*, 1317–1336. [CrossRef]
23. Rezaei, A.; Hassani, H.; Jabbari, N. Evaluation of groundwater quality and assessment of pollution indices for heavy metals in North of Isfahan Province, Iran. *Sustain. Water Resour. Manag.* **2019**, *5*, 491–512. [CrossRef]
24. Rezaei, A.; Hassani, H. Hydrogeochemistry study and groundwater quality assessment in the north of Isfahan, Iran. *Environ. Geochem. Health* **2018**, *40*, 583–608. [CrossRef]
25. Rezaei, A.; Hassani, H.; Hassani, S.; Jabbari, N.; Fard Mousavi, S.B.; Rezaei, S. Evaluation of groundwater quality and heavy metal pollution indices in Bazman basin, southeastern Iran. *Groundw. Sustain. Dev.* **2019**, *9*, 100245. [CrossRef]
26. Rezaei, A.; Hassani, H.; Tziritis, E.; Fard Mousavi, S.B.; Jabbari, N. Hydrochemical characterization and evaluation of groundwater quality in Dalgan basin, SE Iran. *Groundw. Sustain. Dev.* **2020**, *10*, 100353. [CrossRef]
27. Xiao, Y.; Gu, X.; Yin, S.; Pan, X.; Shao, J.; Cui, Y. Investigation of Geochemical Characteristics and Controlling Processes of Groundwater in a Typical Long-Term Reclaimed Water Use Area. *Water* **2017**, *9*, 800. [CrossRef]
28. Zhang, J.; Shi, Z.; Wang, G. Hydrochemical characteristics and evolutionary laws of groundwater in Dachaidan area, Qaidam Basin. *Earth Sci. Front.* **2020**, *28*, 194.
29. Tiwari, A.K.; Orioli, S.; De Maio, M. Assessment of groundwater geochemistry and diffusion of hexavalent chromium contamination in an industrial town of Italy. *J. Contam. Hydrol.* **2019**, *225*, 103503. [CrossRef]

30. Laxmankumar, D.; Satyanarayana, E.; Dhakate, R.; Saxena, P.R. Hydrogeochemical characteristics with respect to fluoride contamination in groundwater of Maheshwarm mandal, RR district, Telangana state, India–ScienceDirect. *Groundw. Sustain. Dev.* **2019**, *8*, 474–483. [CrossRef]
31. Zhu, F.; Liu, T.; Zhang, Z.; Liang, W. Remediation of hexavalent chromium in column by green synthesized nanoscale zero-valent iron/nickel: Factors, migration model and numerical simulation. *Ecotoxicol. Environ. Saf.* **2021**, *207*, 111572. [CrossRef] [PubMed]
32. Hausladen, D.M.; Fendorf, S. Hexavalent Chromium Generation within Naturally Structured Soils and Sediments. *Environ. Sci. Technol.* **2017**, *51*, 2058–2067. [CrossRef] [PubMed]
33. Zhou, L.; Zhang, G.; Wang, M.; Wang, D.; Cai, D.; Wu, Z. Efficient removal of hexavalent chromium from water and soil using magnetic ceramsite coated by functionalized nano carbon spheres. *Chem. Eng. J.* **2018**, *334*, 400–409. [CrossRef]
34. Wang, X.; Li, L.; Yan, X.; Meng, X.; Chen, Y. Processes of chromium (VI) migration and transformation in chromate production site: A case study from the middle of China. *Chemosphere* **2020**, *257*, 127282. [CrossRef]
35. Hausladen, D.M.; Alexander-Ozinskas, A.; Mcclain, C.; Fendorf, S. Hexavalent Chromium Sources and Distribution in California Groundwater. *Environ. Sci. Technol.* **2018**, *52*, 782–792. [CrossRef]
36. Rezaei, A.; Hassani, H.; Mousavi, S.B.F.; Jabbari, N. Evaluation Of Heavy Metals Concentration In Jajarm Bauxite Deposit In Northeast Of Iran Using Environmental Pollution Indices. *Malays. J. Geosci.* **2019**, *3*, 12–20. [CrossRef]
37. Esmaeili, A.; Moore, F.; Keshavarzi, B. Nitrate contamination in irrigation groundwater, Isfahan, Iran. *Environ. Earth Sci.* **2014**, *72*, 2511–2522. [CrossRef]
38. Bai, B.; Xu, T.; Nie, Q.; Li, P. Temperature-driven migration of heavy metal $Pb^{2+}$ along with moisture movement in unsaturated soils. *Int. J. Heat Mass Transf.* **2020**, *153*, 119573. [CrossRef]
39. Wagh, V.M.; Panaskar, D.B.; Varade, A.M.; Mukate, S.V.; Gaikwad, S.K.; Pawar, R.S.; Muley, A.; Aamalawar, M.L. Major ion chemistry and quality assessment of the groundwater resources of Nanded tehsil, a part of southeast Deccan Volcanic Province, Maharashtra, India. *Environ. Earth Sci.* **2016**, *75*, 1418. [CrossRef]
40. Karagüzel, R.; Irlayici, A. Groundwater pollution in the Isparta Plain, Turkey. *Environ. Geol.* **1998**, *34*, 303–308. [CrossRef]
41. Gibbs, R.J. Mechanisms Controlling World Water Chemistry. *Science* **1970**, *170*, 1088–1090. [CrossRef]
42. Kanagaraj, G.; Elango, L. Hydrogeochemical processes and impact of tanning industries on groundwater quality in Ambur, Vellore district, Tamil Nadu, India. *Environ. Sci. Pollut. Res. Int.* **2016**, *23*, 24364–24383. [CrossRef]
43. Xiao, Y.; Shao, J.; Cui, Y.; Zhang, G.; Zhang, Q. Groundwater circulation and hydrogeochemical evolution in Nomhon of Qaidam Basin, northwest China. *J. Earth Syst. Sci.* **2017**, *126*, 26. [CrossRef]
44. Wang, L.; Dong, Y.; Xie, Y.; Song, F.; Wei, Y.; Zhang, J. Distinct groundwater recharge sources and geochemical evolution of two adjacent sub-basins in the lower Shule River Basin, northwest China. *Hydrogeol. J.* **2016**, *24*, 1967–1979. [CrossRef]
45. Zhu, G.; Wu, X.; Ge, J.; Liu, F.; Wu, C. Influence of mining activities on groundwater hydrochemistry and heavy metal migration using a self-organizing map (SOM). *J. Clean. Prod.* **2020**, *257*, 120664. [CrossRef]

MDPI
St. Alban-Anlage 66
4052 Basel
Switzerland
Tel. +41 61 683 77 34
Fax +41 61 302 89 18
www.mdpi.com

*Applied Sciences* Editorial Office
E-mail: applsci@mdpi.com
www.mdpi.com/journal/applsci

MDPI
St. Alban-Anlage 66
4052 Basel
Switzerland

Tel: +41 61 683 77 34

www.mdpi.com

ISBN 978-3-0365-6178-3